Abstract #	Presenting Author:	Institute:	Title of Abstract:
A01	Taraje Whitfield	University of Connecticut	Magnesium Phosphate Graphene/PLGA Composite Microsphere-Based Matrices for Bone Regenerative Engineering
A02	Mia Huang	Cornell University	Differential Effects of Continuous and Intermittent Salt-Inducible Kinase Inhibition on Cortical and Cancellous Bone Responses to Mechanical Loading
A03	Hirmand Salehi	New York Medical College	Comparative Analysis of Frailty Scores for Predicting Severe Adverse Acute Outcomes Following Lumbar Fusion in Degenerative Spondylolisthesis: A National Inpatient Sample Study
A04	Christopher Perrino	Montefiore Einstein	The Addition of Fluid Management to the Grapefruit Training Model: A More Realistic Arthroscopic Model
A05	Ludovica Stilli	New York Medical College	The 5-Factor Modified Frailty Index is Predictive of Intraoperative Fractures in Primary Hip and Knee Arthroplasty: An Analysis of the National Inpatient Sample Database
A06	Joseph Salem-Hernández	UPR-School of Medicine	A Modified Posterior Approach to the Nerve Transfer of the Spinal Accessory Nerve to the Suprascapular Nerve
A07	Meng Feng	Columbia University	A Multi-functional Small Molecule 4-PPBP Enhances Healing of Meniscus Tears and Functional Outcomes
A08	Wayne Lam	Children's Hospital of Philadelphia	Transcriptomic and epigenomic atlas of human bone marrow reveals gene regulatory networks and cell-cell interactions driving mesenchymal and hematopoietic progenitor fates
A09	Alina Feng	Icahn School of Medicine at Mount Sinai	In Vivo Characterization of Human Fetal Enthesis Cells
A10	Vishal Shankar	Montefiore Einstein	Improvement after TKA to a KOOS Jr greater than 71: Implications for Merit Based Reimbursements
A11	Larion Martin Santiago	Icahn School of Medicine at Mount Sinai	WNT7A lipid nanoparticles promote muscle hypertrophy and reduce fatty infiltration
A12	Nandaraj Taye	Hospital for Special Surgery	Harnessing Blastema-Derived ctsk-cre+ Cells for Post-Amputation Limb Regeneration in Mice
A13	Madison Weckerly	New York Medical College	Pregnancy and Lactation Associated Osteoporosis: A Systematic Review
A14	Mihir Sharma	Montefiore Einstein	Congenital Scoliosis: An Update to Its Natural History and Clinical Approach
A15	Tori Kroon	Icahn School of Medicine at Mount Sinai	Mature-like Intervertebral Disc Cells Compromise the Extracellular Matrix to Attenuate Injury-Induced Inflammatory Signaling and Myeloid Cell Recruitment
A16	Omar Dervisevic	Cornell University	Treatment with Parathyroid Hormone Does Not Attenuate Osteoarthritis Progression Following Daily Loading
A17	Janet Hsu	Montefiore Einstein	Posterior Lumbar Fusions with Adjacent Laminectomies: Outcomes and Radiographic Alignment
A18	Joseph Bisiani	Stony Brook University	Proton Pump Inhibitor Use is Associated with an Increased Risk of Extensor Tendon Rupture in Patients With Gastroesophageal Reflux Disease
A19	Everett Weinstein	Columbia University	Understanding Lineage Capacity of Blastema-Driven Craniofacial Joint Regeneration
A20	Timothy Jacobsen	Icahn School of Medicine at Mount Sinai	Distinct Neutrophil Populations Support Regenerative Healing In Neonatal Mice
A21	Joana I. Almeida	Icahn School of Medicine at Mount Sinai	SerpinA1a is a Novel Age-Related Mediator of Intervertebral Disc Function and Myeloid Cell Recruitment
A22	Denise Iliff	Icahn School of Medicine at Mount Sinai	Combined Anti-TNFα and Anti-depressant Treatments Alleviate Pain in Male and Female Rats in a Chronic In-vivo Discogenic Pain Model
A23	Morgan Roche	Montefiore Einstein	Higher ASA Score Associated with Complications and Mortality Following Nonunion Surgery
A24	Harrison Ho	Montefiore Einstein	Spatial Transcriptomic Profiling of Osteosarcoma in Clinically Relevant Mouse Model
A25	Giulia DiRaimo	Montefiore Einstein	The Critical Role of Irisin in Maintaining Bone Health and Its Therapeutic Potential for Diabetic Osteoporosis and Neuropathy
A26	Wataru Morita	Hospital for Special Surgery	Effects of Tendon Graft Decellularization in a Murine Model of Anterior Cruciate Ligament Reconstruction
A27	Levon Rodriguez	Icahn School of Medicine at Mount Sinai	Annulus Fibrosus Progenitor Gene Signature is Conserved in Human, Bovine, and Mouse Intervertebral Discs

Abstract #	Presenting Author:	Institute:	Title of Abstract:
A28	Vincent Sise	Hospital for Special Surgery	The Effect of Contact Paradigm and Tissue Composition on the Rolling Versus Silding Behavior in the Knee
A29	Kasoorelope (Soore) Oguntuyo	Icahn School of Medicine at Mount Sinai	Determining the Role of Mechanosensitive PIEZO1 Ion Channel in Directing Skeletal Muscle Fibro-Adipogenic Progenitor Function
A30	Claire Pinnie	Columbia University	Phenol Red Enhances Tissue Engineered Cartilage for Osteoarthritis Treatment Through Estrogenic Properties
A31	Ciara Woellhof	Stony Brook University	Parametric Finite Element Analysis of Protective Padding for Pediatric Commotio Cordis Mitigation
A32	Mohamed Said	Montefiore Einstein	Surgical Treatment of Early-Onset Blount Disease: Who is Left in Varus?
A33	Janai Augustin	University of Pennsylvania	Synovium-Cartilage Crosstalk in Facet Joint Osteoarthritis and Correlations with Adjacent Disc Degeneration
A34	Faizan Khalid	Montefiore Einstein	MRI PREDICTORS OF OSTEOCHONDRAL INJURY IN ADOLESCENTS WITH PATELLAR DISLOCATION: ROLE OF TROCHLEAR DYSPLASIA AND RECURRENT INSTABILITY
A35	Christopher J. O'Connor-Coates	Stony Brook University	Response of articular cartilage to bipedal loading
A36	Steven M. Henick	Montefiore Einstein	The Multi-Level Axial Patellofemoral Score (MAPS-TD) to Stratify Trochlea Dysplasia Severity
A37	Brianna S. Orozco	University of Pennsylvania	Comparison of transport properties between human and tissue-engineered vertebral endplates
A38	Neharika Bhadouria	Icahn School of Medicine at Mount Sinai	Lumbar Intervertebral Disc Injury Induces Pain-Like Behaviors And Disability In A Mouse Discogenic Pain Model
A39	Edmund Corcoran	Montefiore Einstein	Internal Fixation of Pediatric Knee Osteochondral Defects: Outcomes at 6-Year Mean Follow-Up
A40	Ofir Horovitz	Montefiore Einstein	So Many Surgeries: Can we minimize the number of surgeries performed for deformity correction in Severe Early-Onset Blount Disease?
A41	Michelle Villagran	Icahn School of Medicine at Mount Sinai	Spinal Alignment Device Enables Detection of Sagittal Curvature Changes in a Mouse Disc Degeneration Model
A42	Mixame Jerome	The City College of New York	Adaptation of the BioDent for Spherical Microindentation to Determine Elastic Modulus in Small Rodent Bones
A43	Josh Grey	Icahn School of Medicine at Mount Sinai	Perturbation of the mechanical microenvironment disrupts muscle stem cell self-renewal in vivo
A44	Katherine Spack	Columbia University	Proteome composition and tissue structural dynamics during scar-free ligament regeneration in zebrafish
A45	Saswati Kar	Icahn School of Medicine at Mount Sinai	Generation of fibrocartilage cells for rotator cuff repair guided by identification of sequential signaling activation during human fetal enthesis development
A46	Alessia Randazzo	Rensselaer Polytechnic Institute	Hypoxic Culture Enhances Biomechanical Properties of Engineered Scaffold-Free Tendon Fibers and Upregulates Collagen I, Collagen III, and Lysyl Oxidase
A47	Rami Abuqubo	Montefiore Einstein	The Orthopaedic Impact of Chronic Kidney Disease and Associated Mineral and Bone Disorder – A Comparative Analysis of Clinical Profiles and Laboratory Markers
A48	Linda Liang	Icahn School of Medicine at Mount Sinai	Hallmarks of Fibrocartilage Cells from Human Fetal Enthesis
A49	Carlos Salazar	Montefiore Einstein	Predictability of Polyethylene Insert Size Using an Imageless Robotic System in Total Knee Arthroplasty: A Single-Surgeon Experience
A50	Eliana Weinstein	Montefiore Einstein	Rethinking Pain Control in Adolescent Idiopathic Scoliosis Surgery: The Role of the Erector Spinae Plane Block
A51	Maria Blumenkrantz	Columbia University Irving Medical Center	Dynamic cell plasticity drives synovial joint regeneration in adult zebrafish
A52	Olivia Stala	New York Medical College	Diabetes Mellitus is a Risk Factor for Extended Length of Stay and Non-Home Discharge Following Non-Elective Hip Arthroplasty: A National Inpatient Sample Study
A53	Katherine Arnold	UConn Health	Characterization of ethanol post-treatment on collagen type I scaffolds for pathological tendon modelling
A54	Cole Angell	UConn Health	Comparing Three In Vitro Mineralization Techniques to Model Calcific Tendinopathy Pathogenesis

Abstract #	Presenting Author:	Institute:	Title of Abstract:
A55	Maxwell Ruffner	New York Medical College	Frailty Scores 11-item Modified Frailty Index (11-mFI) and Charlson Comorbidity Index (CCI) Predict Delayed Fracture Fixation in Patients with Intertrochanteric Fractures: An Analysis of the National Inpatient Sample
A56	Kathryn Grabowski	Stony Brook University	Carpal Tunnel Syndrome and Other Predictors of Amyloidosis
A57	Lynn Ann Forrester	Montefiore Einstein	Outcomes after Treatment of Scaphoid Nonunion with Open Reduction Internal Fixation and Corticocancellous vs Cancellous Only Nonvascularized Autograft
A58	Abhijith Annasamudram	Montefiore Einstein	A Shorter Interval Between Preoperative Radiation and Surgery Does Not Increase Wound Complications in Soft-Tissue Sarcoma: A Single Institutional Experience
A59	Srinidhi Raghav	New York Medical College	Frail Cancer Patients with Extremity Fractures Treated Surgically are More Likely to have Extended Length of Stay and Nonhome Discharge than Non-Frail counterparts as measured by the 11-item Modified Frailty Index: A National Inpatient Sample Database
A60	Jessica Chao	Montefiore Einstein	Distressed Communities Index and Postoperative Outcomes in Geriatric Hip Fracture Patients
A61	GaYoung Park	Icahn School of Medicine at Mount Sinai	Hyperosmotic Pressure Mimics Mechanical Confinement and Regulate Muscle Stem Cell Fate
A62	Dylan Horan	Montefiore Einstein	Improved Healing of Pathologic Long-bone Fractures: Contemporary Outcomes in the Era of Modern Cancer Therapy
A63	Safiyah Ali	Columbia University Irving Medical Center	Investigating the role of AP-1 during zebrafish ligament regeneration
A64	Chynna Smith	Montefiore Einstein	From Variant to Function: Using Machine Learning to Uncover the Regulatory Syntax Governing Osteoblast Differentiation in Osteoporosis
A65	Kelsey Gsell	University of Delaware	Tendon Type and Health Influence the 3D Organization of Collagen Fibrils Visualized with Machine Learning Assisted Segmentation and Reconstruction of SBF-SEM Images

Magnesium Phosphate Graphene/PLGA Composite Microsphere-Based Matrices for Bone Regenerative Engineering

Authors : Taraje Whitfield[1], Cato T. Laurencin[1-5*]

[1]*The Cato T. Laurencin Institute for Regenerative Engineering, University of Connecticut, Farmington, CT, 06030, USA.*
[2]*Department of Biomedical Engineering, University of Connecticut, Storrs, CT, 06269, USA.*
[3]*Department of Orthopaedic Surgery, University of Connecticut Health, Farmington, CT, 06030, USA.*
[4]*Department of Materials Science & Engineering, University of Connecticut, Storrs, CT, 06269, USA. USA.*
[5]*Department of Chemical & Bimolecular Engineering, University of Connecticut, Storrs, CT, 06269, USA.*

Keywords: Bone Regenerative Engineering, Magnesium Phosphate Graphene, Wnt/β-Catenin

Bone defects affect millions of people annually, making bone tissue of particular interest for developing treatments [1]. Current strategies, including autograft, allograft, xenograft, and metallic implants, are lacking in complete, successful solutions due to their many drawbacks including secondary pain, disease transmission and poor osteointegration [2-3]. In the past decade, the field of Regenerative Engineering has shown promise to in healing complex tissues of the body, including critical-sized bone defects, which will not heal without intervention. Regenerative Engineering seeks to achieve while evading drawbacks of current options by utilizing synthetic bone grafts. One material that offers such benefits is a class of functional graphenic material, known as Phosphate Graphenes [4]. Therefore, in this work, we fabricated composite microsphere-based matrices by incorporating Magnesium Phosphate Graphene (MgPG) within poly(lactic-co-glycolic) acid and studied them for their morphological, chemical, and physical characteristics for bone regeneration *in vitro*. Next, we evaluated the cytocompatibility and osteogenic potential of these PLGA/MgPG composite matrices *in vitro*, which demonstrated high cytocompatibility and osteogenesis. Lastly, we evaluated the gene expression profile of different markers of the canonical β-catenin dependent Wnt signaling pathway to understand the potential underlying mechanism behind the enhanced osteogenic potential of MgPG. Thus, these scaffolds demonstrated potential for osteogenesis and proliferation that are highly desired for the regeneration of critical-sized defects. With further study, these mechanically competent porous MgPG matrices may provide practical solutions to the problem of effectively regenerating critical-sized bone defects by delivering bioactive molecules to the defect site to aid in tissue regeneration, thus overcoming a major hurdle in orthopaedics.

Acknowledgements:
NIH T32 AR079114 and the Young Innovative Investigator Program (YIIP) at the University of Connecticut.

References

[1] Baldwin P, Li DJ, Auston DA, Mir HS, Yoon RS, Koval KJ. Autograft, Allograft, and Bone Graft Substitutes: Clinical Evidence and Indications for Use in the Setting of Orthopaedic Trauma Surgery. J Orthop Trauma. 2019;33(4):203-213.
[2] Amini AR, Laurencin CT, Nukavarapu SP . Bone tissue engineering: recent advances and challenges. Crit Rev Biomed Eng. 2012;40(5):363-408.
[3] Davis R, Singh A, Jackson MJ, et al. A comprehensive review on metallic implant biomaterials and their subtractive manufacturing. Int J Adv Manuf Technol. 2022;120(3-4):1473-1530.
[4] Arnold AM, Holt BD, Daneshmandi L, Laurencin CT, Sydlik SA. Phosphate graphene as an intrinsically osteoinductive scaffold for stem cell-driven bone regeneration. Proc Natl Acad Sci U S A 2019;116:4855-4860.

Differential Effects of Continuous and Intermittent Salt-Inducible Kinase Inhibition on Cortical and Cancellous Bone Responses to Mechanical Loading

Muyin (Mia) Huang[1], F. Patrick Ross[2], Marc Wein[3], Marjolein C.H. van der Meulen[1,4]

[1]Cornell University, Ithaca, NY, [2]FPR Scientific Consulting, Amherst, MA

[3]Endocrine Unit, Massachusetts General Hospital, Boston, MA, [4]Hospital for Special Surgery, New York, NY

Introduction: Osteoporosis affects one in three women and is the most common metabolic bone disorder, leading to skeletal fractures[1]. Intermittent parathyroid hormone (PTH), an FDA-approved anabolic therapy, enhances bone formation at loaded sites[2] via inhibition of Salt Inducible Kinases (SIKs)[3]. PTH use is limited by duration of efficacy[4] and daily injections. Orally available SIK inhibitors stimulate bone formation similarly to PTH, increasing cancellous bone in young male mice[5]. Continuous and intermittent PTH affect bone differently,[2,6] but the mechanisms of continuous vs. intermittent SIK inhibition have not been examined. Here, we extended our previous work on continuous SIK inhibition[7] by comparing its effects with intermittent inhibition in adult female mice and examined the interaction with mechanical loading across skeletal sites.

Method: Following IACUC approval, 16-week-old female C57BL/6J mice (n=10/grp) received SIK inhibitor SK-124 via either intraperitoneal injection[7] (continuous, IP) or oral gavage (intermittent) at 40 mg/kg, or were given a vehicle solution (sterile water, oral gavage/IP, VEH) for six weeks (5d/wk). Daily in vivo cyclic mechanical loading was applied to the left tibia (L, 5d/wk, 9N, 4Hz, 1200 cycles)[8], and the right limb was the contralateral control (C). On day 41, blood was collected via cardiac puncture to analyze bone serum markers and residual SK-124 levels 24 hours after the last treatment dose. Tibiae were dissected for microCT imaging at the cancellous core and cortical shell of the metaphysis, and the mid-diaphyseal cortex. Data was analyzed using a linear mixed model (loading & treatment: fixed effects, mouse: random effect), with significance at $p<0.05$. A Tukey HSD post-hoc test was conducted when the interaction term was significant.

Results: Continuous SIK-inhibited animals had an increased residual SK-124 level compared to VEH administration of both routes and SK-124 via oral gavage (Fig. 1a), confirming IP injection induced continuous exposure and oral gavage induced intermittent exposure. SIK inhibition via both routes increased bone formation (serum P1NP, Fig. 1b). Intermittent SIK inhibition increased cancellous bone volume fraction (BV/TV) and trabecular thickness. However, the response to loading in SIK-inhibited animals was diminished; loading increased cancellous BV/TV more in VEH compared to SK-124 group (Fig. 2a,b). Continuous SIK inhibition also increased cancellous BV/TV and did not affect the response to loading (Fig. 2a). Both metaphyseal shell and mid-diaphysis cortical bone thickness (Ct.Th) increased with intermittent SIK inhibition, although loading was not synergistic with SIK inhibition (Fig. 2c,d). In contrast, continuous SIK inhibition decreased Ct.Th and amplified the response to mechanical loading, rescuing the SIK inhibition-induced bone reduction (Fig. 2d).

Discussion: Continuous SIK inhibition increased cancellous bone mass but reduced cortical bone, which aligns with the bone phenotype in hyperparathyroidism. Mechanical loading was essential for maintaining cortical bone mass. In contrast, intermittent SIK inhibition was anabolic at both cancellous and cortical sites but not synergistic with mechanical loading. Instead, intermittently SIK-inhibited animals had a blunted response to loading in cancellous bone. Cancellous bone formation could be near its maximum rate under the effect of intermittent SIK inhibition and loading. Overall, the efficacy of intermittent SIK inhibition as an oral therapy was evident through its anabolic effects and the importance of administration route and dosing is emphasized. Future studies should evaluate the potential of intermittent SIK inhibition in clinical settings.

References: [1]Imel et al., 2014. [2]Sugiyama et al., 2008. [3]Wein et al., 2016. [4]Aslan et al., 2012. [5]Sato et al., 2022. [6]Uzawa et al., 1995. [7]Huang et al., 2024 ORS [8]Fritton et al., 2005.

Acknowledgments: Funding provided by Robert and Helen Appel Fellowship, and NIH R01-AR081943. We thank the Cornell CARE Staff.

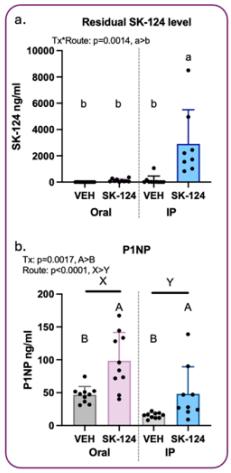

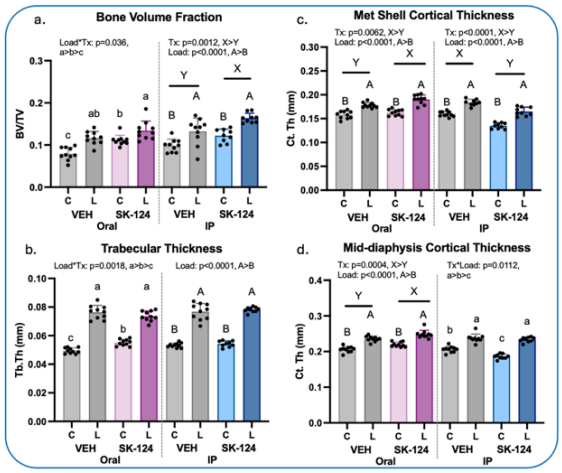

Figure 1 (left) a) Animals administered SK-124 via IP injection had higher residual levels 24 hours after the final dose. **b)** Both continuous and intermittent SIK inhibition increased bone formation marker, P1NP

Figure 2 (right) a & b) Animals administered SIK inhibitor SK-124 via oral gavage (intermittent) or IP (continuous) had an increased cancellous bone mass. Response to loading in the oral gavage group was blunted. **c & d) Cortical bone mass increased in** animals administered intermittent SIK inhibitor via Oral Gavage; SIK inhibition administered via IP decreased cortical bone mass, and loading rescued the loss (C: Control; L: Loaded)

Comparative Analysis of Frailty Scores for Predicting Severe Adverse Acute Outcomes Following Lumbar Fusion in Degenerative Spondylolisthesis: A National Inpatient Sample Study

Hirmand Salehi BS[1], Staton Albert BS[1], Jared Sasaki BS[1], Victor Koltenyuk BA[1], Elizabeth Drugge PhD[1], Jay Ayar DrPH[2],

Harshadkumar A. Patel MD[3], Anna R. Cooper MD[4]

Affiliations:[1] New York Medical College School of Medicine, Valhalla, New York, USA[2] New York Medical College School of Public Health, Valhalla, New York, USA[3] Department of Orthopaedic Surgery, Westchester Medical Center Health Network, Valhalla, New York, USA [4] Department of Orthopaedic Surgery, Montefiore Medical Center

Degenerative spondylolisthesis (DS) is increasingly treated with posterior lumbar decompression with and without fusion in older adults. Accurate frailty assessment is crucial given the elevated risk of postoperative complications and associated healthcare costs. The Risk Analysis Index (RAI) is a rapid bedside tool that incorporates demographic and nutritional information, potentially offering broader frailty assessment than the Modified Frailty Index (mFI-5) and Charlson Comorbidity Index (CCI).

This study evaluates the predictive performance of the RAI, compared to mFI-5 and CCI, for severe postoperative outcomes in DS patients undergoing single-level lumbar fusion surgery.

The National Inpatient Sample 2015 Q4-2021 was used to examine the predictive performance of three frailty indices among patients aged 40 years or older with DS who underwent lumbar fusion surgery. The primary outcome was Clavien-Dindo grade IV complications (CD-IV), defined as life-threatening complications requiring ICU management. Secondary outcomes included non-home discharge (NHD) and extended length of stay (ELOS, >3 days).

Patients were identified by ICD-10-CM code for lumbar spondylolisthesis and ICD-10-PCS procedure codes for single-level lumbar fusion. We excluded fusion of two or more lumbar vertebral joints and congenital spondylolisthesis. Weighted logistic regression models were fit. Discriminative performance was assessed via area under the receiver operating characteristic curve (AUC). Balanced sensitivity and specificity were assessed using optimal cut-points for predicted probability.

A total of 84,341 patients were identified. The prevalence of CD-IV, NHD, and ELOS was 3%, 14.4%, and 28.4%, respectively. All three frailty indices were associated with each outcome but their predictive performance differed. For CD-IV, RAI (AUC: 0.65, 95% CI: 0.64–0.66) was comparable to mFI-5 (0.65, 95% CI: 0.64–0.66) but lower than CCI (0.74, 95% CI: 0.73–0.75). CCI had the highest sensitivity and specificity for CD-IV. For non-home discharge, RAI (0.68, 95% CI: 0.68–0.69) slightly outperformed mFI-5 (0.66, 95% CI: 0.65–0.66) and was slightly lower than CCI (0.70, 95% CI: 0.70–0.71). CCI and mFI-5 were more specific for NHD but RAI was more sensitive. For ELOS, RAI (0.55, 95% CI: 0.54–0.55) showed similar performance to mFI-5 (0.56, 95% CI: 0.55–0.56) but was inferior to CCI (0.58, 95% CI: 0.57–0.58). MFI-5 had the highest specificity and CCI had the highest sensitivity for ELOS.

RAI is an independent predictor of acute postoperative morbidity for DS but demonstrates inferior discrimination compared to CCI and similar performance to mFI-5 across the three measured outcomes. For NHD and ELOS, RAI had similar predictive probability to mFI-5 and CCI. RAI incorporates functional, cognitive, and nutritional domains alongside demographic factors such as age and sex. Limitations of this study include reliance on administrative coding in NIS, underreporting of cognitive and functional data, and absence of long-term outcomes.

The Addition of Fluid Management to the Grapefruit Training Model: A More Realistic Arthroscopic Model

Christopher Perrino, Harrison A. Volaski MD, Yung-Tai Lo PhD, Michael Hossack MD, Benjamin J. Levy MD, I. Martin Levy MD
Department of Orthopaedic Surgery, Montefiore Einstein, Bronx,NY

Purpose: To determine the face and construct validity of a modified grapefruit training model (GTMFM) incorporating fluid inflow/outflow and arthroscopic shaver use. **Methods:** Orthopaedic residents, fellows, and attendings were stratified into novice (n=10), intermediate (n=10), and advanced (n=9) groups. Participants performed five arthroscopic tasks on the GTMFM, including fluid management and precision resection. Performance was scored for task completion, accuracy, and water management (maximum 31 points). Task times were recorded. Construct validity was tested by comparing scores and times across groups. Face validity was assessed by attending surgeon survey responses. **Results:** Median total scores increased progressively with experience (Beginners 21.5, Intermediates 28.5, Advanced 31; $p < .001$). Advanced participants outperformed both intermediates ($p = .001$) and beginners ($p < .001$). Median task completion time decreased from 18 minutes (Beginners) to 6.3 minutes (Advanced; $p < .003$). Advanced participants demonstrated significantly superior water management and shaver precision ($p \leq .009$). Survey responses from nine attendings confirmed strong face validity, with 77.8%–100% rating the model as “very closely” aligned with training objectives. **Conclusions:** The GTMFM is a simple, low-cost simulator that demonstrates both face and construct validity. By incorporating fluid management and shaver tasks, the model discriminates skill levels and approximates essential elements of arthroscopic training. **Clinical Relevance:** This enhanced grapefruit-based trainer provides an accessible, reproducible platform for early arthroscopic skill acquisition, supplementing high-fidelity simulators and cadaveric labs while reducing cost barriers.

The 5-Factor Modified Frailty Index is Predictive of Intraoperative Fractures in Primary Hip and Knee Arthroplasty: An Analysis of the National Inpatient Sample Database

Authors Alejandra Chavarria BS[1], Katherine Condra BA[1], Ludovica Stilli BA[1], Jay Ayar DrPH, MPH, BDS [2], Elizabeth Drugge PhD, MPH[2], Anna R. Cooper MD, MPH [3]

Affiliations
1 School of Medicine, New York Medical College, Valhalla, NY
2 School of Public Health, New York Medical College, Valhalla, NY
3 Department of Orthopaedic Surgery, Montefiore Medical Center, 3400 Bainbridge Avenue, 6th Floor, Bronx, NY 10467, USA

Purpose: This study assesses the association between frailty as measured by the 5-factor Modified Frailty Index (mFI-5) and intraoperative fracture risk in patients undergoing total hip arthroplasty (THA) and total knee arthroplasty (TKA) using a nationally representative dataset.

Methods: Using the 2015-2019 National Inpatient Sample (NIS), adult patients undergoing elective, primary THA or TKA were identified by NIS procedural codes. Frailty variables were collected and categorized using the mFI-5 as robust (0), prefrail (1), or frail (≥2). Multivariate logistic regression was used to assess the association between frailty and intraoperative fracture, adjusting for demographic, clinical, socioeconomic, and hospital-level factors. All analyses were two-sided with statistical significance set at $p<0.05$.

Results: A total of 964,194 hospitalizations were analyzed, including 372,419 (38.62%) THA and 591,775 (61.38%) TKA. Intraoperative fractures occurred in 0.55% of THA and 0.15% of TKA patients. In THA, frailty modified fracture risk by age. Frail individuals ≥68 years had significantly higher predicted probabilities of intraoperative fracture. In TKA, frailty was associated with increased risk across all ages. Frail TKA patients had 58% higher odds of intraoperative fracture compared to robust counterparts (aOR: 1.58, 95% CI: 1.30–1.93). Female sex, public or self-pay insurance, lower income, treatment in rural hospitals, and surgery in the Western U.S. were also independently associated with higher fracture risk.

Conclusion: Frailty as measured by mFI-5 was a significant and independent predictor of intraoperative fractures in both THA and TKA, with age-modified effects in THA. These findings support the integration of frailty screening into preoperative risk stratification to guide personalized surgical planning and perioperative management. Sociodemographic and regional practice differences continue to be risk factors for adverse events in arthroplasty surgeries.

Figure 1: Predicted Probability of Intraoperative Fracture in (a) THA patients and (b) TKA patients by mFI-5 and Age

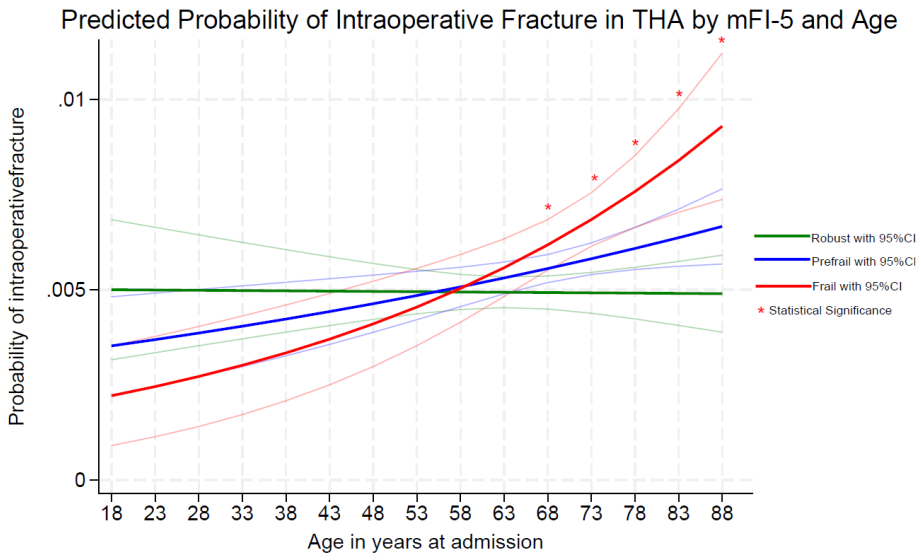

A Modified Posterior Approach to the Nerve Transfer of the Spinal Accessory Nerve to the Suprascapular Nerve

Joseph Salem-Hernández, Lenny L. Rivera-Rosario; Ruben Tresgallo Parés; José I. Acosta-Julbe; Alexandra Claudio Marcano; Joseph Salem-Hernández; Gerardo S. Caussade Silvestrini; Norman Ramirez; Christian Foy-Parrilla
UPR School of Medicine, Hospital for Special Surgery

Purpose : Restoration of shoulder abduction and external rotation is critical in patients with upper brachial plexus injuries (BPIs). The transfer of the spinal accessory nerve to the suprascapular nerve is a well-established surgical technique; however, the optimal approach remains debated. The traditional posterior approach may compromise muscle integrity because of trapezius detachment and splitting of the supraspinatus. This study introduces a muscle-sparing modification to the posterior approach and evaluates functional outcomes in pediatric and adult patients with obstetric or traumatic BPIs.

Methods : A retrospective review was conducted on patients who underwent spinal accessory nerve to suprascapular nerve transfer using a muscle-sparing posterior approach from September 2018 to November 2022. Inclusion criteria comprised pediatric patients (aged ≤18 months) with obstetric BPIs and adult patients with traumatic BPIs with a minimum postoperative follow-up of 24 months. Pediatric patients were evaluated using the Toronto Muscle Grading System, Modified Mallet Grading System, and Birch Triple System. Adults were assessed using range of motion and Disabilities of the Arm, Shoulder, and Hand questionnaire scores.

Results : Fourteen patients met the inclusion criteria (six pediatric and eight adult). Pediatric outcomes demonstrated Modified Mallet Grading System scores of grade IV and Birch Triple System stages IV–V, indicating good shoulder function. Toronto Muscle Grading System scores of 3 reflected active movement against gravity. Among adults, mean forward flexion improved from 35° to 53°, abduction improved from 28° to 47°, and external rotation improved from 12° to 23°. The mean Disabilities of the Arm, Shoulder, and Hand questionnaire score improved from 91 to 48, exceeding the minimal clinically notable difference. No complications were observed.

Conclusions

The muscle-sparing posterior approach for spinal accessory nerve to suprascapular nerve transfer is a safe and effective technique that yields favorable functional outcomes in both pediatric and adult BPI populations. Further comparative studies are warranted.

Type of study/level of evidence

Therapeutic IV.

A Multi-functional Small Molecule 4-PPBP Enhances Healing of Meniscus Tears and Functional Outcomes

Meng Feng[1], Angelyn Nguyen[1], Hyungkyun Shin[1], Ming Wang[1], Chen Zong[1], Sarah Ginsberg[2], Chenxi Nian[2], David Pellei[1], Chris Ricupero[1], Chang Lee[1]
1. Regenerative Engineering Laboratory, Columbia University Irving Medical Center, New York, NY, USA
2. Barnard College, Columbia University, New York, NY, USA
Email of Presenting Author: mf3634@cumc.columbia.edu

Disclosures: **M. Feng:** None. **A. Nguyen:** None. **H. Shin:** None. **M. Wang:** None. **C. Zong:** None. **S. Ginsberg:** None. **C. Nian:** None. **D. Pellei:** None. **C. Ricupero:** None. **C. Lee:** None.

INTRODUCTION: Meniscus injuries lead to knee joint pain and weakened knee joint function, frequently progressing into cartilage thinning and osteoarthritis. Simultaneously, the endogenous repair capacities of the avascular meniscus are limited. Our previous studies demonstrated the efficacy of bioactive glue sequentially releasing connective tissue growth factor (CTGF) and transforming growth factor beta 3 (TGF-β3) in meniscus healing and harnessing endogenous synovial mesenchymal stem/progenitor cells (SMSCs). However, an approach involving multiple growth factors has suffered from several translational challenges. To address the challenges, we have recently repurposed a small molecule, 4-PPBP as an agonist for Sigma 1 receptor (σ1R) to maintain endoplasmic reticulum homeostasis. Our data showed that 4-PPBP promotes meniscus healing by stimulating SMSCs and modulating inflammation. However, local delivery of 4-PPBP to injured meniscus site could be challenging due to the physical barrier of extracellular matrix. Fibrin, an irreplaceable constituent forming a 3-dimensional biocompatible meshwork comprised of minuscule fibers, serves as a biodegradable material to deliver small molecules. Notably, this intricate structure attracts endogenous sMSCs, but also demonstrates distinctive viscoelastic characteristics defined by its mechanical reaction to varying frequencies of loading. Our previous studies with *in vitro* and *ex vivo* models suggested that 4-PPBP induces proliferation, migration, and differentiation of meniscal sMSCs, as well as reducing local inflammation. In this study, we investigated the efficacy of genipin-crosslinked bioactive glue (FibGen) to deliver 4-PPBP/BD1047 for meniscus repair in a rodent model. This preclinical study helps researchers and clinicians have better understand the biological mechanisms of σ1R signaling regulating meniscus homeostasis and repair *in vivo*.

METHODS: *Ex vivo meniscus explant model*: Per our established methods, a longitudinal/radial tear was created in the inner 1/3 zone of fresh bovine meniscus explants (1.0cm×0.8cm×0.6cm) and treated with 4-PPBP/FibGen. *Preclinical animal model:* This study was approved by IACUC (project number #AC-AACB1704). 78 male SD rats (body weight 300-350g) were used in this study. Longitudinal tears were established in the anterior horn of medial meniscus as we reported previously. *Bioglue preparation*: 200 mg/mL fibrinogen, 200U/mL thrombin and 2.5 mg/mL genipin at the final concentration will be mixed with an equal volume. 10uM 4-PPBP or 200nM BD1047 (σ1R-antagonist) was injected into the torn meniscus site through a syringe injection. 20ul 4-PPBP-laden bioglue was applied in meniscus injury to allow the viscoelastic gel formation. *Video-based gait analysis* was performed using a custom-built Catwalk system. Animals were allowed to walk at least 5 times through a one-meter-long treadmill. Average walking speed, stance length, stride length and stance width were evaluated. *Histological and functional assessment: the* healing of the meniscus was systemically evaluated by histological staining, video-based gait analysis, range of motion measurement and biomechanical test at 2 weeks and 4 weeks. *Gene expression*: total RNA was isolated from the knee joint tissue by Qiagen kit and qPCR was conducted to detect the anabolic, catabolic and pro-inflammatory markers. *scRNA-seq and CellChat analysis*: Per our established methods, scRNA-seq analysis was perform for single cells isolated from knee joint at 2 wks post-op, followed by cell-cell communication analysis using CellChat system. *Statistical analysis* was performed using GraphPad Prism 5.0 with Student's -test for two-group comparisons. $p<0.05$ is considered as statistically significant.

RESULTS: In our meniscus explant healing model, a single application of 4-PPBP via FibGen enhanced healing of longitudinal tears in the inner avascular zone, demonstrated by minimal tissue gapping and newly formed collagen fibers (**Fig. 1A & B**). In addition, we noticed highly proliferative cells at the peripheral region of meniscus tears with 4-PPBP application, likely confirming the effects of 4-PPBP in stimulating endogenous cellular proliferation. Similarly, 4-PPBP/FibGen bioglue enhanced healing of radial tears in the deep zone, while sMSC only failed to bridge the meniscus gapping, suggesting that FibGen provided viscoelastic scaffoldings which allow the sMSC to localize and proliferate (**Fig. 1C& D**). In our *in vivo* model, a single injection of 4-PPBP via FibGen enhanced functional recovery including average walking speed and range of motion, compared to non-treated defect and bioglue only groups. However, BD1047 delayed meniscus healing of longitudinal tears in the inner avascular zone and limited the functional recovery (**Fig. 2 A-C**). In addition, we noticed early healing at the peripheral region of meniscus tears with 4-PPBP/FibGen bioglue injection (**Fig. 2D**). In addition, 4-PPBP inhibits synovial inflammatory responses (MMP3 decrease) and protects cartilage integrity compared to non-treated group at 4 wks. The BD1047-treated group progressed to cartilage thinning, as the thickness of hyaline cartilage relative to calcified cartilage decreased (**Fig. 3A & B**). We further isolated the synovium, medial meniscus, cartilage from the medial compartment of knee joint. The PCR results further showed that 4-PPBP/bioglue also inhibits *mmp3* mRNA expression, while stimulated the expression of sox9 and col2 (**Fig. 3C**). To further determine the effect of early intervention of 4-PPBP/FibGen bioglue on knee joint homeostasis and meniscus repair at the early stage, scRNA-seq revealed the CD9+/CX3CR+ macrophage and complement system involved in the early healing. CellChat analyses are pending to date to uncover the tissue crosstalk.

DISCUSSION: In this study, our FibGen bioglue was activated by a single small molecule to serve as an artificial matrix to enhance healing and seal meniscus gapping within a torn meniscus. Our results suggest that 4-PPBP induces multiple functions in meniscal cells and SMSCs, including stimulating proliferation and migration, and reducing inflammatory responses. It indicates that 4-PPBP application stimulates endogenous SMSCs and meniscal cells to proliferate and migrate to the injury site, leading to tissue repairing. In addition, 4-PPBP inhibits synovial inflammatory responses and promotes CTGF synthesis in the acute meniscus tear site through σ1R signaling. As 4-PPBP also inhibits MMP3, IL-1β, and IL-6 expressions, our approach has significant potential as an intra-articular therapeutic in an early intervention setting following an acute meniscus injury. Moreover, a notable advantage in the use of a single small molecule rather than multiple growth factors in our previous work is its significant translational potential by minimizing regulatory barriers and the cost of developing a clinical grade product. The limitation of this project is the lack of the mechanism study of this 4-PPBP/bioactive glue at the cellular level. To better understand the biological mechanisms and pathways regulating meniscus homeostasis and repair *in vivo*, we are currently investigating cellular crosstalk from the knee joint tissue by applying single cell RNA-sequencing.

SIGNIFICANCE/CLINICAL RELEVANCE: We developed an injectable, viscoelastic and biodegradable FibGen glue with σ1R agonist 4-PPBP that can reduce inflammatory response-associated tissue damage and enhance avascular meniscus healing by eliciting the regenerative activities of endogenous sMSCs. The 4-PPBP/bioglue provides sufficient meniscal stability to the torn site that load bearing can be tolerated and torn site motion minimized which allow early functional recovery.

ACKNOWLEDGEMENTS: NIH R01DE029321 to C.H.L and Columbia Postdoc Affairs and ORS/OREF Travel Grants to M.F.

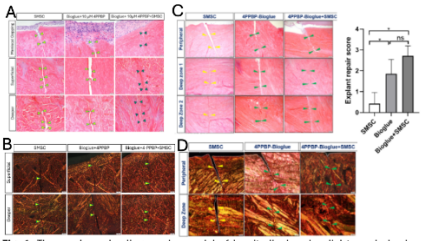

Fig. 1. The meniscus healing ex *vivo* model of longitudinal and radial tears in bovine explants by a single injection of 10μM 4-PPBP via bioglue and SMSCs for 4 weeks: (**A**) Representative H&E staining images of explant and (**B**) Picrosirius red staining under polarized microscopy for longitudinal tears (n=6 each group, scale bar=100 μm). (C) H&E and (D)PR staining under polarized microscopy radial tears. Scale bar=100 μm.

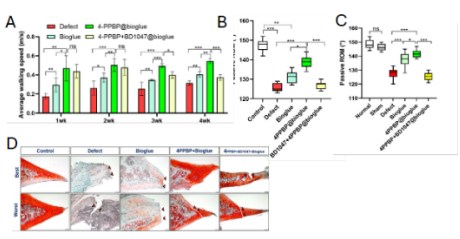

Fig. 2 Functional and histological assessment of meniscus tear post 4-PPBP-loaded bioglue treatment. (A) Effects of 4PPBP/bioglue on functional recovery from 1 wk to 4wk; (B) Range of motion at 2 wk; (C) Range of motion at 4wk, n=6 in each group. Ns: not significant, *p<0.05, **p<0.01, ***p<0.001. (D) SO/FG staining of 4-PPBP and BD1047-loaded bioglue on meniscus tear repair at 4wk. n=6, Scale bar=100 μm

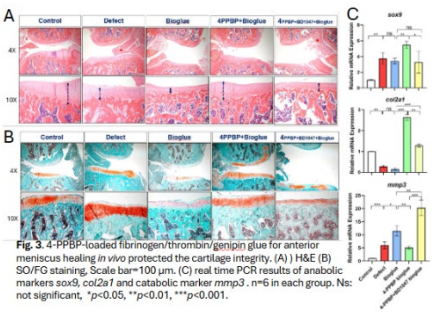

Fig. 3. 4-PPBP-loaded fibrinogen/thrombin/genipin glue for anterior meniscus healing *in vivo* protected the cartilage integrity. (A)) H&E (B) SO/FG staining, Scale bar=100 μm. (C) real time PCR results of anabolic markers *sox9*, *col2a1* and catabolic marker *mmp3* . n=6 in each group. Ns: not significant, *p<0.05, **p<0.01, ***p<0.001.

Transcriptomic and epigenomic atlas of human bone marrow reveals gene regulatory networks and cell-cell interactions driving mesenchymal and hematopoietic progenitor fates

Authors : Wayne Lam[1], Michael Duffy[2], Austin Yang[1], Kai Tan[1]

Affiliations : 1 Division of Oncology and Center for Childhood Cancer Research, Children's Hospital of Philadelphia, Philadelphia, PA

2 Department of Orthopaedic Surgery, Perelman School of Medicine, University of Pennsylvania, Philadelphia, PA

Bone marrow is a highly complex and heterogeneous environment composed of hematopoietic, mesenchymal, and endothelial lineage cells. It is the site of many diseases affecting all its constituents, including blood and immune diseases, skeletal diseases, vascular diseases, and cancer metastases. Aging increases the occurrence of these diseases. Within the bone marrow, aging is characterized by myeloid and megakaryocyte skewing of hematopoietic progenitors and adipogenic bias of mesenchymal progenitors. Both play a role in reduced immune function and diminished skeletal integrity. Organization in cellular niches, mainly regulated by mesenchymal cells, is thought to orchestrate the array of critical functions in this highly diverse tissue. To develop a mechanistic understanding of the regulation of aging bone marrow, we simultaneously profiled human femoral head transcriptomic (snRNA-seq) and epigenomic (ATAC-seq) cell states and constructed an atlas of the gene regulatory networks involved in hematopoietic stem cell and mesenchymal differentiation. Femoral head samples were collected from total hip arthroplasty and processed by the Anatomical Pathology Lab at the University of Pennsylvania. Distal trabecular bone was removed and cut into small pieces before digestion in Collagenase I (2 mg/mL) and Dispase II (4 mg/mL) in PBS. Digested cells were strained and RBC depleted (EasySep system). Granulocytes were removed to improve ATAC quality. Rare cell populations were then enriched with a CD34 selection kit (EasySep) for HSPCs and a CD45 depletion kit (EasySep) for non-hematopoietic cells. Nuclear isolations were performed on the unenriched fractions, the HSPC enriched fraction and non-hematopoietic enriched fraction. The three fractions were then mixed and single-nuclear transcriptomic and ATAC libraries constructed with Chromium Next GEM Single Cell Multiome ATAC + Gene Expression kit and sequenced on an Illumina NovaSeq platform. Data preprocessing was completed with CellRanger and scATAC-pro with hematopoietic transcripts regressed out using SoupX. Initial clustering and data analysis was performed with Seurat and Signac. CytoTALK, CytoTRACE and LIANA were used to construct cell pseudotime, cell-cell signaling networks and gene regulatory networks. From ten samples, using a strategy to enrich rare cell populations, we captured 27,596 non-hematopoietic and 18,437 hematopoietic cells, including hematopoietic stem and progenitors, myeloid cells, lymphoid lineage, osteogenic and adipogenic cells, and mesenchymal progenitor cells. The multiomic atlas captured increased non-hematopoietic cell clusters compared to scRNA-seq alone. Downstream analysis focuses on the non-hematopoietic and mesenchymal regulation of HSPC maintenance and differentiation potentiation. Using pseudo-time analysis (CytoTRACE), we predict markers regulating mesenchymal differentiation and find different gene markers in the transcriptomic and epigenomic data. We then construct signaling pathways between hematopoietic and mesenchymal cells and found 27 significant mesenchymal-HSPC interactions. For example, THY1+ MSC regulates HSCs via CXCL12. Building a transcriptional regulatory network will further allow us to elucidate the differentiation and hematopoietic regulation programs of mesenchymal cells. Our human multiomic atlas represents the first to explore the epigenetic and signaling pathways of hematopoietic and mesenchymal differentiation biases in the aging bone marrow.

In Vivo Characterization of Human Fetal Enthesis Cells

Alina Feng[1], YiYi Liang[1], Angel Moonilall[1], Fei Fang[1]

[1]Leni and Peter W. May Department of Orthopaedics, Icahn School of Medicine at Mount Sinai, New York, NY

Introduction: One of the most common injuries seen in adults is rotator cuff tears at the supraspinatus tendon enthesis [1-2]. To address this clinical challenge, stem cell therapy has recently emerged as an attractive approach [1]. However, it is unclear what the most appropriate therapeutic stem cell sources for enthesis fibrocartilage healing are. Previous mouse studies have shown that embryonic/postnatal tissue-derived progenitor cells present desired regenerative capacities for musculoskeletal tissue repair [3]. Although mouse work provides some insights into cell types for enthesis repair, there is a knowledge gap as to whether human has similar enthesis progenitors and whether these cells also maintain consistent regenerative potentials. Therefore, the goal of this study is to 1) examine whether human fetal enthesis cells could form fibrocartilage-like tissues *in vivo*, 2) examine how dynamic micro-environments of fetal cells dictate cell function after transplantation. **Methods:** Our preliminary scRNA-seq data showed that most of human fetal enthesis cells had progenitor potentials, reflected by self-renewal and multilineage differentiation capacities. Therefore, we isolated fetal enthesis cells, without cell sorting, from human fetal tissues provided by the Developmental Origins of Health and Disease Biorepository at Icahn School of Medicine at Mount Sinai (ISMMS) with full compliance with New York State Laws and ISMMS regulations for human subject protocols. The fetal cells were loaded onto an absorbable gelatin sponge overnight before transplantation. Intramuscular transplantation and renal capsule transplantations were performed in NSG-GFP mice. For intramuscular transplantations, a 1-cm longitudinal opening was made on the vastus lateralis muscle, and fetal cells carried by sponge were inserted. For renal capsule transplantation, a 1-cm longitudinal incision was made between the left flank and abdomen of the mouse. A 2-mm pocket was made in the renal capsule, and the sponge carrying the fetal cells was inserted. Histology and immunohistochemistry: vastus lateralis muscles and kidneys with identified transplanted cells were dissected at 4 weeks, 6 weeks, and 9 weeks post-surgery. The tissues were stained with H&E and Safranin O to observe tissue morphology. Expression of fibrocartilaginous markers (i.e., SOX9, OSX, COLI, COLII) were evaluated by immunostaining. **Results**: Transplanted cells in highlighted regions from 4 weeks to 9 weeks were negative for GFP, demonstrating that fetal cells survived and were maintained in the host tissue (Fig. 1). Histological sections showed clear sponge degradation with time and matrix deposition at 9 weeks post-surgery. Of note, a more organized matrix was observed at week 9 (Fig.1). Fetal enthesis cells are found to express SOX9, but not OSX (osterix). After transplantation, the cells showed decreased SOX9 expression with increased expression of OSX osteogenic markers over time (Fig. 2A). Consistent with histology, COLI, a core matrix protein of fibrocartilage, showed an obvious increase from 4 weeks to 9 weeks (Fig. 2B). Conversely, COLII showed an obvious decrease from 4 weeks to 9 weeks. This inverse relationship between COLI and COLII further indicates the formation of nascent fibrocartilage tissue. Transplanted cells in muscle and renal capsule displayed similar morphology, new tissue formation, and SOX9 expression, which indicates limited environmental influence on fetal enthesis cells. However, this needs further examination (Fig. 3). **Discussion**: Fetal enthesis cells transplanted into muscle formed fibrocartilage-like tissues, which indicates their regenerative capacities. Consistent SOX9 expression in transplanted cells showed their cartilaginous features. COLI in fetal cells was increasingly expressed across the transplantation time, accompanied by decreased COLII expression. This further indicates that fetal cells form a fibrocartilage structure rather than simple cartilage tissue, a conclusion strengthened by the observation of organized fibers in the transplanted regions of interest. An osteogenic marker, OSX, was also found to be more expressed at the transplanted regions at the later time point. As enthesis formation is characterized by fibrocartilage deposition followed by its mineralization, the expression of OSX in implanted fetal cells suggests the occurrence of mineralization. More studies should be conducted to examine whether this process is fibrocartilage mineralization or ectopic ossification. Surprisingly, no obvious difference in the morphology of fetal cells and related matrix/protein expression was found between renal capsule and muscle transplantation at week 4, which could be explained by robust identities s of fetal enthesis cells. Our study suggests that human fetal enthesis retains autonomous maturation capacity even when removed from its original environment. The similarities seen from our data with previous mouse data provide a bridge from animal models to clinical translation which provides a better understanding of human fetal enthesis cell niche and function that could translate to potential use in cell-based therapies for rotator cuff healing. **References:** [1] S. Kar et al. *The Journal of Physiology* 2025 [2] H. Lu et al. *Annu Rev Biomed Eng* [3] F. Fang et al. *Cell Stem Cell* 2022

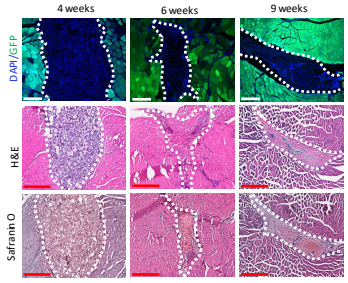

Figure 1: Immunofluorescence, H&E, and SafraninO staining of muscles transplanted with fetal enthesis cells at 4 weeks, 6 weeks, and 9 weeks after implantation. The regions with transplanted cells are highlighted by dashed lines. Red scale bar, 500um; White scale bar, 250um.

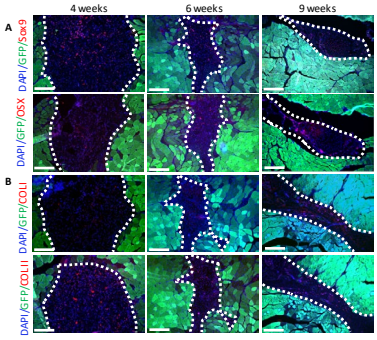

Figure 2: Immunostaining of SOX9, OSX, COLI, and COLII in fetal enthesis cells transplanted to muscles at 4 weeks, 6 weeks, and 9 weeks. White scale bar, 250um

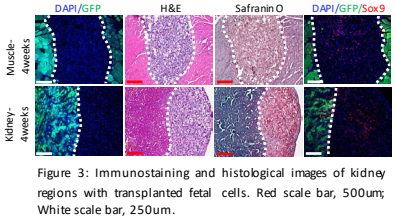

Figure 3: Immunostaining and histological images of kidney regions with transplanted fetal cells. Red scale bar, 500um; White scale bar, 250um.

Improvement after TKA to a KOOS Jr greater than 71: Implications for Merit Based Reimbursements

Authors: Vishal Shankar BA[1], Aedan Hanna MD[1, 2], Zeynep Seref-Ferlengez PhD [1, 2], Yungtai Lo PhD[1,2], John Pope MD[1,2], Eli Kamara MD[1, 2], Sun Jin Kim MD[1, 2], Zachary Berliner MD[1, 2]

Affiliations:
[1] Albert Einstein College of Medicine, Bronx, NY 10461, USA
[2] Montefiore Einstein Orthopaedic Surgery, Bronx, NY, USA

Background: The Center for Medicare & Medicaid (CMS) is introducing the merit-based incentive payment system, requiring outcome reporting. One potential measure is the proportion of patients with a postoperative Knee Injury and Osteoarthritis Outcome Score for Joint Replacement (KOOS Jr) score of 71. This study aimed to determine the percentage of patients who achieved this threshold at 1-year following primary TKA, the demographic and clinical predictors associated with this outcome, and the proportion who achieved substantial clinical benefit (SCB).

Methods: A database of primary TKA cases performed at an academic institution from 2018-2024 was queried. Demographic and clinical variables such as age, sex, BMI, ASA score, race/ethnicity, zip code, insurance payer, other joint pain, low back pain (Oswestry Questionnaire), and VR-12 physical and mental component scores were tabulated. KOOS Jr scores were recorded at the preoperative and 1-year post-operative visit. Patients that had KOOS Jr improvement of ≥ 20 points were noted to achieve SCB. Univariate analysis was performed with *Chi*-square and *t*-tests, followed by multivariate regression.

Results: The total cohort was 3,217 patients, of which 32.5% (95% C.I. 30.8%-34.15%) achieved a KOOS Jr of ≥ 71. Of the 2,572 patients with both pre-operative and post-operative KOOS Jr scores, 1,580 (61.4%) achieved the SCB, of which 728 (46.1%) had a postoperative KOOS Jr score ≥ 71. After multivariate analysis, patients that were less likely to meet the KOOS Jr cut off exhibited lower preoperative KOOS Jr scores (p=0.003), a lower preoperative mental component score (p<0.001), additional painful joints (p<0.001), low back pain (p<0.001), or identified as African American (p=0.003), Asian (p=0.017), or Hispanic/Latino (p=0.001).

Conclusions: The findings corroborate that patients may achieve meaningful clinical benefit without achieving the KOOS Jr threshold at 1-year post-operatively. This study may inform outcome reporting as new payment models are adopted.

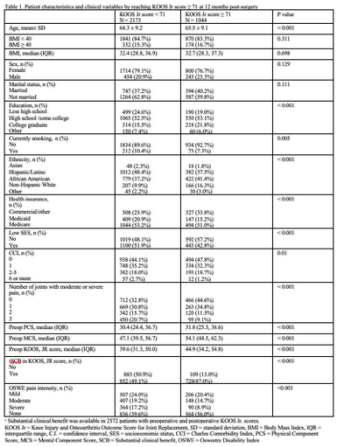

Table 1. Patient characteristics and clinical variables by reaching KOOS Jr score ≥ 71 at 12 months post-surgery

	KOOS Jr score < 71 N = 2173	KOOS Jr score ≥ 71 N = 1044	P value
Age, mean± SD	64.3 ± 9.2	65.9 ± 9.1	< 0.001
BMI < 40 BMI ≥ 40	1641 (84.7%) 332 (15.3%)	870 (83.3%) 174 (16.7%)	0.311
BMI, median (IQR)	32.4 (28.8, 36.9)	32.7 (28.3, 37.3)	0.698
Sex, n (%) Female Male	1714 (79.1%) 454 (20.9%)	806 (76.7%) 243 (23.3%)	0.129
Marital status, n (%) Married Not married	747 (37.2%) 1264 (62.8%)	398 (40.2%) 597 (59.8%)	0.111
Education, n (%) Less high school High school /some college College graduate Other	499 (24.6%) 1065 (52.5%) 314 (15.5%) 150 (7.4%)	190 (19.0%) 530 (53.1%) 219 (21.9%) 60 (6.0%)	< 0.001
Currently smoking, n (%) No Yes	1834 (89.6%) 213 (10.4%)	934 (92.7%) 73 (7.3%)	0.005
Ethnicity, n (%) Asian Hispanic/Latino African American Non-Hispanic White Other	48 (2.3%) 1012 (48.4%) 779 (37.2%) 207 (9.9%) 45 (2.2%)	10 (1.0%) 382 (37.5%) 622 (61.0%) 164 (16.3%) 30 (3.0%)	< 0.001
Health insurance, n (%) Commercial/other Medicaid Medicare	508 (25.9%) 699 (20.9%) 1044 (53.2%)	327 (33.8%) 147 (15.2%) 496 (51.0%)	< 0.001
Low SES, n (%) No Yes	1019 (48.1%) 1100 (51.9%)	892 (57.2%) 452 (42.8%)	< 0.001
CCI, n (%) 0 1 2-5 6 or more	938 (44.1%) 748 (35.2%) 362 (18.0%) 57 (2.7%)	494 (47.8%) 334 (32.3%) 191 (18.7%) 12 (1.2%)	0.01
Number of joints with moderate or severe pain, n (%) 0 1 2 3	712 (32.8%) 669 (30.8%) 342 (15.7%) 450 (20.7%)	466 (44.6%) 261 (34.8%) 120 (11.5%) 95 (9.1%)	< 0.001
Preop PCS, median (IQR)	30.4 (24.4, 36.7)	31.8 (25.5, 38.4)	< 0.001
Preop MCS, median (IQR)	47.1 (39.5, 56.7)	54.1 (44.5, 62.3)	< 0.001
Preop KOOS, JR score, median (IQR)	39.6 (31.3, 50.0)	44.9 (34.2, 54.8)	< 0.001
iSCB in KOOS, JR score, n (%) No Yes	883 (50.9%) 852 (49.1%)	109 (13.0%) 728(87.0%)	< 0.001
OSWE pain intensity, n (%) Mild Moderate Severe None	507 (24.0%) 407 (19.2%) 364 (17.2%) 834 (39.5%)	206 (20.4%) 148 (14.7%) 90 (8.9%) 565 (56.0%)	< 0.001

*Substantial clinical benefit was available in 2572 patients with preoperative and postoperative KOOS Jr scores
KOOS Jr = Knee Injury and Osteoarthritis Outcome Score for Joint Replacement, SD = standard deviation, BMI = Body Mass Index, IQR = interquartile range, C.I. = confidence interval, SES = socioeconomic status, CCI = Charlson Comorbidity Index, PCS = Physical Component Score, MCS = Mental Component Score, SCB = Substantial clinical benefit, OSWE = Oswestry Disability Index

Table 2: Factors associated with reaching KOOS Jr score ≥ 71 at 12 months post-surgery identified from logistic regression

	Odds ratio (95% C.I.)	P value
Preop MCS	1.02 (1.02, 1.03)	< 0.001
Preop KOOS Jr score	1.01 (1.003, 1.014)	0.003
Ethnicity African American Asian Hispanic/Latino Other Non-Hispanic White (reference)	 0.66 (0.50, 0.87) 0.46 (0.24, 0.87) 0.59 (0.45, 0.77) 1.00 (0.55, 1.82) 1	 0.003 0.017 0.001 0.995
Number of joints with moderate or severe pain 3 2 1 None (reference)	 0.47 (0.35, 0.63) 0.75 (0.56, 0.99) 0.99 (0.81, 1.22) 1	 < 0.001 0.048 0.948
OSWE category Severe Moderate Mild None (reference)	 0.57 (0.42, 0.77) 0.74 (0.58, 0.95) 0.66 (0.53, 0.83) 1	 < 0.001 0.019 < 0.001

MCS = Mental Component Score, KOOS Jr = Knee Injury and Osteoarthritis Outcome Score for Joint Replacement, C.I. =

References:

- Deans, C.F., et al., *New CMS Merit-Based Incentive Payment System Value Pathway After Total Knee and Hip Arthroplasty: Preparing for Mandatory Reporting.* J Arthroplasty, 2024. **39**(5): p. 1131-1135.
- Program, Q.P. *MIPS Value Pathways (MVPs)*. Available from: https://qpp.cms.gov/mips/mips-value-pathways.
- Services, C.f.M.M. *QPP Participation Status*. August 10, 2025]; Available from: https://qpp.cms.gov/participation-lookup.
- Surgery, H.f.S. *KOOS, JR SCORING INSTRUCTIONS*. 2022; Available from: https://www.hss.edu/globalassets/files/research/hss-koos-jr-scoring-instructions.pdf.
- Association, A.M., *Quality ID #470 : Functional Status After Primary Total Knee Replacement* 2022.
- Services, C.f.M.M. *Transforming Episode Accountability Model (TEAM)*. [cited 2025 August 20]; Available from: https://www.cms.gov/priorities/innovation/innovation-models/team-model.

WNT7A lipid nanoparticles promote muscle hypertrophy and reduce fatty infiltration

Larion Martin Santiago[1], Kasoorelope Oguntuyo[1], Britney Chin-Young[1], Damien Laudier[1], Zhixin Yu[1], Pedro Henrique Alves da Silva[1], Fei Fang[1], Angelo Amabile[1], Woojin M. Han[1]

[1]*Icahn School of Medicine at Mount Sinai, New York, NY*

INTRODUCTION: Myosteatosis, the infiltration of fat into skeletal muscle, and muscle atrophy are key pathologic features of muscle degeneration in chronic injuries, degenerative myopathies, and aging, correlating with increased disease severity, diminished function, and poor surgical repair outcomes.[1-3] Recombinant, secretory protein wingless-type MMTV integration site family 7a (WNT7A) has shown promise in stimulating muscle hypertrophy and reducing fatty infiltration without fibrosis, making it a promising therapeutic candidate for muscle regeneration.[4,5] However, recombinant protein therapies face challenges related to scalability, delivery, and cost.[6,7] Lipid nanoparticle (LNP) delivery of mRNA offers a promising alternative with scalable production and effective therapeutic delivery.[8,9] We assess the feasibility of LNP-mediated mRNA delivery of WNT7A (W7a-LNP) as a strategy for mitigating muscle degeneration by reducing fatty infiltration and promoting myofiber hypertrophy.

METHODS: ***WNT7A mRNA-LNP synthesis.*** Using the human *WNT7A* sequence as a template, modified RNAs were *in vitro* transcribed using HiScribe® T7 High Yield RNA Synthesis Kit and fully substituted with N^1-methylpseudouridine-5'-triphosphate (m1Ψ). LNPs were formulated via microfluidic mixing of lipid components—SM-102, DOPE, cholesterol, and DMG-PEG_{2000}, at a molar ratio of 50:10:38.5:1.5—and mRNA. ***In vivo proof-of-concept.*** All animal studies were performed following the approved IACUC protocol. Cre mRNA-LNPs (15 µg/ 30 µL) were injected in the tibialis anterior (TA) muscle of Ai14-tdTomato mice. TAs were harvested 12-13 days post-injection and cryosectioned. LNP uptake and mRNA expression in skeletal muscle was assessed by visualization of fluorescent tdTomato expression in myofibers. ***In vitro dose-response.*** Primary fibro-adipogenic progenitors (FAPs), isolated from C57BL/6 mice, and C2C12 myoblasts were cultured in growth media and differentiation media, with/without recombinant WNT7A (rWNT7A; 200 or 50 ng/mL) or W7a-LNPs (1, 10, 100 ng/mL). Cells were assessed by immunocytochemistry for perilipin-1 and myosin heavy chain to evaluate adipogenic inhibition and myotube hypertrophy, respectively. ***In vivo W7A-LNP injection in uninjured muscle.*** Vehicle (30 µL) and W7A-LNP (10 µg/ 30 µL) were injected into contralateral uninjured supraspinatus (SS) muscles of C56BL/6 mice. For multi-dose regimen, injections were repeated every two weeks for a total of three doses. SS muscles were collected 4 weeks after the final treatment. Myofiber hypertrophy was assessed by measuring myofiber diameter. ***In vivo injury and W7A-LNP treatment.*** Vehicle (35 µL), WNT7A (2.5 µg/ 35 µL), and W7a-LNPs (10 µg/ 35 µL) were injected into the TA of C57BL/6 mice 4 days post-glycerol (50% v/v; 50 µL) injury to the same TA. Muscle was harvested 14 days post-injury, and regeneration was assessed by quantification of intramuscular adipose tissue (IMAT) formation.

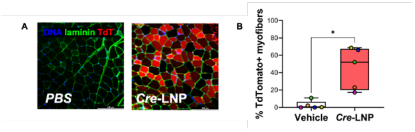

Fig. 1 Proof-of-concept mRNA-LNP delivery in skeletal muscle. **(A)** TA muscles of Ai14-tdTomato mice injected with cre-LNP or PBS. Scale bar: 100 µm. **(B)** Percentage of tdT+ myofibers. *p<0.05.

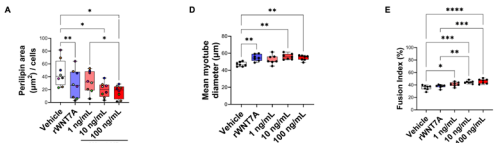

Fig. 2 W7a-LNPs reduce FAP adipogenesis and increase myotube size. **(A)** Perilipin area of FAPs treated with rWNT7A/W7a-LNP. **(C)** Mean myotube diameter and **(E)** fusion index (%) of C2C12 myoblasts treated with rWNT7A/W7a-LNP. *p<0.05; **p<0.01; ***p<0.001; ****p<0.0001.

RESULTS: *WNT7A* mRNA was encapsulated in LNPs with 97.53% efficiency, an average diameter of 75.83 nm, and polydispersity index of 0.0940. *In vivo* feasibility studies demonstrated significant expression of tdTomato following local injection of Cre-LNPs to TA (Fig. 1A,B). *In vitro* dose-response studies demonstrated significant reductions in FAP adipogenesis and increased C2C12 fusion and myotube size, notably at lower doses of W7a-LNPs (10 and 100 ng/mL) compared to recombinant WNT7A (Fig. 2A-E). In uninjured muscle, multiple W7a-LNP injections significantly increased myofiber size without inducing fibrosis, confirming its safety and efficacy in promoting muscle hypertrophy (Fig. 3A,B). Delivery of W7a-LNP 4 days post-injury significantly reduced fatty infiltration and increased TA weight (Fig. 3C-E).

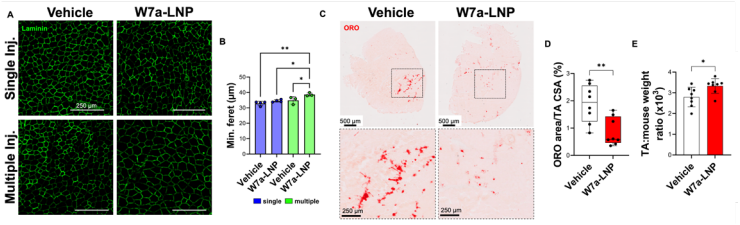

Fig. 3 W7a-LNPs promote myofiber hypertrophy and reduce IMAT. **(A)** Uninjured SS muscle following single or repeated W7a-LNP injections. **(B)** Minimum Feret's diameter of myofibers. *p<0.05; **p<001. **(C)** Glycerol-injured TA muscle following vehicle (35 µL) or W7a-LNP (10 µg/35 µL) treatment. **(D)** ORO area and **(E)** TA wet weight. *p<0.05; **p<0.01.

CONCLUSION: We show that LNPs effectively deliver mRNA payloads to muscle cells, producing and secreting WNT7A, reducing FAP adipogenesis and increasing myotube fusion and size *in vitro*. Our *in vivo* models show that W7a-LNPs can promote myofiber hypertrophy and reduce fatty infiltration of skeletal muscle after glycerol injury.

SIGNIFICANCE: Our findings establish W7a-LNPs as an effective strategy to reduce adipogenesis, prevent IMAT accumulation, and enhance myofiber hypertrophy, potentially at lower doses than recombinant WNT7A. This approach addresses challenges of dose toxicity, scalability, and production costs, and suggests broader applications of mRNA-LNPs as a therapeutic platform for chronic muscle injuries, myopathies, and other degenerative conditions.

REFERENCES: [1] Li+ *Neuromuscul Disord*. 2015; [2] Gladstone+ *Am J Sports Med*. 2007; [3] Norris+ *Cell Rep*. 2025; [4] Le Grand+ *Cell Stem Cell*. 2009; [5] Fu+ *Stem Cell Reports*. 2023; [6] Niazi+ *Biologics*. 2023; [7] Vavilis+ *Pharmaceutics*. 2023; [8] Hou+ *Nat Rev Mater*. 2021; [9] Kenjo+ *Nat Commun*. 2021. **ACKNOWLEDGEMENTS**: NIH/NIAMS R01AR080616, PRORP/CDMRP HT94252410894

Harnessing Blastema-Derived *ctsk-cre*$^{+}$ Cells for Post-Amputation Limb Regeneration in Mice

Taye, Nandaraj; Alexandrov, Alexander; Bostrom, P Mathias; and Yang, Xu
Hospital for Special Surgery, HSSRI, Osseointegration Lab, Bostrom/Yang Lab
515 East, 71st Street, New York 10021

Introduction and Objective: Limb loss remains an extremely severe clinical problem, leaving patients dependent on prosthetic devices and with limited functional recovery. Effective regenerative treatments capable of restoring severed limbs have yet to be developed in mammals. Our study aims to develop a novel regenerative method that uses the natural regenerative capacity of blastema tissue or blastema-derived stem/progenitor cells to promote limb regeneration following amputation. We developed a mouse model of below-knee amputation of the tibia to simulate clinical limb loss.

Methods: Donor mice (*ctsk-cre*$^{+}$*;mTmG*) had their digit tips, the distal 1/3 of the 3rd phalanges, (3 digits from each hind limb) amputated at P7 to P14, which is a well-studied model for blastema generation. The induced blastema tissue was collected at 7-14 days post amputation. From these tissues, the periosteal stem cells were isolated and characterized, with particular focus on *ctsk-cre*$^{+}$*;mTmG* lineage–traced populations that are enriched in skeletal progenitors. Fluorescence-activated cell sorting (FACS) was used to isolate *ctsk-cre*$^{+}$ cells from the blastema. The 16-week-old recipient MIP mice were used to avoid rejection of donor tissue or cells underwent a tibial amputation. Either whole tissue blastema (6 blastema) or sorted *ctsk-cre*$^{+}$ cells (~10,000 – 16,000 cells) were grafted under the tibial stump immediately following amputation. To facilitate engraftment and cell differentiation, we established a bioactive environment with rBMP2 protein (500 ng), fibrin hydrogel, or calcium sulfate ($CaSO_4$) cement to mimic a supportive chondrogenic and osteogenic niche. To confirm effective grafting, H&E staining and confocal imaging techniques were used.

Results: X-ray images show successful engraftment of the blastema tissues and cells at day 0 immediately post-surgery (Fig. A). After 8 weeks (blastema engraftment), and 3 weeks (cell engraftment) post-surgery, new bone regeneration at the tibial stump ends were visible. As we are grafting *ctsk-cre*$^{+}$ cells, the blastema tissue graft would answer our query about whether new bone regeneration requires only one type or a mixed population of periosteal cells. Using H&E and immunofluorescent imaging, blastema tissues were visible at the stump end of recipient's tibia (Fig. B, C). Interestingly, some cells from the blastema tissues migrated and integrated into the tibial stump of the recipient mice (Fig. D, E). Our observation also suggests that the proximity and orientation of blastema tissues have a significant impact for successful grafting. Correct orientation of the excision site of blastema tissue towards the amputated tibial stump ensures favorable host environment, effective for donor cells to integrate. In addition, chemotactic cues originating from the amputated sites of tibial stumps as well as excision sites of blastema tissues could influence cell migration behavior. To provide a controlled proximity and stability of the grafted blastema cells, we sought to use $CaSO_4$ cement as a scaffold (Fig. F). These cast $CaSO_4$ cylinders were drilled to generate a hollow space to accommodate the blastema cells. From our *in-vitro* cell culture experiment, the seeded cells distributed evenly inside the drilled hollow space as well as infiltrating the spaces within the $CaSO_4$ cylinders (Fig. G). The grafted cells were also spiked with rBMP2 protein to induce the donor cells to differentiate into osteoblast lineage (Fig. H). We hypothesized that this combination of blastema-derived stem cells and tailored niches will allow for *de novo* bone formation to induce bone lengthening and facilitate the regeneration of other tissues such as muscle, nerve and skin.

Conclusion and Significance: The present investigation provides the first step in developing a platform for mammalian limb regeneration, as even a small success could offer a foundation upon which additional tissues like muscles, nerve, vasculature and skin may eventually integrate. Our study demonstrates the regenerative potential of blastema tissues or blastema-derived periosteal stem cells in a below-knee amputation model, providing proof-of-concept for future therapeutic strategies that may one day allow patients with limb loss to regain mobility without the use of prosthetics.

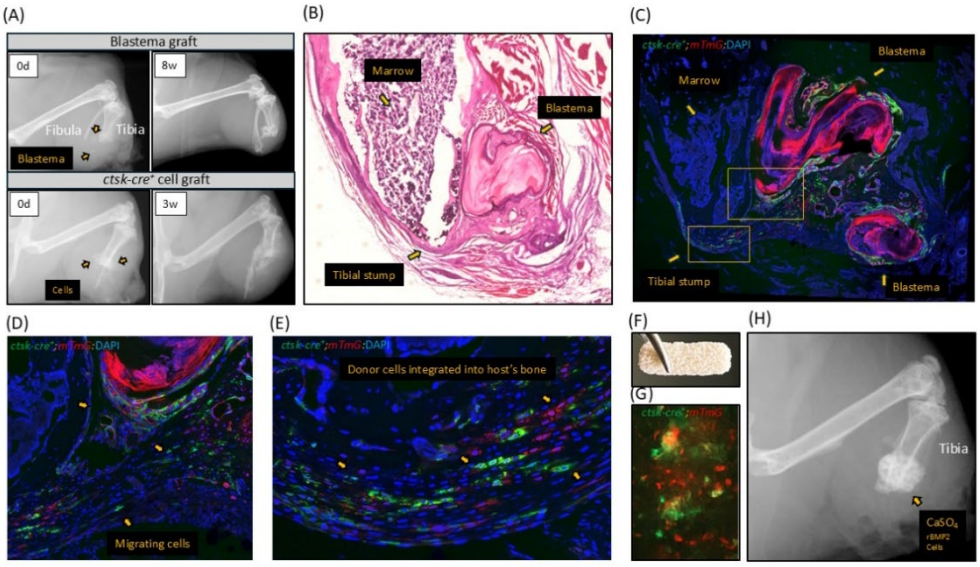

Figure: (A) X-ray images at different time points after grafting blastema tissues (yellow arrows) or *ctsk-cre*$^{+}$ cells (yellow arrows) at recipient mice's tibial stump ends post amputation. Blastema tissues are observed under the tibial stump ends after 8 weeks of engraftment (B) H&E, (C) Confocal imaging. Confocal images highlighting *ctsk-cre*$^{+}$ (GFP) & *mTmG* (tdTomato) (D) migrating cells (yellow arrows) and (E) engrafted cells (yellow arrows). (F) A cast $CaSO_4$ cement designed to support proximity and stability of the grafted cells. (G) *In-vitro ctsk-cre*$^{+}$*;mTmG* cells cultured in the hollow space of the cast $CaSO_4$ cement shows viable and proliferating cells. (H) X-ray image of tibial stump post amputation after grafting with $CaSO_4$ cement, *ctsk-cre*$^{+}$*;mTmG* cells & rBMP2 protein.

Title: Pregnancy and Lactation Associated Osteoporosis: A Systematic Review

Authors: Madison L. Weckerly BS[1], Cailan L. Feingold BS[1], Naitik K. Singh BS[1], Mary K. Fatehi BS[1], Robert Abrahams BS[1], Daniel A. Mirzai BA1, Adi Cohen MD[2], Anna Cooper MD MPH[3]

Affiliations: New York Medical College[1], Columbia University[2], Montefiore Einstein[3]

Background: During pregnancy and lactation, most of the changes in mineral metabolism to provide fetuses with sufficient calcium are clinically silent; however, the decrease in bone mineral density causes pregnancy and lactation associated osteoporosis (PLO) with a reported instance of 4-400 per 1 million pregnancies. This the first systematic review conducted on this condition affecting the hip to the authors' best knowledge.\

Methods: A comprehensive literature search of the databases Embase, PubMed, and Web of Science, was conducted from August to September of 2024. The articles included for review were case studies or case series that consisted of pregnant patients with PLO of the hip. Data extraction was performed on the resulting 64 studies, totaling 149 patient cases.

Results: The average age reported was 33.5 years, with an average BMI of 26.5 kg/m2 and an average height of 165.8 cm. Symptom onset was reported in 50% of cases, 69% in the 3rd trimester, 25% in the 2nd trimester, and 4% in the postpartum period. The route of delivery was a cesarean section (CS) in 44% of cases, vaginal delivery in 33%, and unreported in 23%. The most common treatment was modified weight-bearing (40%), followed by physical therapy (30%), vitamin D and/or calcitriol (26%), and surgery (26%). Risk factors noted include tobacco use in 15% of cases and a history of abortion or miscarriage in 3% of cases. Cortical defects described as fractures occurred in 28% of cases, and of those 35% were bilateral fractures. An MRI result indicating bone marrow edema was reported in 85% of cases.

Fractures	Number of Cases	Percentage of Cases
Femoral neck fracture	36	71%
Subcapital specifically	**19 of 36**	**53% of 71%**
Femoral head	4	10%
Acetabulum	2	2%
Inter Trochanteric	1	2%
Unspecified	7	14%
Sacral	1	2%
Total Fractures	51	
Bilateral	10	24%
Right	11	27%
Left	12	29%
Unspecified/Not Applicable	8	20%
Total Cases with Fractures	41	28%

Conclusions: In cases with a reported route of delivery, CS occurred at a greater percentage (44%) when compared to the US population in 2023 (32.1%). Some cases described the decision to undergo a CS due to either pain or fracture. This could have implications for the health of the mother and the fetus. The majority of cases occurred during pregnancy. This may complicate the diagnosis and care of the patient in an attempt to reduce fetal exposure to imaging modalities and treatments with known or unknown teratogenic effects. The importance of exercise in improving patient outcomes during pregnancy may be complicated in these cases, as the most prescribed treatment was modified weight-bearing, and 16% of cases prescribed bed rest. The absence of metabolic disease workup details in these cases is an area for future research and clinical focus.

Congenital Scoliosis: An Update to Its Natural History and Clinical Approach

Mihir Sharma[1], Alexander Bhatt MS[1], Jason Brenner[1], Ashlyn Callan MS[1], Priya Singh MD[1], Edina Gjonbalaj[1], Pediatric Spine Study Group, Jacob Schulz MD[1], Leila Alvandi PhD[1], Jaime Gomez MD[2]
[1]Montefiore Einstein Dept. of Orthopedic Surgery, [2]Nicklaus Children's Pediatric Specialists

INTRODUCTION: Congenital scoliosis exhibits a highly variable natural history. Predictive modeling based on radiographic features could improve individualized care and timing of intervention. The natural history by McMaster and Ohtsuka remains the framework for scoliosis treatment, and we sought to confirm and expand upon it. We assessed X-Ray images obtained from a large cohort of patients to develop and validate a data-driven model to predict curve progression in congenital scoliosis.

METHODS: This retrospective multicenter study included 464 patients with congenital scoliosis with baseline and follow-up X-rays. Patients with neurological conditions were excluded. Deformities were classified using McMaster's system. The primary outcome was a Cobb angle ≥50° assessed at final follow-up. A Kaplan-Meier survival analysis was used to analyze curve progression by deformity type. A Chi-squared Automatic Interaction Detection (CHAID) decision tree was used to find predictors of progression based on baseline Cobb angle and deformity type. A multivariable logistic regression model was used to assess independent associations between progression and baseline age, and gender. A receiver operating characteristic (ROC) analysis was performed to assess the accuracy of baseline Cobb angle cutoffs in predicting progression to ≥50°.

RESULTS SECTION: Of the participants included, 261 (56.3%) were female. The mean baseline and follow-up ages were 3.5 ± 3.5 years and 8.8 ± 4.7 years, respectively. Most patients underwent surgical correction (55.3%), followed by observation (40.1%) or casting/bracing (4.5%). Baseline and follow-up Cobb angles averaged 46.5° ± 18.9° and 51.3° ± 22.9°, respectively. The Kaplan-Meier analysis found unilateral unsegmented bars with and without hemivertebra (HV) were at greatest risk of progression. CHAID analysis revealed baseline Cobb angle as the strongest predictor of progression through recursive analysis in determining the following cutoffs:
Cobb ≤38°: Low progression risk (20.8%), especially in block vertebra, incarcerated HV, and complex anomalies (6.9%).
Cobb 38–54°: Moderate progression risk (53.2%), with higher risk in patients with semisegmented HV, wedge, and unilateral unsegmented bar deformities (70.6%).
Cobb >54°: High risk of maintenance at >50° (92.2%) regardless of deformity type.
ROC analysis confirmed strong predictive accuracy (AUC = 0.85). Multivariable logistic regression model confirmed that higher baseline Cobb angle (OR 1.12 per degree increase, $p < 0.001$), deformity type ($p = 0.041$), and female gender (OR 2.02, $p = 0.006$) were independent predictors of progression.

DISCUSSION: Baseline Cobb angle is a robust predictor of curve progression in congenital scoliosis. Deformity classification adds prognostic value in mid-range curves.

SIGNIFICANCE/CLINICAL RELEVANCE: These findings offer a clinically applicable framework for early risk stratification and individualized treatment planning.

REFERENCES:

1. McMaster, MICHAEL J., and Kuniyoshi Ohtsuka. "The natural history of congenital scoliosis. A study of two hundred and fifty-one patients." *JBJS* 64.8 (1982): 1128-1147.

2. Herring, John A. *Tachdjian's Pediatric Orthopaedics: From the Texas Scottish Rite Hospital for Children: 2-Volume Set*.Elsevier Health Sciences, 2020.

FIGURES:

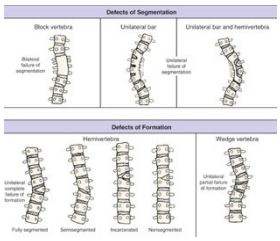

Figure 1: Classification Examples from our Current Understanding of the Natural History of Congenital Scoliosis. If the deformity did not fall into these classifications or was an amalgamation of 4 or more distinct, separate classifications, it was classified as "complex". This figure was taken from Tachdjian's Pediatric Orthopaedics: From the Texas Scottish Rite Hospital for Children: 2-Volume Set.

Mature-like Intervertebral Disc Cells Compromise the Extracellular Matrix to Attenuate Injury-Induced Inflammatory Signaling and Myeloid Cell Recruitment

Tori Kroon[1], Jazz Munitz[2], Anna Ranzenigo[2], Martin Umali[2], William Wang[2], Jonathan Huang[1], Abraham J.P. Teunissen[2,3,4], Nilsson Holguin[1]
[1]Leni & Peter W. May Department of Orthopaedics, [2]BioMedical Engineering & Imaging Institute, [3]Cardiovascular Research Institute, [4]Icahn Genomics Institute, Icahn School of Medicine at Mount Sinai, New York, NY
Tori.kroon@icahn.mssm.edu

Disclosures: Tori Kroon (N), Jazz Munitz (N), Anna Ranzenigo (N), Martin Umali (N), William Wang (N), Jonathan Huang (N), Abraham J.P. Teunissen (N), Nilsson Holguin(N)

INTRODUCTION: Intervertebral disc (IVD) degeneration (IVDD) is a leading cause of chronic low back pain (cLBP) and both are accentuated by aging.[1] Aging promotes a mature IVD cellular phenotype[2] and is also associated with impaired healing and chronic inflammation,[4] highlighting the specific need to study the role of aging in the regulation of IVD inflammation and immune cell recruitment. Wnt signaling is responsible for IVD cell differentiation and activity, where aging and IVD injury reduce Wnt signaling in IVD cells and promote IVD cell maturation,[5] but its subsequent functional role in IVD injury is unclear. Wnt signaling-replete IVD cells are better equipped to promote the extracellular matrix and IVD function[2] and, by contrast, in vitro suppression of Wnt signaling in IVD cells is anti-inflammatory[6]. Therefore, we hypothesized that injury in Wnt signaling-deficient IVD cells that model mature IVD cells will reduce inflammatory signaling and immune cell recruitment.

METHODS: All experiments were IACUC-approved. To suppress Wnt signaling, tamoxifen-inducible ShhCreERT2 mice, which target the nucleus pulposus, were crossed with β-Catenin$^{fl/fl}$ mice to target the Wnt signaling transcription factor. 5-month-old female ShhCreERT2/β-Catenin$^{fl/fl}$ (cKO, n=3) and littermate β-Catenin$^{fl/fl}$ (wildtype control, WT, n=3) were subjected to a model of IVD degeneration by 1 week of tail compression (TC). Two adjacent IVD, that were not compressed, served as internal controls. The whole IVD transcriptome was analyzed by bulk RNA sequencing (n=3/group; RIN: 6.4 ± 0.8; 26.7 million reads/sample). Separately, tamoxifen-inducible AcanCreER^{T2} mice were crossed with β-Catenin$^{fl/fl}$ mice. 5-month-old male and female AcanCreERT2/β-Catenin$^{fl/fl}$ (IVD specific deletion, cKO, n=2 per sex) and β-Catenin$^{fl/fl}$ (wild-type, WT, n=2 per sex) were subjected to 1 week of TC. A wider IVD-targeting cre was used to model IVD age-related loss of Wnt signaling. These latter mice received pre- and post-TC PET/CT scans to track myeloid-derived cells. Mice received a retro-orbital injection of 89Zr-labeled PERFECTA-HDL at a dose of 100 ± 10 µCi 24 hours prior to PET/CT imaging (Meidso nanoScan).[7] Plots and pathway analysis were constructed using RStudio, Excel and Prism. FDR<0.1 and p-val<0.05 were statistical thresholds.

RESULTS: Nucleus pulposus-specific deletion of β-catenin shifted the transcriptomic in response to IVD injury. Pre-injury, WT and cKO mice had overlapping transcriptomes on PCA. However, when comparing the injury response of both groups, there is no overlap of samples indicating a distinct response to injury (Fig. 1A). Pathway analysis revealed that in WT IVD, injury distinctly upregulated MCP1 production, a gene associated with monocyte/macrophage migration and infiltration (FE=4.5, FDR=0.03), while injury did not regulate this pathway in cKO IVDs (Fig. 1B). Additionally, injury distinctly upregulated extracellular matrix constituent secretion, in WT IVD (FE=7.5, FDR=0.001) while not regulating this pathway in cKO IVD (Fig. 1C). 89Zr-labeled PERFECTA-HDL targeted phagocytosis in myeloid derived cells allowing visualization of these cells with PET imaging (Fig. 1D). At baseline, WT and IVD-specific β-catenin deletion had similar mean standard uptake (SUV) of the tracer intensity and show similar levels of myeloid cells at the coccygeal IVD. IVD injury increased myeloid-derived cell recruitment to the injury site by over 460% in WT mice ($p<0.05$) and IVD-specific deletion of β-catenin attenuated this increase by over 60% (Fig. 1D'). Staining for neutrophil-specific marker Ly6G/C is currently ongoing.

DISCUSSION: We identified a new potential cellular crosstalk mechanism between mature-like IVD cells and myeloid-derived cells in response to injury by which mature IVDs may compromise the IVD extracellular matrix and IVD function to mitigate inflammatory signals and immune cell recruitment. The potential reason for why mature IVD cells mitigate myeloid cell recruitment could be to mitigate the systemic age-related inflammation and neutrophil accumulation that occurs with 'inflammaging,[7] which is a potential mechanism for painful IVDD.[8]

SIGNIFICANCE/CLINICAL RELEVANCE: The transcriptomic response of inflammatory genes to IVD injury and immune cell recruitment is differentially regulated by age and treatment for painful IVDD may need to be age-dependent.

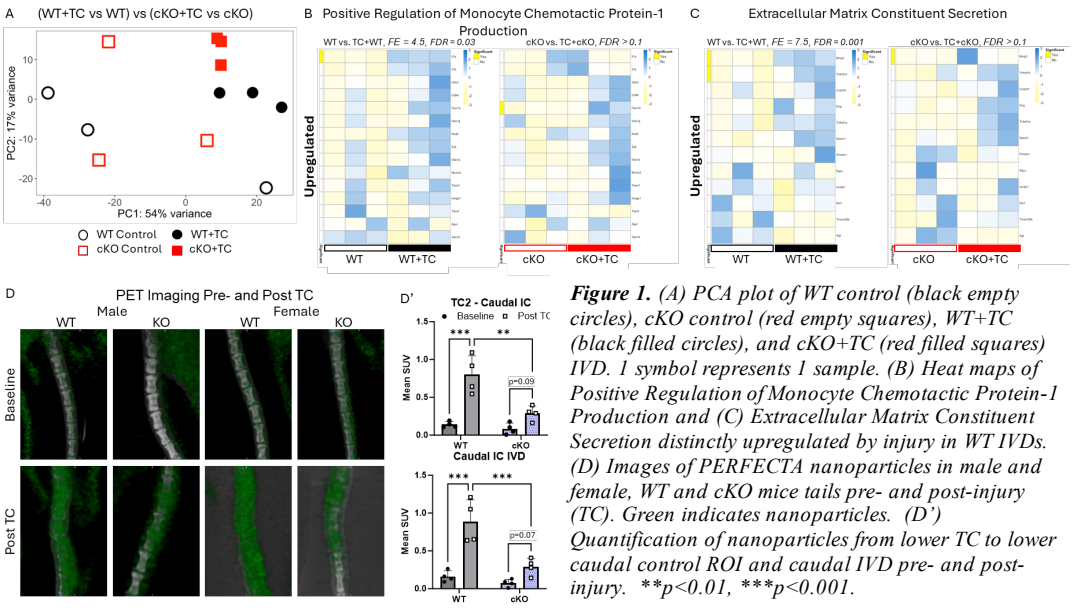

Figure 1. *(A) PCA plot of WT control (black empty circles), cKO control (red empty squares), WT+TC (black filled circles), and cKO+TC (red filled squares) IVD. 1 symbol represents 1 sample. (B) Heat maps of Positive Regulation of Monocyte Chemotactic Protein-1 Production and (C) Extracellular Matrix Constituent Secretion distinctly upregulated by injury in WT IVDs. (D) Images of PERFECTA nanoparticles in male and female, WT and cKO mice tails pre- and post-injury (TC). Green indicates nanoparticles. (D') Quantification of nanoparticles from lower TC to lower caudal control ROI and caudal IVD pre- and post-injury. **p<0.01, ***p<0.001.*

REFERENCES: [1]Adams, M and Rouhgley,P. *Spine.* 2006. [2]Holguin, N and Silva, M. *FasebJ.* 2019. [4] Sendama, Wezi. *Aging Research Reviews.* 2019. [5] Holguin, N, et al. *J Appl Physiol.* 2014. [6]Hiyama, Akihiko et al. *Arthritis Res & Ther.* 2013. [7]Bartlett DB, et al. *Aging Cell.* 2012. [8]Parisien, M. et al. *Sci Transl Med.* 2022.

ACKNOWLEDGEMENTS: This project was funded by NIH/NIAMS (NH) - R01 AR078764.

Treatment with Parathyroid Hormone Does Not Attenuate Osteoarthritis Progression Following Daily Loading

Omar Dervisevic[1], Ana Witkowski[1], Marjolein C. H. van der Meulen[1,2]
[1]Cornell University, Ithaca, NY [2]Hospital for Special Surgery, New York, NY

Introduction: Osteoarthritis (OA) patients primarily seek treatment for pain and joint dysfunction. Early-stage OA involves increased bone remodeling, highlighting subchondral bone as a therapeutic target. Parathyroid hormone (PTH), an FDA-approved anabolic therapy for osteoporosis, attenuates joint degradation and pain in surgical OA models[1,2,3]. Notably, PTH pre-treatment has been shown to enhance cartilage thickness, increase bone mass, and reduce cartilage damage during mechanical loading[4]. This study examined whether PTH, administered concurrent with damaging daily joint loading, reduces OA-related pain, preserves cartilage, and increases bone mass.

Methods: With IACUC approval, the left hindlimbs of 26-wk-old male C57BL/6J mice underwent 6 weeks of daily cyclic tibial loading (9N, 1200 cycles, 4Hz)[5,6]. The right hind limbs were not loaded and used as contralateral controls. Mice were randomized into 2 treatment groups and injected with saline (VEH, SQ, n=8-10, 5d/wk) or PTH (40µg/kg/day, SQ, n=8-10, 5d/wk) immediately following each bout of loading. Static weightbearing was performed every 2 weeks to measure load distribution between right and left hindlimbs. Mice were euthanized 6 weeks after the start of loading; knees were dissected and prepared for microCT imaging and Safranin-O staining[3]. Cancellous bone in the epiphysis and cortical bone of the subchondral plate was analyzed by microCT. Cartilage damage in the tibia was quantified by OARSI scoring of Safranin-O-stained slides for total plateau and posterior and anterior compartments. Using a linear mixed-effects model with Tukey post-hoc analysis, Treatment and Loading effects on OARSI scores and bone morphology, as well as Treatment, Loading, and Duration effects on static weight-bearing, were determined.

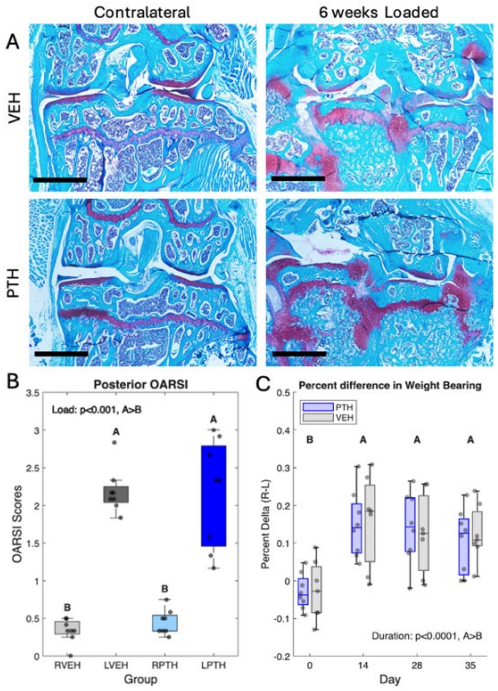

Figure 1: A) Representative sections of the proximal tibia of loaded and control limbs for VEH (Top) and PTH (Bottom) treatments.
B) OARSI Scores in the posterior compartment of the tibia increased with daily loading;
C) Load-bearing on the contralateral limb increased with experimental duration as measured by static weightbearing (% difference R-L).

Results: After 6 weeks of daily loading, significant cartilage damage was observed, particularly in the posterior-medial tibial compartment, with no improvement from PTH treatment. (Figure 1A,B). Over the 6 weeks hindlimb weightbearing shifted to an increased reliance on the contralateral limb. PTH treatment did not alleviate this pain-related behavior (Figure 1C). Loading decreased the epiphyseal bone volume fraction (BV/TV), epiphyseal tissue mineral density (TMD), trabecular number (Tb.N), trabecular thickness (Tb.Th), cortical thickness (Ct.Th), and cortical TMD. As expected, PTH increased the epiphyseal BV/TV (Fig. 2A). The effect of loading on epiphyseal TMD differed with PTH treatment, which increased the reduction in bone mass in loaded limbs (Fig. 2B).

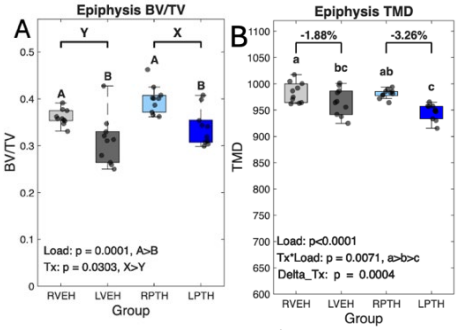

Figure 2: A) Epiphyseal BV/TV decreased with loading (A>B) and increased with PTH treatment (X>Y).
B) Loading reduced epiphyseal TMD, moreso with PTH treatment: VEH limbs decreased 1.88% and PTH-treated limbs decreased 3.26%

Discussion: In the present study, PTH administration initiated concurrently with load-induced OA did not reduce pain or cartilage damage. In surgical models of OA, PTH treatment reduced pain and cartilage damage[2,3]. Additionally, PTH pretreatment had beneficial effects on both bone and cartilage in load-induced OA[4]. These differences across preclinical OA models may stem from the effects of mechanical loading on cartilage and/or the combined impact of PTH and loading on cartilage health. PTH treatment increased bone mass in the epiphysis, reflecting its anabolic effect on bone. Loading reduced epiphyseal TMD, indicating bone remodeling, with a greater reduction in PTH-treated limbs, perhaps highlighting an enhanced remodeling response to combined PTH and loading. Although tibial microarchitecture improved, cartilage damage and pain-related behaviors were not attenuated with combined daily loading and PTH administration, suggesting that our prior results reflected improved cartilage properties with PTH pretreatment. The mechanisms underlying the effects of PTH treatment on cartilage with loading merit further investigation.

Significance: No disease-modifying treatments exist for OA. PTH reduces cartilage damage in surgical models but has not been studied in load-induced OA.

References: [1]Yuan+ 2014, [2]Sun+ 2021, [3]Sampson+ 2011, [4]Antoinette & Ziemian+ 2024, [5]Fritton+ 2005, [6]Ko+ 2013

Acknowledgments: Funding provided by NIH R01-AR081943. We thank Dr. Soph Ziemian and the Cornell CARE team.

Posterior Lumbar Fusions with Adjacent Laminectomies: Outcomes and Radiographic Alignment

Janet Hsu, BS[1]; Rami Z. AbuQubo, BS[1]; Ahsan S. Ahmed, BS[1]; Mitchell S. Fourman, MD, MPhil[1]
[1] *Department of Orthopaedic Surgery, Montefiore Medical Center, Bronx, NY*

Objectives
Lumbar fusions can be done to help correct sagittal alignment. Laminectomies may be done at the same or an adjacent level to decompress the spine. This study aims to analyze how adjacent laminectomies may influence outcomes after posterior lumbar fusions, including revision rates, complications, and radiographic sagittal alignment and spinopelvic parameters.

Methods
A retrospective case-control study was conducted for patients who received a 1-3 level posterior lumbar fusion from seven spine surgeons from 2021 to 2024. Patients in the adjacent laminectomy group were propensity-score matched by age, BMI, level of spinal surgery, and open vs. minimally invasive surgery. The final cohort included 23 patients in the adjacent laminectomy group and 51 patients in the non-adjacent laminectomy group. Complications and rates of revision surgery were analyzed. Lumbar lordosis and pelvic tilt were measured by two independent and blinded raters from sagittal radiographs for patients with imaging.

Results
Demographics (sex, age at surgery, BMI, and race) between the two groups were not significantly different between the two groups. Two patients (8.7%) in the adjacent laminectomy group had numbness post-operatively compared to 5 patients (9.8%) in the non-adjacent laminectomy group. The non-adjacent laminectomy group also had 1 patient with both sensory and motor deficits post-operatively ($p = 0.8$). Three adjacent laminectomy patients (13.0%) had revision fusion procedures with extension or revision of hardware, compared to zero in the non-adjacent laminectomy group ($p = 0.03$). The average time to revision surgery was 24 months. Adjacent laminectomy patients had an average lumbar lordosis of 50.5 ± 4.9 pre-operatively and 48.0 ± 8.4 one-year post-operatively ($p = 0.2$). Non-adjacent laminectomy patients had an average lumbar lordosis of 48.0 ± 15.2 pre-operatively and 48.5 ± 14.2 one-year post-operatively ($p = 0.8$). Adjacent laminectomy patients had an average pelvic tilt of 20.0 ± 3.2 pre-operatively and 23.2 ± 9.1 one-year post-operatively ($p = 0.4$). Non-adjacent laminectomy patients had an average pelvic tilt of 23.1 ± 11.0 pre-operatively and 23.6 ± 10.1 one-year post-operatively ($p = 0.8$).

Discussion and Conclusion
Patients with adjacent laminectomies had comparable complication rates but a significantly increased rate of revision surgery compared to non-adjacent laminectomy patients. The adjacent laminectomy group had an increased change in average pelvic tilt and lumbar lordosis post-operatively. While these differences were not significantly different, it is possible that clinically, there is increased compensation of the spine due to changes in alignment, increasing the rates of revision surgeries.

Proton Pump Inhibitor Use is Associated with an Increased Risk of Extensor Tendon Rupture in Patients With Gastroesophageal Reflux Disease

Joseph Bisiani (BS) [1], David E. Komatsu (PhD) [1]
[1] Department of Orthopaedics, Renaissance School of Medicine at Stony Brook University, Stony Brook, NY, 11790

Aims:
Proton pump inhibitors (PPIs) are among the most frequently prescribed therapies for gastroesophageal reflux disease (GERD), yet emerging data suggest their use is associated with adverse effects on connective-tissue. PPIs raise gastric pH and reduce copper absorption, impairing lysyl oxidase activity, an enzyme essential for collagen cross-linking in tendons. Extensor tendons are smaller and weaker than flexor tendons, though still critical for hand function, and minor losses in collagen integrity could result in extensor tendon rupture. However, the relationship between PPI exposure and extensor tendon rupture has not been examined in a large real-world population. Therefore, we investigated whether PPI use in GERD patients is associated with an increased risk of extensor tendon rupture and explored potential sex-based differences.

Methods:
We performed a retrospective cohort study using the TriNetX Research Network, a global federated database of de-identified electronic health records (>100 million patients). Adult patients with a diagnosis of GERD were stratified by documented PPI exposure. Propensity score matching (1:1) controlled for age, sex, and comorbidities (Rheumatoid Arthritis, Type 2 Diabetes Mellitus, long term steroid usage, Chronic Kidney Disease, adverse reaction to antibiotics, orthopedic joint implants, and distal radius fractures) relevant to tendon health. The primary outcome was incident extensor tendon rupture identified by ICD-10 codes. Risk ratios (RR) with 95% confidence intervals (CI) were calculated, with significance set at $p < 0.05$.

Results:
After matching, 3,539,814 patients were included in the generalized cohort, with sex-specific sub-analyses of 1,457,413 males and 2,080,425 females. PPI use was associated with a **43.8% increased risk** of extensor tendon rupture compared with non-use (RR 1.438; 95% CI 1.346–1.538; $p < 0.0001$). Male PPI users demonstrated a **20.1% increased risk** (RR 1.201; 95% CI 1.090–1.323; $p = 0.0002$), whereas female users exhibited a **74.3% increased risk** (RR 1.743; 95% CI 1.590–1.912; $p < 0.0001$).

Conclusions:
PPI therapy in GERD patients is significantly associated with an increased risk in extensor tendon rupture, with a markedly greater risk observed in females. Potential mechanisms include copper-mediated impairment of collagen cross-linking and sex-specific differences in tendon biology or medication metabolism. Given the widespread, often long-term use of PPIs, these findings highlight an under-recognized musculoskeletal risk with important public-health and orthopaedic implications and warrant prospective studies of copper status, tendon health, and safer acid-suppression strategies.

Understanding Lineage Capacity of Blastema-Driven Craniofacial Joint Regeneration

Authors: Everett Weinstein[1,2], Maria Blumenkrantz[1,2], Joanna Smeeton[1],
Affiliations: [1]Columbia Stem Cell Initiative, Department of Rehabilitation and Regenerative Medicine, Department of Genetics and Development, Vagelos College of Physicians and Surgeons, Columbia University Irving Medical Center, Columbia University; New York, NY 10032, USA, [2]Columbia University Integrated Program in Cellular, Molecular, and Biomedical Studies

Objective: Humans cannot naturally repair joint tissues after injury or aging-dependent tissue degradation. However, we find that Zebrafish have lubricated synovial joints in their jaws and can regenerate hyaline cartilage, supportive ligaments, as well as joint morphology and function after total joint resection[1–3]. We previously described that following a complete joint resection injury, adult zebrafish restore tissue morphology and joint function within 2 months[3]. This regeneration is driven by a transient population of cells that form at the site of injury known as a blastema. Unlike single plane amputation models with unilateral regenerative growth from a single blastema, our avulsion-style injury model features multiple sites of blastema-driven regeneration that provide a unique patterning with the three blastema proliferating to meet near the center. These three blastema may be interrogated both individually and collaboratively to reveal the regenerative program(s) capable of restoring a functional joint after complete loss. Currently, the cell populations that contribute to the blastema responsible for regenerating the zebrafish jaw joint remain unknown, as does how each of the three individual blastema may influence the composition of the regenerating joint. Using transgenic lines for whole-mount stereoscope and confocal imaging, as well as histological analyses and single cell sequencing, we define molecular markers of the early blastema and track the composition of regenerating joints *in vivo* up to 56 days post joint resection (dpjr). Furthermore, to test the role of cell extrinsic versus cell intrinsic cues in blastemal cell fate bias, we developed a new protocol for zebrafish craniofacial blastema isolation and joint tissue explant culture. The goal of this study was to test whether the anatomical origin of a blastema can influence the composition of the tissue and structure being regenerated.

Methods: Unilateral joint resection surgeries were performed by anesthetizing zebrafish and consisted of three cuts to completely resect the quadrate-articular jaw joint. Histological analyses included hematoxylin & eosin (H&E) staining, and immunofluorescence and smFISH experiments were performed on 5µm formalin-fixed paraffin embedded (FFPE) tissue sections. Tissue clearing and imaging was achieved through the use of transgenic *thbs4a_p1:eGFP;scxa:mCherry* fish were used to visualize changes in cartilage, ligaments, and tendon during regeneration. *sp7:GFP* transgenic or calcein blue stain were used to label osteoblasts or mineralized bone tissue. Following CUBIC tissue clearing[4], joints were imaged with a Leica SP8 confocal microscope with lightning deconvolution. *In vitro* culture media consisted of low glucose DMEM, 20% FBS, 1% penicillin-streptomycin, and 2% amphotericin B, with atmospheric conditions of 28.5°C, 3% O2, 2.5% CO2.

Results: We find that following whole jaw joint resection, three blastema (anterior, posterior, and dorsal) are induced. Through single-cell RNA sequencing, single-molecule *in situ* hybridization, and PCNA immunofluorescence, we find that blastema cells are broadly marked by transient expression of *fn1a*, *tnfaip6*, and *hmga1a*, and that the three blastema proliferate at approximately similar rates. We first found expression of these genes in periosteal, stromal and bone-adjacent mesenchyme compartments at 1 dpjr, suggesting a potential tissue origin for these blastemal fibroblasts around the resected bones. Histological analysis shows that blastemal cells cap the cut bone ends by 3 dpjr. Blastemal cell proliferation peaks at 3 days-post-injury to fill in the injury space by 1 week following resection (n=6)[3]. Next, to isolate the relative contribution of individual blastema to the regenerating joint, repeat resections were used to prevent two of the three blastema from regenerating, allowing only a single blastema to contribute cells to the regenerate before analyzing regenerate composition at 56 dpjr. Through repeated resections, we found that the anterior blastema more readily forms osteogenic fates (n=5; p=0.0339), with associated reduced formation of *scxa+* connective tissue cell fates (n=5; p=0.043). We find that hypoxic atmospheric conditions as low as 3% O_2 and elevated FBS concentrations as high as 20% promote healthy proliferation of zebrafish blastema cells *in vitro* (n=3), while standard human cell culture conditions of 20% O_2 and 10% FBS resulted in accelerated cell death of the blastemal cells within 7 days (n=8). Using the same cell culture techniques we refined for blastemal cells, explants of the quadrate-articular joint survived and maintained *scxa+* ligament identity *ex vivo* for up to 14dpjr (n=3). After performing whole joint resections and allowing the three blastema to proliferate out to 4dpjr, we then surgically isolated the blastema and chemically dissociated them before growing the combined blastemal cells in culture. We then observed an *in vitro* bias to adopt *sp7+* osteogenic fates by 21 days when all blastema are cultured together (n=3).

Conclusions and Significance: Previously we showed *de novo* articular joint formation in zebrafish following a complete joint resection, here we investigated how the three blastema function cooperatively or independently when restoring all mature joint tissues during regeneration. Through repeat resections we observed differential tissue composition of the regenerating joint, with anterior blastemal cells biased towards osteogenic fate at the expense of connective tissue fate. This implies that while individual blastema are capable of forming the major joint cell lineages, there is lineage bias in their output *in vivo* depending on injury site differences in blastemal composition. Isolated cell cultures of each blastema suggest that tissue origin may play a pivotal role in regenerative lineage capacity based on etiological origin, potentially defining regenerate composition. By developing new culture conditions that allow for *ex vivo* joint explant and *in vitro* manipulation of zebrafish blastemal cells this study opens possibilities for future assays to probe cell-intrinsic lineage fate commitment biases in regeneration and define the cues that drive articular cartilage and ligament fate from blastema cells. Taken together, our results define the molecular signature of joint blastema cells and probe the lineage biases of blastema-driven regeneration of joint tissues.

References: [1] Smeeton, J. *et al.* Regeneration of Jaw Joint Cartilage in Adult Zebrafish. *Front. Cell Dev. Biol.* **9**, (2022). [2] Anderson, T. *et al.* Ligament injury in adult zebrafish triggers ECM remodeling and cell dedifferentiation for scar-free regeneration. *Npj Regen. Med.* **8**, 1–15 (2023). [3] Blumenkrantz, M. *et al.* Dynamic cell fate plasticity and tissue integration drive functional synovial joint regeneration. 2024.12.12.628180 Preprint at https://doi.org/10.1101/2024.12.12.628180 (2024). [4] Susaki, E. A. *et al.* Whole-Brain Imaging with Single-Cell Resolution Using Chemical Cocktails and Computational Analysis. *Cell* **157**, 726–739 (2014)

Distinct Neutrophil Populations Support Regenerative Healing In Neonatal Mice

Timothy D. Jacobsen[1*], Timothy Hoang[1], James Hong[1], Levon Rodriguez[1], Irina Heggli[1], James C. Iatridis[1]
[1]Ichan School of Medicine at Mount Sinai, New York, NY *Timothy.Jacobsen@mssm.edu

Disclosures: The authors have no potential conflicts to this work.

Introduction: Back pain and disability are associated with intervertebral disc (IVD) degeneration and herniation, and these conditions increase with age [1]. Aging involves changes to IVD cells, extracellular matrix composition, structure, and function that impact healing [2]. In mice, IVDs with a critically-sized herniation-type injury healed regeneratively in neonates and fibrotically in adults [3]. This transition from regenerative IVD healing to fibrosis occurs between postnatal day p14 and p28, with bulk-RNA-seq analyses implicating changes to the IVD immune cell response [4]. Last year, we determined that resident IVD neutrophils are lost with age and implicated in neonatal mouse IVD regeneration [5]. This year, we test the hypothesis that IVD neutrophil phenotypes shift with aging and injury, and play a mechanistic role in IVD healing. This study aims to: (1) determine effects of age and injury on immune cell sub-populations; (2) investigate changes in neutrophil phenotype between regenerative and nonregenerative ages; (3) Mechanistically observe importance of neutrophils in regenerative IVD healing by knocking them out prior to injury in neonatal mice.

Methods: *single cell RNA sequencing (scRNA-seq):* Naïve and Injured mouse coccygeal IVDs were analyzed at 4 age groups: 0.5 Month (0.5 Mo, neonatal mice capable of regenerative healing), 4 Mo (skeletal maturity, young adult), 12 Mo (adult) and 24 Mo (aged, peak back pain prevalence). Injury involved a critically-sized AF-herniation created using 26- or 30-gauge needle (scaled with age to adjust for IVD size). IVDs were dissected and analyzed at 14 days post-injury (dpi) when immune-modulated healing responses are prominent and healing patterns are predictive of steady-state responses. For each group, cells were isolated and pooled from 6 mice with 6 IVDs per mouse. Data from all samples were integrated, clustered and visualized using uniform manifold approximation and projection (UMAP). A distinct immune cell subset was identified, and re-clustered to further characterize immune cell phenotypes. *Flow Cytometry:* Cells were isolated from naïve coccygeal IVDs of 0.5 Month (regenerative) and 1 Month (non-regenerative) mice and stained for Cd45 (Immune Marker), Ly6G (Neutrophil Marker) and CD11b (Activation Marker). Cells for flow cytometry were gated for immune cells (Cd45+) then for neutrophil maturity (Ly6G Hi/Low) and activation state (CD11b +/-). *Neutrophil Depletion:* Neutrophils were depleted from neonatal mice by intraperitoneal injection of a neutrophil depleting αLy6G/Ly6C antibody (BioXCell), depletion was confirmed using Ly6G staining in mouse spleen. Change in disc height index (DHI) was measured in uninjured and injured coccygeal IVDs 14dpi in both control and neutrophil depleted mice using faxitron x-ray. Paraffin histology with H&E and PR-AB staining were used to investigate IVD morphology.

Results: Annotation using canonical markers identified a distinct immune cluster within cell isolated from the IVD, with sub-clusters of neutrophils, macrophages, T Cells and B Cells (Figure 1A). Neutrophils decrease with aging from regenerative (0.5 Mo) to non-regenerative ages (4,12,24 Mo), while neutrophil infiltration was observed following injury in older age (Figure 1B). Four distinct neutrophil sub-clusters were identified and neutrophils from naive neonatal IVDs were predominantly Neutrophil 1 (Neut1) and Neut2 while aged injured samples were mostly Neut3 and Neut4 was distributed across age and injury state (Figure 1C & 1D). Neutrophils clusters had distinct phenotypic expression with Neut1 and Neut2 being less mature and expressing higher levels of cysteine protease inhibitors (Figure 2A). Flow cytometry confirmed neutrophil populations from regenerative ages (0.5 Mo) were phenotypical distinct from non-regenerative ages (1 Mo) showing higher proportions of immature (Ly6G Lo) activated (Cd11b +) neutrophils with an increase in neutrophil maturity by 1 Mo (Figures 2B & 2C). Injury in neutrophil depleted 0.5 Mo neonates caused inferior healing from injury with IVD compaction, decreased cellularity, and greater glycosaminoglycan loss (Figure 3A) as well as significantly decreased DHI (Figure 3B).

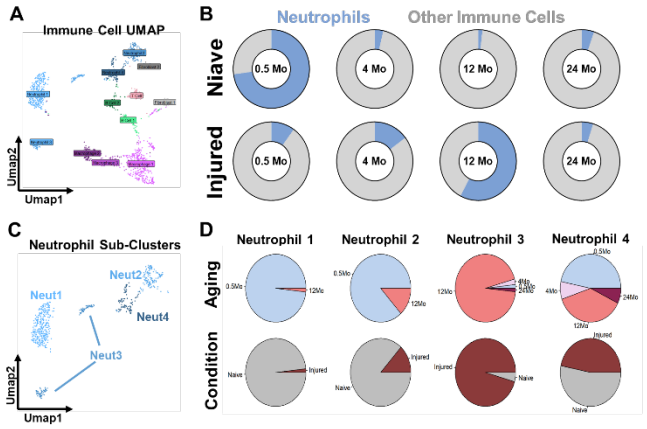

Figure 1: Immune cell sub-clustering of scRNA-Seq in mouse coccygeal IVDs identified (A) distinct immune cells populations that were (B) predominantly neutrophils in naïve neonates and increased with injury in adult and aged IVDs. (C) Neutrophil (Neut) sub-clusters on UMAPS showed (D) Neut1 & Neut2 clusters dominant in naïve neonates and Neut3 dominant in injured adult IVDs.

Discussion: This study determined identified distinct neutrophil populations in naïve and injured mouse coccygeal IVD and determined that neutrophil populations shift with aging and injury, supporting recent studies identifying that neutrophils are an important AF cell response to IVD injury [6]. ScRNA-Seq and flow cytometry determined neutrophils present neonatal (0.5 Mo) mice exhibited an immature phenotype compared to neutrophils present in adult and aged IVDs with a transition to mature neutrophils occurring as young as 1 month. Result point to immature neutrophils playing a mechanistic role in regenerative IVD healing since neutrophil inhibition in neonates worsened IVD healing and since neutrophil populations 1 and 2 neutrophils were nearly absent at later ages and following injury. In contrast, neutrophil population 3 was dominant in aged and injured IVDs and exhibited the highest neutrophil maturation score and least amount of cysteine protease inhibition. Cysteine proteases include Cathepsins and Caspases which play roles in cell senescence, apoptosis, the complement cascade, and terminal complex formation. As such Cysteine protease inhibition could play a role enhancing neonatal IVD regenerative healing, while its absence may impair adult IVD healing. We conclude that neutrophils are phenotypically distinct in naïve neonatal IVDs and injured mature IVDs, and contribute to neonatal regenerative healing capacity. Future characterizations and gain of function experiments will be important to further elucidate functional roles of the distinct neutrophil populations identified in this study and determine how to translate this knowledge into immune modulating therapies for IVD repair.

Significance: A resident neutrophil population was described in neonatal IVDs that is phenotypically distinct differing from recruited neutrophils in injured IVDs at older ages. Neutrophil knockout showed neutrophils contribute to AF regenerative healing implicating suggesting immune modulating therapies is an important area for IVD repair research.

References: [1] Hartvigsen+ Lancet, 2018. [2] Silwal+ Biomolecules, 2023. [3] Torre+ FASEB, 2018. [4] D'Erminio+ iScience, 2024. [5] Jacobsen+ Trans ORS, 2025. [6] Clayton+ Exp Cell Res, 2025.

Acknowledgements: Supported by NIH R01AR080096.

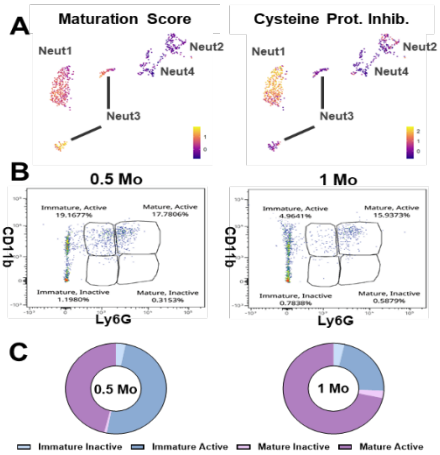

Figure 2: Neutrophil sub-clusters Neut1 & Neut2 were less mature and had higher Cysteine protease inhibition by scRNA-Seq. (B) flow cytometry showed (C) neutrophils in naïve IVDs became more mature as early as 1 month of age.

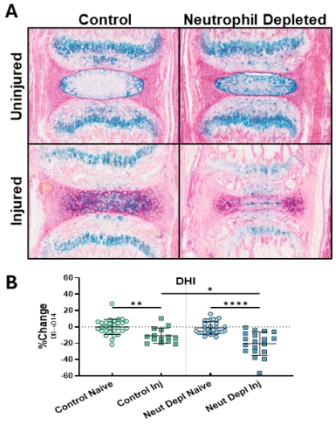

Figure 3: Neutrophil-depletion with systemic antibody treatment in neonates impaired IVD healing at 14dpi as shown on (A) H&E and with (B) DHI.

SerpinA1a is a Novel Age-Related Mediator of Intervertebral Disc Function and Myeloid Cell Recruitment

Joana I. Almeida[1], Amelia Franchin[1,2], Phil Nasser[1], Jonathan Huang[1], Martin Umali[3], Jazz Munitz[3], Tori Kroon[1], Michelle Gelbs[1], Abraham Teunissen[3], Nilsson Holguin[1]

1 Leni & Peter W. May Department of Orthopedics, Icahn School of Medicine at Mount Sinai, New York, NY
2 University of Navarra School of Medicine, Pamplona, SP
3 Biomedical Engineering and Imaging Institute, Icahn School of Medicine at Mount Sinai, New York, NY

Introduction: Patients with alpha-1 antitrypsin deficiency (A1ATD) have increased risk of liver and pulmonary diseases [1], and for unclear reasons, A1ATD is also associated with skeletal complications, including vertebral fractures, osteoporosis, joint dislocation, scoliosis and rheumatoid arthritis at middle age [2-5]. A1AT, encoded by *SERPINA1*, is a serine protease inhibitor of neutrophil chemotaxis and elastase. Mice possess five *SerpinA1* paralogs (*SerpinA1a-e*), and we identified *SerpinA1a* as the most downregulated paralog upon intervertebral disc (IVD) injury in a mouse model of IVD aging. To investigate the role of A1AT in IVD homeostasis and injury, we generated a novel conditional knockout floxed mouse enabling IVD-specific deletion of *SerpinA1a*. We hypothesized that IVD-specific deletion of *SerpinA1a* increases myeloid cell recruitment in naïve and injured IVDs, thereby accelerating structural and functional degradation.

Methods: Naïve 12-month-old *SerpinA1a$^{f/f}$/Acan-cre* (cKO) and *SerpinA1a$^{f/f}$* (WT) littermates of both sexes were used (males: cKO n=8 *vs.* WT n=10; females: cKO n=6 *vs.* WT n=9). Mice were fed tamoxifen *ad libitum* for 4 days to induce deletion of *SerpinA1a*, followed by 4 weeks on normal chow to allow potential IVD remodelling. Readouts included coccygeal IVD histopathology scoring, immunostaining, IVD mechanical testing, micro-computed tomography of vertebrae/endplates/tibia, and gait analysis. For IVD injury experiments, 12-month-old male mice (n=3/group) underwent tail compression-induced IVD injury for 24h [6]. Myeloid cell recruitment pre- and post-injury was assessed by positron emission tomography (PET) imaging following retro-orbital injections of 89Zr-labelled PERFECTA-HDL, which track phagocytic myeloid-derived cells. Each mouse generated 2 control IVD and 2 injured IVD data points. Tamoxifen was administered as above prior to injury. IVD injury severity was scored histologically, and serum levels of A1AT were measured post-injury by ELISA.

Results: Compared to naïve WT mice, cKO mice showed a ~33% increase in IVD degeneration score in males and a ~78% increase in females, along with a 20% reduction in IVD torsional stiffness and a decreased the percentage of A1AT$^+$ cells, particularly in the outer annulus fibrosus. In gait analysis, *SerpinA1a* deletion reduced stride length and increased step frequency, suggestive of a shuffling gait phenotype. Surprisingly, despite targeting ACAN-expressing cells, *SerpinA1a* deletion also reduced vertebral endplate and tibial subchondral bone volume. Under naïve conditions, deletion of *SerpinA1a* doubled IVD myeloid cell intensity at baseline (pre-injury), whereas post-injury levels were comparable between groups. Following IVD injury, deletion of *SerpinA1a* exacerbated IVD degeneration, marked by annulus lamellae disorganization, endplate damage, and reduced A1AT levels relative to naïve counterparts.

Discussion/Conclusion: Our findings identify A1AT as a critical regulator of IVD homeostasis and immune cell recruitment. Because A1AT is known to inhibit myeloid chemotaxis, its loss promoted local inflammation that accelerated IVD degeneration and compromised IVD structure and function. Unexpectedly, *SerpinA1a* deletion also impaired vertebral and subchondral bone health, consistent with delayed bone growth. Given that *SerpinA1a* is expressed in knee chondrocytes, the observed gait deficits may also reflect joint pathology, aligning with reports of arthritis in A1ATD patients [5]. Together, these findings demonstrate that our novel cartilage-specific mouse model not only recapitulates musculoskeletal features associated with A1ATD but also suggests that tissue-intrinsic mechanisms, rather than systemic factors, drive musculoskeletal degeneration. This model provides a powerful platform to advance our understanding of *SerpinA1a* in musculoskeletal biology.

References: [1] Wu Y. et al., JOR Spine. 2021; [2] Velnar T. et al., World J Clin Cases. 2023; [3] Chunyi W. et al., J.Orthop. Translat. 2014; [4] Filipas E. et al., BMJ Case Rep. 2018; [5] Liu W. et al., J Orthop Surg Res. 2021; [6] Carmona-Rivera C. et al., Curr Osteoporos Rep. 2024.

Combined Anti-TNFα and Anti-depressant Treatments Alleviate Pain in Male and Female Rats in a Chronic In-vivo Discogenic Pain Model

Denise Iliff[1], Harsev Singh[1], Irina Heggli[1], Jonathan Huang[1], Venetia Zachariou[2], Andrew Hecht[1], Damien Laudier[1], James Iatridis[1*], Alon Lai[1*]
*equal contributions

[1]*Icahn School of Medicine at Mount Sinai, New York, NY,* [2]*Chobanian and Avedisian School of Medicine at Boston University, Boston, MA*

INTRODUCTION: Back pain is a leading cause of global disability; discogenic pain accounts for ~40% of back pain cases and is driven by intervertebral disc (IVD) degeneration (IVDD) [1]. Annulus fibrosus (AF) injury induced IVDD in a rat model caused persistent IVD inflammation as well as sensitization and neuroinflammation of the spinal cord (SC) dorsal horn highlighting the complexity of discogenic pain [2]. Nevertheless, most current treatments focus on pain management or broad anti-inflammatory approaches with unsatisfactory outcomes. We postulate that treating discogenic pain requires simultaneous targeting of IVDD and SC neuropathy. Etanercept, a TNFα inhibitor, has shown promise reducing inflammation associated with IVD degeneration [3,4]. Duloxetine, an SNRI, has efficacy reducing neuropathic and chronic low back pain, and attenuating SC glial activation in both animal and clinical studies [5–7]. This study applies Duloxetine and Etanercept as combined and individual treatments since these drugs have no known interactions. Furthermore, sex-differences are reported in pain sensitivity, inflammatory responses, and therapeutic outcomes [8]. Therefore, the aims of this study are to assess the effects of Etanercept, Duloxetine, and their combination on chronic discogenic pain in male and female rats using an in-vivo discogenic pain model using measurements of behavior, IVD, and SC. **METHODS:** With IACUC approval, 49 male and 20 female skeletally mature (5-6 month old) Sprague–Dawley rats were randomized into Male; Naïve (n=12), Vehicle (n=13), Duloxetine (n=5), Etanercept (n=4), or Combined (n=13) groups and Female; Naïve (n=6), Vehicle (n=7) or Combined (n=7) groups. All groups except Naïve received AF puncture injury (26G needle with PBS at anterior and left and right lateral punctures with transverse sweeps to increase IVD disruption) to induce severe IVDD at L3-4, L4-5, and L5-6 levels. Naïve animals served as controls. Four weeks post-injury, systemic treatments were administered for 2 weeks: Duloxetine (20 mg/kg, i.p. daily), Etanercept (5 mg/kg, s.c. every 3 days), their Combination, or Vehicle (equivalent saline injections as Combination). Euthanasia occurred at 8 weeks, 2 weeks after treatment. Outputs included von Frey hindpaw mechanical allodynia, IVD height loss, IVDD grading (Safranin-O/Fast-green), spinal macrophages (CD68); and SC staining for neuropeptide (SubP), astrocytes (GFAP), microglia (Iba1), and TNFα. ANOVA with Tukey's post-hoc tests determined effects of treatment for all variables. Random Forest regression identified predictors of withdrawal thresholds using all outputs. **RESULTS:** IVDD decreased hindpaw withdrawal threshold in male and female rats at 2 weeks post-injury and persisted through 4 weeks. Combined therapy restored the withdrawal thresholds to Naïve levels in both male and females (**Fig. 1**). Individual treatment (evaluated only in the male cohort) showed Duloxetine was more effective than Etanercept in restoring the withdrawal threshold to Naïve levels. In the SC, SubP-, GFAP-, Iba1-, and TNFα-ir in the SC dorsal horn were significantly increased in the Vehicle group compared to Naïve (**Fig. 2**). Duloxetine reduced GFAP, Iba1, and TNFα; Etanercept selectively reduced TNFα; and Combined treatment broadly suppressed all four markers (**Fig. 2**). Random Forest identified male SC GFAP, Iba1, and SubP as the top predictors of hindpaw mechanical hypersensitivity, surpassing IVDD grade and spine inflammation measures (**Fig. 3**). No treatments altered male IVD height, IVD degeneration, or spine CD68-ir (not shown). Female cohort SC and spine histology and IVD height measures are in progress. **DISCUSSION:** Combination treatment reduced pain-related behaviors in both sexes although the kinetics of effects was slower in females (even though dosing by weight was identical), and all SC biochemical markers were reduced (in males; female measures are ongoing) further demonstrating combined treatment reduced central sensitization. Individual treatment interventions (in males) showed additive effects, in agreement with animal models where simultaneous targeting of neurotransmitter and cytokine pathways enhanced behavioral recovery in neuropathic injury [6,10]. Duloxetine's modulation of GFAP and Iba1 is consistent with similar findings in radiculopathy and neuropathic pain models [5]. Etanercept's selective TNFα effect parallels clinical and preclinical evidence that systemic anti-TNFα therapy has limited efficacy in established pain unless administered early or locally [9]. Importantly, neither treatment altered IVD height, IVD degeneration, or spine CD68-ir, paralleling clinical observations where symptom improvement can occur without structural repair [6]. Furthermore, Random Forest identified SC GFAP, Iba1, and SubP as the strongest predictors of pain, surpassing IVD measures, reinforcing the SC as a central therapeutic target for IVDD-related pain. Therefore, therapies aimed at modifying IVDD may be more effective if applied in less severe stages of degeneration, delivered locally, or initiated earlier systemically. Future studies should also evaluate longer treatment durations to determine whether chronic IVDD eventually reestablishes pain. We conclude that this combined systemic pharmacological approach has potential to address both neurochemical and inflammatory pathways in chronic discogenic pain yet may be limited for treatment of severe IVDD, as induced in this model. Female cohort SC and IVD assays are ongoing to determine sex-specific mechanisms of action. **SIGNIFICANCE:** Combination Duloxetine and Etanercept alleviated discogenic pain in both male and female rats and reduced SC sensitization and neuroinflammation in males, supporting its potential as a multimodal therapeutic approach for chronic discogenic pain. **REFERENCES:** [1] Fujii+ JBMR Plus 2019; [2] Lai+ Int J Mol Sci 2024; [3] Evashwick-Rogler+ JOR Spine 2018; [4] Cordaro+ Int J Mol Sci. 2022; [5] Handa+ Eur Spine J 2016; [6] Peng+ Spine 2006; [7] Skljarevski+ Eur J Neurol 2010; [8] Mogil+ Nat Rev Neurosci 2020; [9] Bi+ J Dent Res 2022; [10] Watkins+ Nat Rev Drug Discov 2007 **ACKNOWLEDGEMENTS:** Supported by NIH/NIAMS grant R01AR078857 and P30AR079206.

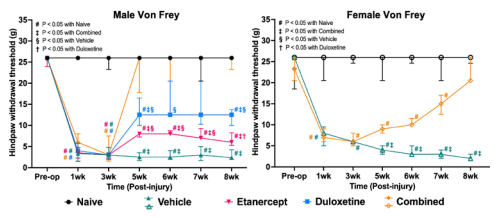

Figure 1. Combination treatment restored VF thresholds in males and females, outperforming monotherapies.

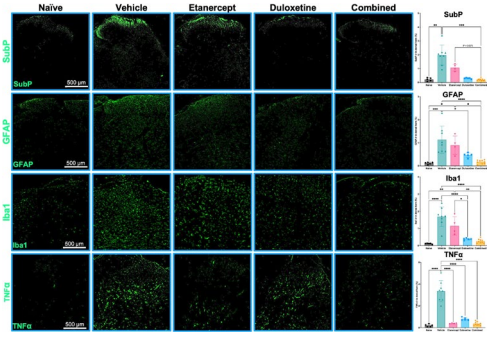

Figure 2. Combination treatment broadly suppressed SC SubP, GFAP, Iba1, and TNFα in males.

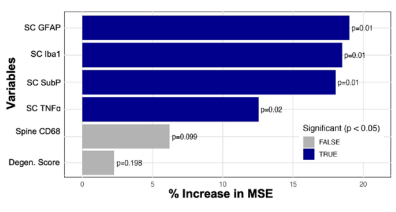

Figure 3. Random forest identified SC markers as strongest predictors of pain behaviors over IVD measures in males.

Higher ASA Score Associated with Complications and Mortality Following Nonunion Surgery

Morgan Roche BS[1], Mihir Sharma BS[1], Mohammed Bashier BA[1], Sirjanhar Singh MD[2], Mani Kahn MD[2]

[1]Albert Einstein College of Medicine, Bronx, NY; [2]Montefiore Einstein Department of Orthopedic Surgery, Bronx, NY

Introduction: The American Society of Anesthesiologists (ASA) physical status classification is commonly used to communicate a patient's comorbidity burden prior to surgery.[1] Various studies have found higher ASA scores to be associated with postoperative complications, complication severity, length of hospital stay, non-home discharge disposition, and total hospitalization cost for orthopedic surgeries.[2-5] The purpose of this study is to determine if higher ASA scores are associated with increased risk of complications following nonunion or malunion surgery.
Methods: We conducted a retrospective cohort study of all patients ≥18 years old with fracture nonunion or malunion of any bone who underwent surgical correction at a large urban health system between November 2015 and June 2024. Outcomes assessed included the incidence of postoperative complications within 90 days of surgery as well as the incidence of specific complications: mortality, vascular complications [including myocardial infarction (MI), venous thromboembolism (VTE), stroke, and transient ischemic attack (TIA)], postoperative infection, sepsis, hardware failure, pneumonia, renal complications (including acute kidney injury and urinary retention), postoperative anemia, nerve complications (including nerve palsy, paresthesia, and complex regional pain syndrome), and gastrointestinal (GI) complications (including Clostridium difficile infection and Ogilvie syndrome). Rehospitalization due to complications was also considered. Fisher's exact tests were used to assess statistical significance.
Results: Of 235 patients with reported preoperative ASA scores, 18.3% (n = 43) had an ASA=1, 53.6% (n = 126) had an ASA=2, 27.2% (n = 62) had an ASA=3, and 0.9% (n = 2) had an ASA=4. Higher ASA score was significantly associated with having one or more complications within 90 days of surgery (p = 0.05). Higher ASA score was specifically associated with a greater incidence of sepsis (p = 0.003), vascular complications (p = 0.023), pneumonia (p = 0.009), and mortality (p = 0.009). Of note, mortality, sepsis, and pneumonia only occurred in patients with ASA scores of 3 or 4. ASA score was inversely associated with GI complications (p = 0.018) and rehospitalization due to complication (p = 0.043). ASA score was not significantly associated with the other specific complications assessed.
Discussion: A higher ASA score is significantly associated with mortality and various life-threatening complications, including MI, VTE, stroke, TIA, pneumonia, and sepsis, following nonunion or malunion surgery. Patient health factors should be carefully considered when developing treatment plans and counseling patients with nonunions and malunions. Limb reconstruction for these conditions can require multiple operations, and patients with severe systemic disease (ASA scores 3 and 4) warrant particular attention when determining surgical indications and strategies.

References:

1. Committee on Economics. (2020). Statement on ASA Physical Status Classification System [Practice Parameter/Standards Statement]. American Society of Anesthesiologists. https://www.asahq.org/standards-and-practice-parameters/statement-on-asa-physical-status-classification-system
2. Meyer, A. C., Eklund, H., Hedström, M., & Modig, K. (2021). The ASA score predicts infections, cardiovascular complications, and hospital readmissions after hip fracture—A nationwide cohort study. Osteoporosis International: A Journal Established as Result of Cooperation between the European Foundation for Osteoporosis and the National Osteoporosis Foundation of the USA, 32(11), 2185–2192. https://doi.org/10.1007/s00198-021-05956-w
3. Ashy, C. C., Morningstar, J. L., Gross, C. E., & Scott, D. J. (2024). The association of ASA score and outcomes following total ankle arthroplasty. Foot and Ankle Surgery: Official Journal of the European Society of Foot and Ankle Surgeons, 30(6), 488–492. https://doi.org/10.1016/j.fas.2024.03.011
4. Kastanis, G., Topalidou, A., Alpantaki, K., Rosiadis, M., & Balalis, K. (2016). Is the ASA Score in Geriatric Hip Fractures a Predictive Factor for Complications and Readmission? Scientifica, 2016, 7096245. https://doi.org/10.1155/2016/7096245
5. Ihejirika, R. C., Thakore, R. V., Sathiyakumar, V., Ehrenfeld, J. M., Obremskey, W. T., & Sethi, M. K. (2015). An assessment of the inter-rater reliability of the ASA physical status score in the orthopaedic trauma population. Injury, 46(4), 542–546. https://doi.org/10.1016/j.injury.2014.02.039

Spatial Transcriptomic Profiling of Osteosarcoma in Clinically Relevant Mouse Model

Harrison Ho [1,2], Sung-Suk Chae [2], Ranxin Zhang [2], Hasibagan Borjihan [2], Abhijith Annasamudram [2], Rui Yang [2], David Geller [2], Chuanyong Lu [2], Deyou Zheng [1], Bang Hoang [2]

[1] Department of Genetics, Albert Einstein College of Medicine, Bronx, NY, USA
[2] Department of Orthopedic Surgery, Montefiore Medical Center, Albert Einstein College of Medicine, Bronx, NY, USA

Objective:
Osteosarcoma (OS) is a common primary bone malignancy. The Rb1/Trp53 double knockout (DKO) mouse model recapitulates the histological and molecular features of human OS, providing a platform for studying disease progression [1]. Spatial transcriptomics combines cellular transcriptomic data with spatial coordinates in tissues, revealing area specific cell interactions and tissue structure. Spatial profiling of metastatic osteosarcoma lung specimens revealed spatial heterogeneity which correlate with five-year survival, highlighting the clinical relevance of spatial organization [2]. In this study we use spatial transcriptomics to characterize the tumor cells and microenvironment heterogeneity in primary tumor and lung metastasis using our mouse model.

Methods:
Four spatial transcriptomics datasets were obtained from two DKO mice using the 10x Genomics Visium platform. For each mouse, paired samples were taken from the femur (primary tumor) and lung (tumor metastases). In collaboration with pathologists, areas of interest were selected, and spot deconvolution data were confirmed. This data was further computationally analyzed using Space Ranger, Seurat, R, and RCTD. RCTD was used for spatial deconvolution utilizing a previously annotated scRNA-Seq dataset[1]. The package ISCHIA was used to group spots into spatial ecotypes according to their cell type composition, as each spot contains anywhere from a few to several dozens of cells.

Results:
Spatial transcriptomics analysis revealed distinct tumor heterogeneity in all samples. Computationally identified cell types matched information from histology. In one lung metastasis sample (Fig. A), tumor nodules were enriched in distinct spots (Fig. B). Utilizing spatial ecotypes to normalize for the different compositions of cell types per spot, we were able to conduct pathway analysis comparing lung metastasis with the primary tumor. Spots with malignant tumor cells in lung metastasis samples were enriched in immune suppression and drug resistance pathways, whereas primary tumor samples were enriched in pathways related to overall cell proliferation and epithelial–mesenchymal transition (EMT).

Conclusions:
Our preliminary findings indicate that tumors exhibit significant heterogeneity both within individual tumors (intratumorally) and between different tumors (intertumorally). These results establish a foundation for understanding the tumor microenvironment and highlight the need for further investigation to develop effective osteosarcoma treatments.

Figures:

A

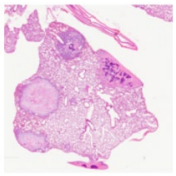

B

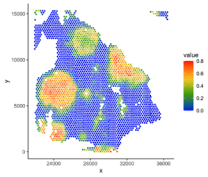

References:

1. Ferrena, Alexander, et al. "Comprehensive single cell transcriptomics analysis of murine osteosarcoma uncovers Skp2 function in metastasis, genomic instability and immune activation and reveals additional target pathways." *bioRxiv* (2024)
2. Lacinski, R.A., et al. Spatial multiplexed immunofluorescence analysis reveals coordinated cellular networks associated with overall survival in metastatic osteosarcoma. *Bone Res* 12, 55 (2024).

The Critical Role of Irisin in Maintaining Bone Health and Its Therapeutic Potential for Diabetic Osteoporosis and Neuropathy

Giulia DiRaimo[1], Hassan Ainani[2], Marcia Urban-Maldonado[3], Jelena Basta-Pljakic[5], Mitchell B Schaffler[5], Sylvia O Suadicani[3,4], David C Spray[2], Mia M Thi[2,3]

Departments of [1]Orthopedic Surgery, [2]Neuroscience, [3]Molecular Pharmacology and [4]Urology, Montefiore Medical Center and Albert Einstein College of Medicine, Bronx, NY, [5]Department of Biomedical Engineering, City College of New York, New York, NY

INTRODUCTION: Peripheral neuropathy and osteoporosis are common diabetes complications resulting in long-term bone and joint pain, motor dysfunction and greater chance of fractures (1,2). Prior studies have recognized the importance of neural control in skeletal development, homeostasis, repair and bone pain, and point to "signaling molecules" acting as messengers between these systems, offering novel therapeutic targets for future approaches to manage diabetic neuropathy and skeletomuscular disorders (3-5). One such molecule is irisin, an adipomyokine released from muscle during exercise that has anti-inflammatory, cell survival and glucose-stabilizing properties (6-8). In previous studies we demonstrated that in type 1 diabetic (T1D) mice the exercise-induced bone anabolic response is impaired and is accompanied by both local bone inflammation and blunted exercise-induced increase in circulating irisin levels (9). We have now investigated the potential role that dysregulated irisin signaling plays in exercise-induced inflammatory response not only in the bone but also in the nervous system, whereby it might contribute to diabetic neuropathy and bone loss. Our objective is to define the role of irisin in maintaining bone health and its impact on joint pain sensitivity, focusing on its therapeutic potential for diabetic neuropathy and bone loss.

METHODS: We used the Akita (C57BL/6J) mouse model of T1D and age-matched wildtype (Wt) mice (8 wk old, male, n=6/group) that were submitted to mechanical loading by treadmill running (1, 2 and 4 wk; 5 days/wk, 300 m/day) during their active phase (nighttime). All animals were euthanized immediately after the last running bout, and femur, blood and sensory dorsal root ganglia (DRGs; L2-L6) were collected. Serum irisin levels were quantified using ELISA (Phoenix Pharmaceuticals). Levels of inflammatory mediators [NLRP3 inflammasome components Nlrp3 and Asc (Pycard)] and pain biomarkers [interleukin-1 beta (Il1b), tumor necrosis factor alpha (Tnfa), nerve growth factor (Ngf), calcitonin gene-related peptide (Cgrp)] in DRG were quantified by RT-qPCR. All experiments were performed under IACUC approval. A second set of Wt and Akita mice was used to prepare DRG cultures that were maintained in normal (1 g/dL; NG) and high glucose (4.5 g/dL, HG), respectively. Ca^{2+} imaging of Fura-2 AM (10µM, Invitrogen) loaded cells and electrophysiological studies were performed on cultured DRG neurons and satellite glial cells (SGCs) in the absence and presence of irisin (100nM, Cayman Chemical). Changes in bone parameters were detected using high-resolution SkyScan 1172 micro-CT system. Cortical bone optical sections from mid-diaphyseal region of femurs were analyzed as previously described (10). Statistical analysis: Data were analyzed from 3-7 independent experiments using Prism 10 (GraphPad). Statistical differences were determined by two-way ANOVA and t-test. $P < 0.05$ was considered statistically significant.

RESULTS: We found that in healthy mice the exercise-induced changes in circulating irisin levels followed a time course that paralleled that of the exercise-induced bone anabolic response (onset at 1 wk and anabolic response at 4 wk of loading), and inversely correlated with the levels of exercise-induced inflammatory mediators (Nlrp3, Asc, Cgrp, Tnfa, Ngf, Il1b) in the DRGs. Notably, these associations and pattern of responses to exercise were lost in diabetic mice. Electrophysiological recordings from cultured DRG neurons showed that while irisin had no effect on the action potential (AP) properties of Wt neurons, it reduced the AP amplitude in T1D neurons. Moreover, irisin decreased the excitability of DRG neurons in T1D mice in a more pronounced manner than in Wt mice. Ca^{2+} imaging experiments revealed that irisin attenuates ATP-induced Ca^{2+} signaling in both DRG neurons and SGCs from Wt and Akita mice.

DISCUSSION: The connection between bone loss and diabetic neuropathy and the mechanisms underlying irisin's modulation of these events are not fully understood. In this study we tested the hypothesis that irisin plays a key role in modulating the exercise-induced inflammatory responses in DRG, DRG neuron excitability, neuron-SGC interactions and ATP signaling. In this context, dysregulation of irisin signaling in the DRG might be one of the factors contributing to diabetic peripheral neuropathy and consequent dysregulation of neural regulation of the bone, which can ultimately contribute to diabetic bone loss. Findings from this study provide initial evidence that irisin signaling can provide a novel target to develop more effective management of diabetic neuropathy and musculoskeletal disorders.

SIGNIFICANCE/CLINICAL RELEVANCE: Identifying novel, personalized risk factors and mechanisms contributing to diabetic osteoporosis and neuropathy is crucial for developing more effective treatments and improving the quality of life for aging individuals with diabetes.

REFERENCES: 1) Ferrari SL+ Osteoporos Int. 2018, 2) Wu B+ Front Endocrinol. 2022, 3) O'Brien PD+ Ilar j. 2014, 4) Brazill JM+ J Bone Miner Res. 2019, 5) Beeve AT+ Current osteoporosis reports. 2019, 6) Slate-Romano JJ+ Mol Cell Endocrinol.2022, 7) Colaianni G+ Proc Natl Acad Sci U S A. 2015, 8) Storlino G+, J Bone Miner Res. 2020, 9) Saw B+ AMRRS Trans 2023. 10) Seref-Ferlengez, Z+ Ann N Y Acad Sci. 2019.

ACKNOWLEDGEMENTS: Supported by R01 AR073475, R01 AR070547 from NIAMS and Montefiore Orthopaedic Research Seed Grant

Effects of Tendon Graft Decellularization in a Murine Model of Anterior Cruciate Ligament Reconstruction

Wataru Morita[1,2], Yuki Suzuki[1], Kyung-Hyun Park-Min[1,2], Scott A. Rodeo[1], and Lionel B. Ivashkiv[1,2]
[1]*Hospital for Special Surgery, New York, NY*
[2]*Weill Cornell Medicine, New York, NY*

INTRODUCTION: Anterior cruciate ligament reconstruction (ACLR) surgery involves replacing the torn ligament with a tendon graft passed through femoral and tibial bone tunnels. Prior pre-clinical studies indicate that graft-derived cells are gradually lost post-operatively, while host-derived cells, primarily from bone marrow and/or synovium, repopulate and contribute to graft healing and remodeling. This study investigated the role of graft-derived cells on ACLR healing using tendon graft decellularization. Drawing a parallel to the "conditioning" process before bone marrow transplantation eradicating native cells and creating space for transplanted cells, we hypothesized that removal of graft cells would facilitate host cell repopulation and improve post-operative healing.

METHODS: All experiments were approved by the Institutional Animal Care and Use Committee. All experiments were performed in 12- to 16-week-old male mice. Twenty-nine and nine C57BL/6J wild-type (WT) and UBC-GFP (GFP expressed ubiquitously in all cells) mice, respectively were used to confirm tendon graft decellularization by the freeze-thaw method.[1] Decellularization was verified by histology and cell counts after tendon tissue digestion. Eighty WT mice underwent ACLR with either naïve or decellularized tendon grafts. Mice were allowed immediate post-operative weight-bearing. The primary outcome measure was ultimate load to failure of the reconstructed knee construct at 4 weeks post-operatively. Secondary measures included gait analysis as a clinically relevant functional outcome measure, plain radiographs for post-traumatic osteoarthritis (PTOA) development graded by the Kellgren-Lawrence scale, micro-CT (µCT) to assess new bone formation within the bone tunnels, and histologic evaluation of bone-to-tendon healing and cell repopulation at 1-, 2-, 4-, and 8-weeks post-operatively. Normal distribution was assessed using the Shapiro-Wilk normality test prior to statistical analysis, and parametric or non-parametric tests were used as appropriate. Statistical significance was set at $p < 0.05$.

RESULTS: Freeze-thaw decellularization removed graft-derived cells without impairing baseline tendon biomechanics. However, ACLR with decellularized grafts showed significantly reduced ultimate load to failure and stiffness at 4 weeks post-operatively. Gait and PTOA scores were unchanged at all investigated timepoints. µCT revealed altered bone microarchitecture by 2 weeks, with increased bone volume by 4 weeks post-operatively with decellularized grafts. Histology demonstrated abnormal bone-to-tendon healing and impaired graft repopulation with decellularized grafts. Notably, graft scraping, which is routinely performed during ACLR to remove excessive soft tissues to achieve a press-fit of tendon to bone, also reduced cellularity to levels comparable with freeze-thaw decellularization.

DISCUSSION: Contrary to our hypothesis, decellularization impaired post-ACLR healing, suggesting the critical roles of graft-derived cells. Decellularized grafts resulted in weaker biomechanics, abnormal bone formation, and poor cellular repopulation. These findings highlight that graft preparation methods, especially scraping, may inadvertently reduce graft cellularity and compromise healing. Preservation of graft-derived cells may be critical for improving post-ACLR outcomes.

REFERENCES: 1. Ikeda et al., J Bone Joint Surg Am. 2010.

Figure 1. Decellularization (Decell.) by the freeze-thaw method. Representative images of (a) calcein AM staining (green), whole tissue and (b) fluorescence (GFP), tissue section. Scale bars: 100 µm. (c) Cell counts after tissue digestion. *$p < 0.05$; ****$p < 0.0001$.

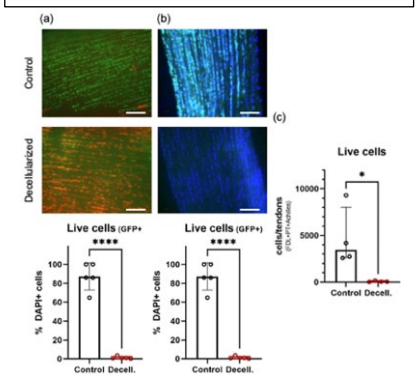

Figure 2. Decellularized (Decell.) grafts impairs post-ACLR healing. (a) Biomechanical testing, (b) µCT analysis of bone formation, and (c) histological assessment including graft cellularity at 4 weeks post-op. Representative images are shown. Scale bars: 200 µm. *$p < 0.05$; ***$p < 0.001$.

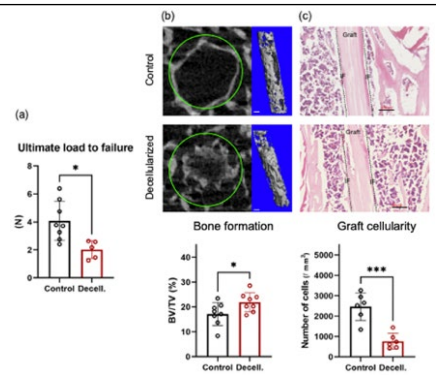

Figure 3. Scraping (Scrape) the graft reduces cellularity. Representative images of (a) calcein AM staining (green), whole tissue and (b) fluorescence (GFP), tissue section. Scale bars: 100 µm. (c) Cell counts after tissue digestion. **$p < 0.01$; ****$p < 0.0001$.

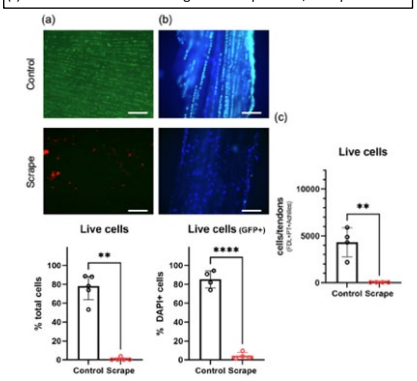

Annulus Fibrosus Progenitor Gene Signature is Conserved in Human, Bovine, and Mouse Intervertebral Discs

[1,2]Levon Rodriguez, [1]Timothy Jacobsen, [2]Robert Sebra, [1]James Iatridis

[1]Leni & Peter May Department of Orthopaedics, [2]Department of Genetics & Genomic Sciences, Icahn School of Medicine at Mount Sinai, New York, NY

INTRODUCTION: Intervertebral disc (IVD) pathologies are major contributors to the global burden of back pain and disability, where annulus fibrosus (AF) defects are a degenerative phenotype contributing to herniation, inflammation, and fibrosis [1]. Current clinical trials of IVD-targeting therapies demonstrate promising pain reduction, but patient outcomes show inconsistent improvements [2, 3], likely reflecting insufficient healing in the absence of clearly defined AF-specific progenitors. We previously defined transcriptomic signatures for bovine AF progenitors (AFPs) using single-cell RNA-sequencing (scRNA-seq) and identified cell culture conditions that enriched this phenotype [4]. As a follow-up, we sought to investigate whether this AFP transcriptomic signature is conserved across species by analyzing mouse and human scRNA-seq datasets. The aims of this study were to: (1) identify AFPs in mouse and human outer AF cells (oAF) with transcriptional entropy profiling and (2) define a conserved AFP gene list using a normalized framework for cross-species transcriptomic comparisons.

METHODS: scRNA-seq datasets from bovine [4], mouse [5], and human [6] IVDs were processed with Seurat. oAF populations were reclustered and analyzed for differential expression. Transcriptional entropy profiling (pySCE) then identified putative stem/progenitor populations [7], and a previously defined bovine AFP population was used as a reference for cluster-level cross-species comparisons [4, 7]. To account for interspecies differences in transcriptome size and baseline similarity, we normalized the Jaccard coefficient between cluster comparisons by the global transcriptome overlap for each species pair. Statistical significance was assessed with a hypergeometric test with Benjamini-Hochberg correction, and a Venn diagram illustrated the intersection of DEGs from the top entropy-scoring clusters.

RESULTS: Clustering resolved 11, 8, and 4 oAF subpopulations in bovine, human, and mouse datasets, respectively. mIVD Cluster 3 and hIVD Cluster 1 exhibited significantly greater transcriptional entropy scores, identifying them as AFP populations (Fig 1). Consistently, these same clusters showed the highest normalized similarity scores relative to the bovine AFP population (Fig 2), indicating strong interspecies conservation between the top entropy-scoring clusters. Comparison of DEGs across bovine, mouse, and human AFPs revealed a shared gene signature of 38 conserved features (Fig 3), including the canonical stem cell-associated marker for nucleostemin, *GNL3*.

DISCUSSION: This study demonstrated the presence of AFP populations across bovine, mouse, and human IVDs, as revealed by the transcriptional entropy profiling that identified mIVD Cluster 3 and hIVD Cluster 1 as AFPs. Our normalized similarity scoring confirmed mIVD Cluster 3 and hIVD Cluster 1 as the most transcriptionally conserved to bovine AFPs, while all other comparisons showed markedly lower, non-significant scores, reinforcing that cross-species conservation is restricted to the top entropy-scoring populations. Within the conserved AFP gene set, *GNL3* was particularly notable given its established role in regulating proliferation and stemness of human mesenchymal stem cells, as well as its expression in rabbit-derived AF stem-like cells [8]. Additional conserved features, including *CNOT3, SAFB, EIF3A,* and *TRIM27*, further suggest a progenitor phenotype with functional programs linked to RNA processing, ribosome biogenesis, and epigenetic regulation of differentiation. The lack of clear extracellular surface markers in this AFP gene set underscores the need to identify generally expressed surface markers for downstream multi-selection sorting, and functional perturbation studies will be needed to establish the regenerative potential of AFPs for AF repair. In conclusion, we identified a novel AFP signature with 38 conserved genes across species, underscoring the translational relevance of preclinical models and advancing AFP-directed repair strategies for disc degeneration.

REFERENCES: [1] Hartvigsen+ *Lancet* 2018, [2] Gornet+ *IJSS* 2024, [3] Beall+ *SpineJ* 2025, [4] Rodriguez+ *ORS* 2025; [5] Jacobsen+ *ORS* 2025, [6] Jiang+ *iScience* 2022, [7] Charytonowicz+ *Nat Comm* 2023, [8] Guo+ *Methods Mol Biol* 2018

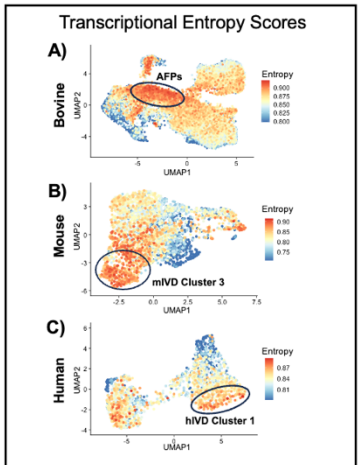

Fig 1: Transcriptional entropy profiling of (A) bovine, (B) mouse, and (C) human scRNA-seq datasets clearly identify the presence of AFPs across species.

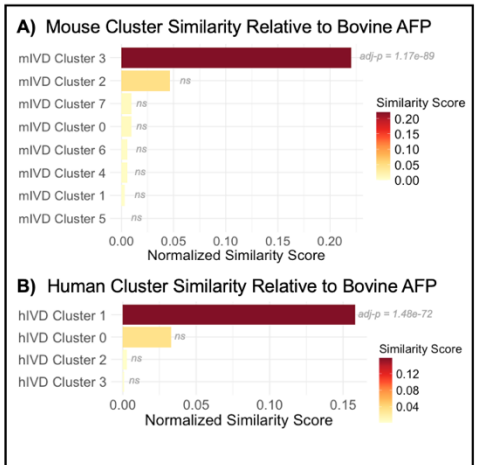

Fig 2: Normalized similarity scores were highest for (A) Mouse Cluster 3 and (B) Human Cluster 1, demonstrating species conservation of an AFP gene signature identified in bovine (ns = non significant).

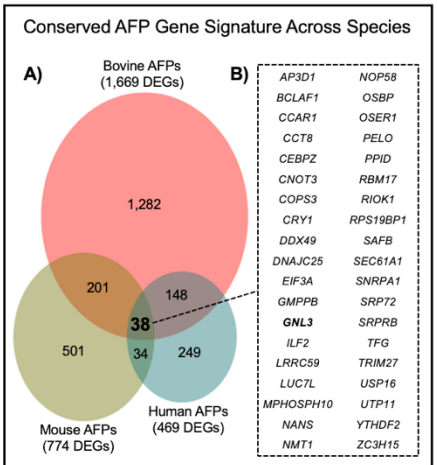

Fig 3: (A) Top transcriptional entropy-scoring AFPs identified across 3 species shared (B) 38 common DEGs, including the canonical stem cell -related marker, GNL3 (nucleostemin).

The Effect of Contact Paradigm and Tissue Composition on the Rolling Versus Silding Behavior in the Knee

Vincent Sise[1], Suzanne Maher[1], Tony Chen[1]
[1]*Hospital for Special Surgery, New York City, NY*

Study Objective: During movement, the knee undergoes rolling and sliding contact of the tibiofemoral joint [1]. Disruption of normal kinematics via injury results in atypical loading patterns and increased stress on the cartilage [2]. Understanding the effect of sliding velocity, applied load, and tissue composition on the kinematic behavior of the knee is critical to understanding wear progression. The objective of this study was to evaluate the rolling versus sliding behavior at different applied loads and velocities in both mature and immature bovine to better understand the effects of contact paradigm and tissue composition on the kinematic profile of the knee.

Methods: Three mature (2-3 years old) and three immature (2-3 months old) bovine knees (abattoir; IACUC exempt; sex unknown) were dissected into medial and lateral condyles (DREMEL oscillating saw). The samples were secured in a custom Sliding Articular Testing System (SACTS) [3] for articulation against a spherical Delrin ball (Ø2.54 cm) on a freely rotating axis that could be set to a (1) fixed axis (FA) configuration to isolate purely sliding articulation, or an (2) unfixed axis (UA) configuration to allow rolling and sliding motion (Figure 1). Articulation along the track length (+/-20 mm) from the apex down the sample and vice versa were defined as the downstroke (DS) and upstroke (US), respectively. The samples were tested for 20 cycles at different speeds (50, 10, 1 mm/s), 3 kg applied load, and with a FA and UA configuration at each velocity. For the immature bovine samples, the tests were subsequently repeated at 1 kg of load. Samples hydrated in gauze for 2× the duration of contact in between tests. After testing, the cartilage was removed and the Delrin ball was run along the bone to measure cartilage thickness. MATLAB was used to calculate mechanical properties for the 3 kg cases with contact area approximated by a modified Hertzian theory of elastic deformation (1 kg case was not calculated due to error in thickness measurement). Change in angular position was converted to a linear distance using the arc length formula ($L=(\theta/360)\,\pi D$) and defined as cumulative distance rolled (CDR) over all 20 cycles (80 mm distance per cycle). Two-way ANOVAs with Tukey post-hoc correction were conducted on the FA and UA cases and between UA cases for tissue types (significance level $p<0.05$).

Results: At 3 kg load, CDR was significantly higher in the unfixed v. fixed axis case for the mature ($p=0.0315$) but not the immature tissue ($p=0.329$). In the second test, with immature bovine loaded at 1 kg, CDR was significantly higher in the unfixed v. fixed axis case ($p<0.0001$), and significantly higher than the immature bovine at 3 kg ($p=0.001$). In all cases, there was no statistically significant effect of sliding velocity on the CDR (Figure 2). Strain was significantly higher, and stress was significantly lower in the unfixed vs fixed axis case for mature ($p=0.0452$, $p=0.0422$) and immature bovine tissue at 3 kg ($p<0.001$, $p=0.0012$). Comparing tissue types in the free rolling condition, significant difference between tissue maturities was found in strain ($p<0.0001$), but no significant difference was found between stress ($p=0.254$) (Figure 3). Average thickness and deformation in mature tissue (0.54±0.17 mm, 1.23±0.22 mm, respectively) and in immature tissue (0.76±0.36 mm, 5.87±1.55 mm, respectively) were statistically different ($p<0.0001$, $p=0.0388$, respectively. Data not shown).

Conclusions: We found that a combination of rolling/sliding decreases the stress profile across both tissue types at 3 kg, indicating obstructed movement (fixed axis prohibiting rolling) results in higher stresses on the cartilage. Additionally, tissue maturity influenced the incidence of rolling behavior, despite mature and immature bovine tissue having similar friction coefficients reported in literature (~0.006) [4, 5]. This factor, paired with the increased rolling in mature tissue, suggests that the incidence of rolling is influenced by the intrinsic mechanical properties of the tissue with increased strain, but not deformation, resulting in higher levels of rolling occurring. The results also indicate that applied load, not velocity, has a statistically significant impact on the rolling behavior in the cartilage. Because both loading across the joint and anterior-posterior translation change with injury [2], this result encourages further investigation into how individual symptomatic factors might alter the joint kinematics.

Significance: Abnormal kinematic movement in the knee results in increased incidence of musculoskeletal injury. Through identification of structure-function relationships between contact paradigms, tissue composition, and resulting kinematic behavior, we can begin to determine what alterations to joint contact predispose to cartilage degeneration.

References: [1] Maderbacher, G, et al. J Arthroplasty 31.9; 2038-2042,2016. [2] Markström, J. et al Knee Surg. Sports Traumatol. Arthrosc:26.2:358-367, 2018. [3] Schätti, O et al., Ann Biomed Eng, 2577-2588, 2016. [4] Shi, L, et Ann. Biomed. Eng. 39.1:132-146, 2011. [5] Petersen, C. A., et al. Osteoarthr. Cartil. 31.12 (2023): 1594-1601. **Acknowledgements**: This study was funded by T32 AR078751.

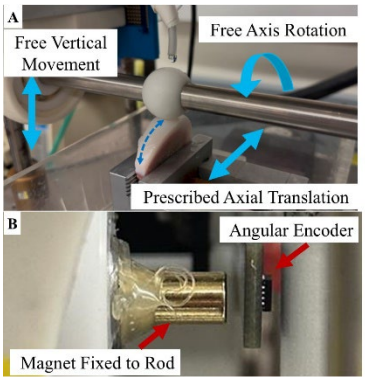

Figure 1: SACTS Device. (A) Delrin ball attached to an axis on ball bearings, (B) Magnetic encoder and magnet fixed to end of the axis.

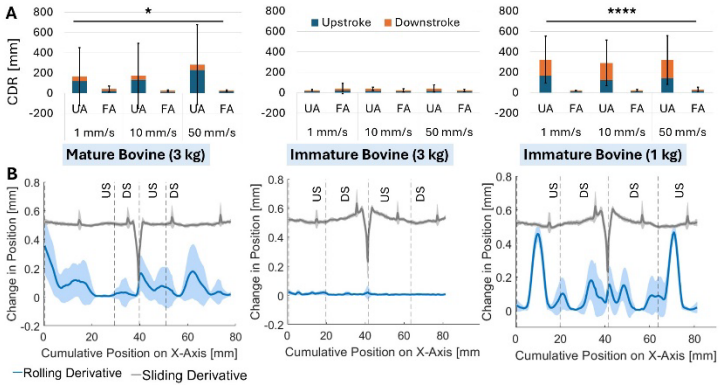

Figure 2: (A) CDR for mature bovine, immature bovine at 3 kg load, and immature bovine at 1 kg load. (*=p<0.05; ****=p<0.0001) (B) Change in position across the sample for rolling (blue) compared to prescribed axial sliding (gray) for mature and immature tissue. Articulation changes direction at x = 40 mm.

Determining the Role of Mechanosensitive PIEZO1 Ion Channel in Directing Skeletal Muscle Fibro-Adipogenic Progenitor Function

Kasoorelope Oguntuyo[1], Charlene Cai[1], Britney Chin-Young[1], Larion Santiago[1], Woojin M. Han[1]

1. *Department of Orthopaedics, Icahn School of Medicine at Mount Sinai*

Introduction: Fatty and fibrotic infiltration into muscle following chronic injury or disease is detrimental to muscle quality, leading to progressive decreased function. Fibro-adipogenic progenitors (FAPs) are the mesenchymal stem cell population that are the source of these degenerative tissues that embed within the muscle.[1] During normal muscle regeneration, these FAPs transiently proliferate to play a supportive role before being cleared.[2] In chronic conditions, FAPs persist and differentiate into adipocytes and/or myofibroblasts.[3] However, the cues that drive this response in FAPs is not well understood. We propose that mechanical cues that change over the course of muscle regeneration, such as the matrix stiffness,[4] contribute to FAPs pathologic function. While it is known that FAPs do respond to changes in matrix stiffness,[5] the underlying mechanism remains unclear. PIEZO1, an ion channel that has been shown to respond to matrix stiffness, stretch, and other mechanical cues,[6,7] that has been identified in cells across the musculoskeletal system, but not yet in FAPs. We hypothesize that PIEZO1 senses the dynamic matrix stiffness and is essential for FAP function during muscle regeneration.

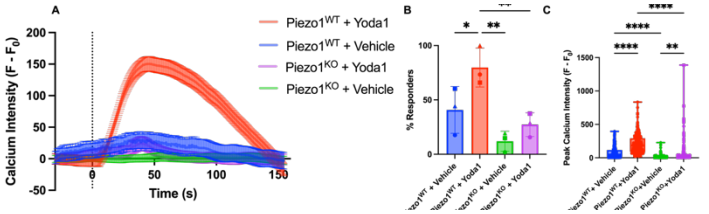

*Figure 1: Calcium Intensity in FAPs with PIEZO1 wild-type or knockout. * p < 0.05, ** p < 0.01, **** p < 0.0001 by one-way ANOVA.*

Brief Statement of Methods: To test our hypothesis, we established a method to knockout PIEZO1 in FAPs *ex vivo* using lipid nanoparticles (LNPs) delivering Cre mRNA (Cre-LNPs). With this system, we evaluated the role of PIEZO1 in FAP cellular morphology and proliferation in response to engineered hydrogels of different stiffness.

Results: Following administration of Yoda1, a PIEZO1 specific agonist, a greater percentage of wild-type FAPs showed increased intracellular calcium signals than those treated with vehicle or Yoda1 in FAPs where PIEZO1 was knocked out by Cre-LNP (**Figure 1**). When cultured on hydrogels, we found that cell area increases as stiffness increases (**Figure 2 A,B**). PIEZO1^{KO} FAPs exhibit decreased cellular area when compared to their wild-type counterparts. When assayed for proliferation with EdU+ pulse, FAPs were found to similarly increase both cellular density and proliferation as stiffness increased (**Figure 2C-D**). However, these effects were lost on the 12 and 35 kPa hydrogels with PIEZO1 knockout.

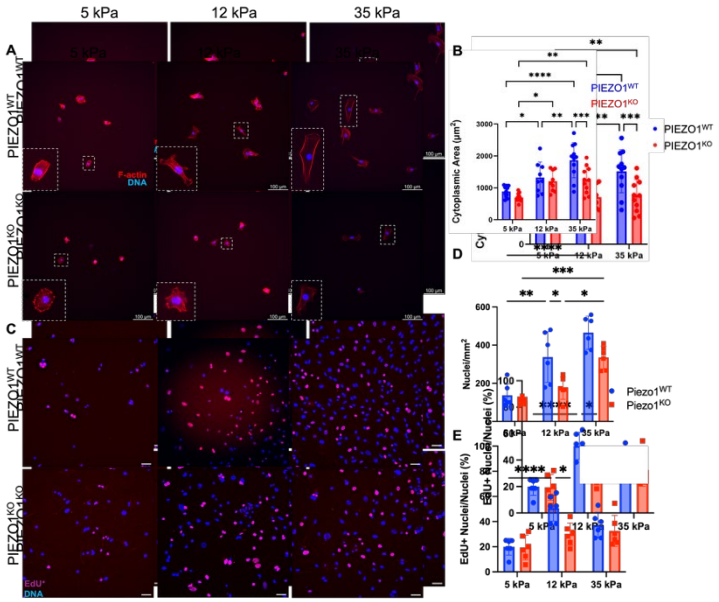

*Figure 2: PIEZO1 Mediates Stiffness Dependent Changes in Cell Area (A,B) and Proliferation (C-E). * p < 0.005, ** p < 0.01, *** p < 0.001, **** p < 0.0001 by two-way ANOVA.*

Conclusions: Our findings show that FAPs express PIEZO1, which can be knocked out *ex vivo* using Cre-LNP delivery. Additionally, PIEZO1KO lessens the stiffness-dependent increase in cell area and proliferation seen when FAPs are seeded on hydrogels, suggesting that PIEZO1 may respond to dynamic stiffness during muscle regeneration may regulate FAPs quantity and prevent their persistence.

Significance: This work identifies PIEZO1 as a potential mechanosensor in FAPs during muscle regeneration that may operate through altering cellular morphology and cytoskeletal elements. By investigating the mechanisms affected by PIEZO1, this work may also identify potential therapeutic targets to prevent degenerative fatty and fibrotic infiltration in diseased states or following chronic muscle injury.

Phenol Red Enhances Tissue Engineered Cartilage for Osteoarthritis Treatment Through Estrogenic Properties

Claire Pinnie[1], Jack Rogot[1], Lianna R. Gangi[1], Clark T. Hung[1,2]
Departments of [1]Biomedical Engineering and [2]Orthopedic Surgery, Columbia University, New York, NY

INTRODUCTION: Osteoarthritis (OA) is a degenerative cartilage disease that causes inflammation, pain, and loss of mobility in the knee joint.[1] OA has been found to disproportionately affect the aging female population due to postmenopausal decreases in estrogen levels.[1] Postmenopausal estrogen supplementation has been shown to decrease symptoms of OA, potentially mediated through estrogen receptors in articular cartilage.[1] Low levels of estrogen in the synovial fluid translates to lower estrogen receptor activation and, as a result, lower articular cartilage metabolism[4]. Currently, total knee arthroplasties (TKA) are the gold-standard for pain relief and restoration of function. Tissue-engineered (TE) osteochondral grafts have emerged as an alternative treatment option to TKA; serving a scaffold for allogeneic cells, they promote native tissue regeneration.[2] Phenol Red, a common pH indictor used in tissue culture media, has been implicated as a weak estrogen analog, causing the activation of estrogen receptors and increased metabolic activity.[5] We hypothesize that the presence of Phenol Red will promote the growth and improvement of mechanical properties of TE cartilage by acting as an estrogen-like growth hormone.

METHODS: Isolation of Cells: Shoulder cartilage was collected from four female canine donors, digested into primary chondrocytes, and pooled into a single population. 6 x 10^7 cells/mL were cast into a custom mold with an equal volume of 4% w/v agarose. Individual constructs were cut from the mold with a biopsy punch to create TE cartilage (⌀4 mm). TE Cartilage Culture: The population of constructs were split into two primary groups: Phenol Red (+Phenol) and Phenol Red-free (–Phenol), and cultured for 28 days in chondrogenic media (Dulbecco's Modified Eagle's Medium supplemented with 100 nM Dexamethasone, 100 µg/mL Sodium Pyruvate, 50 µg/mL L-proline, 50 µg/mL Vitamin C, 10 ng/mL Transforming Growth Factor β-3, and 1% ITS premix).[3] The TE constructs were grown for 28 days in media ± Phenol Red until their Young's Modulus (E_Y) reached ~100 kPa. Mechanical Testing: Representative constructs were sacrificed every two weeks to monitor growth. E_Y were assessed using custom-built compression testers. At the termination of the 36-day study, the constructs were sacrificed, and dry weights were taken prior to downstream analysis. Cell/Viability Analysis: Live/dead staining was performed using 2 µM Calcein AM and 4 µM Ethidium Homodimer-1. Cell number was calculated using a Pico Green dsDNA Assay. Biochemical Analyses: Collagen (COL) and glycosaminoglycan (GAG) assays were performed at days 14, 28, and 36 to quantify the growth of the constructs. Only endpoint values are herein reported. Statistics: Data reported as mean ± SD and were analyzed via one-way ANOVA with Tukey HSD post-hoc test at α = 0.05.

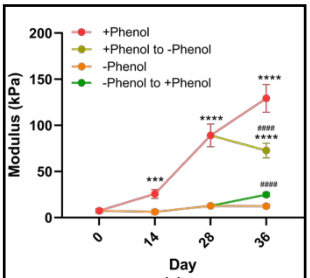

Figure 1. Equilibrium modulus plot of constructs grown in CM ±phenol. ***p<0.001, ****p<0.0001 compared to -phenol, ####p<0.0001 compared to

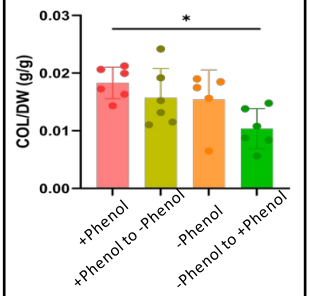

Figure 2. Day 36 plot of collagen concentration normalized to dry weight. *p < 0.05.

RESULTS: Viability Staining: There was no notable increases in cell death in constructs following culture in +/- Phenol Red media. Mechanical Testing: +Phenol constructs demonstrated a greater E_Y at days 14, 28, and 36 compared to -Phenol constructs (Fig. 1, $p < 0.001$). When Phenol Red was removed from the chondrogenic media, a significant decrease in E_Y was observed ($p < 0.0001$). When Phenol Red was added to constructs cultured without it, the E_Y was rescued although not to the level of Phenol Red-only culture ($p < 0.0001$). Biochemical Assays: A trend of a greater collagen concentration in +Phenol constructs compared to -Phenol constructs was observed at each time point (Fig. 2).

DISCUSSION: Steadily increasing E_Y in +Phenol constructs indicated growth and greater structural integrity of those cultured in Phenol Red media compared to those cultured without Phenol Red. Constructs that were cultured in Phenol Red demonstrated significantly greater cellularity, collagen, and GAG compared to constructs cultured without Phenol Red. For the conditions of the current study using engineered cartilage derived from female canine chondrocytes, our results suggest that Phenol Red, a common culture media constituent, is essential for enhancing tissue mechanical and biochemical properties through estrogen receptor activation and increased metabolic activity. It remains to be determined if Phenol Red has the same effect on male canine-derived engineered cartilage.

REFERENCES: 1. Hame+ Curr Rev Musculoskelet Med 2013. 2. Nukavarapu+ Biotechnology Advances 2013. 3. Silverstein+ J. Ortho. Res. 2017. 4. Roman-Blas+ Arthritis Res. Ther. 2009. 5. Berthois+ Proc Natl Acad Sci USA 1986.

Parametric Finite Element Analysis of Protective Padding for Pediatric Commotio Cordis Mitigation

Ciara Woellhof[1], Jeun-Fai Lam[1], Alex Mousazadeh[1], Christian Acuna[1], Todd Griffin[2], Chaudry R. Hassan[1], Yi-Xian Qin[1*]

[1] Department of Biomedical Engineering, Stony Brook University [2] Department of Obstetrics & Gynecology, Stony Brook Medicine

Introduction: Commotio Cordis occurs when a projectile strikes the sternum over the heart during the T-wave upstroke of ventricular repolarization, subsequently leading to sternum deformation, cardiac arrest, and eventual death. Instances of commotio cordis are fatal with a survival rate of 60% only when immediate resuscitation is possible [1]. When not possible, survival rate can drop to as low as 3% [2]. High risk individuals include athletes aged between 8 to 18 who play sports with fast-moving projectiles, such as baseball, hockey, and lacrosse. 47% of Commotio Cordis cases happen during participation in such activities [2]. Chest protectors currently on the market provide inadequate protection against chest injury and Commotio Cordis. One study reported that one third of Commotio Cordis cases have occurred despite chest protection being present [3]. Commercial chest protectors are made from materials which fail to protect the sternum from fatal deformations. This establishes a need for a novel chest protector which incorporates both material choice and design to effectively absorb and distribute impacts from a fast-moving projectile. Using finite element analysis (FEA), this study aims to develop a new chest protector for the adolescent athletes using a layered composite padding for optimized mechanical protection of the body, which will minimize strain and stress in the sternum region, thus reducing Commotio Cordis risk. **Materials and Methods:** FEA software was used to simulate a baseball impact onto the left side of the thorax, with a protective padding present. A nonlinear FEA of thorax was developed using the geometry from CT scans of an adolescent. ABAQUS (Dassault Systèmes, RI, USA) was used to create the baseball, padding, and simplified baseball bat FEMs and incorporated with the thorax. 7,440 hexahedral elements of type C3D8R were used. The following equation was used to determine the elastic modulus of the cortical bones of a 10 year old's ribs [4]: $E(age) = -0.0029316 \cdot (age)^2 + 0.28851 \cdot (age) + 8.3468$ = 8.47 Gpa. The control case for the impact forces was simulated by moving the baseball at 45 mph and hitting the thorax over the heart . A padding was then added in front of the thorax and the baseball impact was analyzed. 4 different materials were analyzed for the chest padding: (i) EVA foam, (ii) soft foam, (iii) hyperfoam, and (iv) expanded polypropylene crushable foam. Additionally, these materials were combined to form 2 types of composites: (a) hyperfoam and EVA foam, and (b) hyperfoam and polypropylene foam. Stress and deformation values were predicted for each material 73 mili-seconds after the ball was launched at the padding. **Results:** The FEA simulation predicted that a composite of polypropylene crushable foam and hyperfoam allowed for the least amount of deformation of the ribs(maximum deformation = 5.55 µm). This composite also showed the lowest stress value on the ribs, with a maximum of 0.753 MPa and lowest strain value of 74 µε. Along with the composite material, polypropylene crushable foam alone also provided good protective chest padding with the maximum deformation of the ribs predicted as 2.77 mm, the maximum stress as 2.55 MPa, and the maximum strain as 530µε, respectively. Soft foam was predicted to provide the worst protection with a maximum deformation predicted as 7.2mm , along with a maximum stress and strain of 64.8 MPa and 7.3 mε, respectively. **Discussion:** This study used a numerical FEA approach to identify the types of foam that were most effective in preventing rib deformation under a high velocity small projectile impact which can lead to Commotio Cordis. The results help to understand how to create more effective chest protection devices for adolescents. One study identified that pressure distribution on impact is an essential factor to preventing severe injury [5]. Although Polypropylene has been cited to have material properties consistent with good pressure distribution [6,7], our discovery of a composite material showing improved protective capabilities can better inform the creation of future chest protectors. In future studies, FEA will simulate Commotio Cordis with additional material and geometric complexities, including the soft tissues (cartilage), non-linear shape, and the microstructure of the padding material to quantify the dispersion of absorbed energy from high velocity impacts.

Conclusion: It is found that polypropylene crushable foam, in layered combination with hyperfoam, can increase impact resistance, decrease stress, strain, and impact energy to create an effective and lightweight chest padding. In future studies, this information can be used on more complex FEA models to determine the best chest protection for adolescent athletes.

Surgical Treatment of Early-Onset Blount Disease: Who is Left in Varus?

Zachariah Samuel, Ofir Horovitz, Mohamed Said, Edina Gjonbalaj, Leila Alvandi, Melinda Sharkey

Introduction: Mid-to-long-term outcomes of patients surgically treated for early-onset Blount Disease remain poorly understood. This study aims to identify preoperative radiographic and patient characteristics, as well as surgical interventions, that predict persistent or recurrent varus deformity at mid-term follow-up.

Methods: In this IRB-approved retrospective study, demographic, clinical, and radiographic data were collected for patients presenting to a single academic institution who underwent surgery for early-onset Blount Disease between 2008 and 2024. Patients were classified into two groups: those with persistent varus alignment and those with neutral or valgus alignment at most recent follow-up. Varus alignment was defined as a mechanical axis deviation (MAD) in zones 2 or 3 and valgus/neutral alignment was defined by MAD in zones 1, -1, -2 or -3. Chi-square and Fisher's exact tests were used to compare groups.

Results: Of 39 limbs, 13 had persistent varus alignment, while 26 achieved valgus/neutral alignment at most recent follow-up. Groups had similar ages at presentation (4.56 vs 4.71; p=0.861) and follow-up (7.08 vs 5.52 years; p=0.167). The varus group more frequently underwent osteotomy with acute or gradual deformity correction (38.5% vs 11.5%) and less often underwent guided growth (38.5% vs 84.6%). Patients with varus had higher Drennan angles at presentation (28.32 vs 21.10), but similar presenting MAD and Langenskiöld stage. Only 1 of 13 patients in the varus group was surgically overcorrected to MAD -1/-2/-3 while 92.3% (12/13) were under-corrected to MAD 1/2/3. In the neutral/valgus group, 46.2% (12/26) of patients were surgically under-corrected to MAD 1/2/3 and 53.8% (14/26) were overcorrected to MAD –1/-2/-3.

Conclusion: Patients with persistent varus were more likely to have undergone osteotomy rather than guided growth, presented with greater initial deformity, and were surgically under-corrected. Interestingly, nearly half of patients in the neutral/valgus alignment group were surgically under-corrected but still achieved neutral or valgus alignment with continued growth at most recent mid-term follow-up.

Significance: A substantial proportion of patients (47%) with early onset Blount disease had their varus deformities surgically under-corrected but nonetheless reached neutral/valgus alignment at most recent follow-up. However, 90% of patients with persistent or progressive varus deformities were under-corrected. Persistent varus was strongly associated with surgical under-correction, supporting intentional overcorrection of the MAD to at least valgus zone –1 when performing guided growth or osteotomy for early-onset Blount disease.

Synovium-Cartilage Crosstalk in Facet Joint Osteoarthritis and Correlations with Adjacent Disc Degeneration

Janai Augustin[1], Kevin Burt[1,2], Matthew Fainor[1,2], Brianna S. Orozco[1,2], Sung Yeon Kim[1], Carla R. Scanzello[1,2], Sarah E. Gullbrand[1,2]

[1]Department of Orthopaedic Surgery, Perelman School of Medicine, University of Pennsylvania, Philadelphia, PA;
[2]Translational Musculoskeletal Research Center, Philadelphia Veterans Affairs Medical Center, Philadelphia, PA.

INTRODUCTION: Low back pain affects up to 85% of individuals and is the leading cause of disability worldwide, often stemming from degeneration of the spinal motion segment[1]. The facet joints (FJs) are synovial articulations posterior to the intervertebral disc (IVD) that play a critical role in load transmission and constrain range of motion in the spine[2]These joints gradually degenerate through cartilage erosion, subchondral sclerosis, and synovial remodeling, with inflammatory and biochemical changes activating nociceptive pathways and driving chronic pain[3]. This pathology is called facet joint osteoarthritis (FOA) and contributes to back pain in 15-41%[4] of patients. In other synovial joints such as the knee and hip, synovitis is tightly linked to symptoms and structural progression of osteoarthritis (OA)[5], yet the contribution of the synovium to osteoarthritic changes in the facet joint and degeneration of the adjacent intervertebral disc remains poorly understood. We hypothesized that FJ synovium pathology initiates and drives inflammatory and catabolic changes in FOA and severity of FOA correlates with adjacent IVD degeneration.

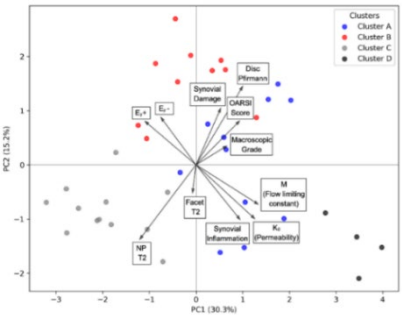

Fig 2: PCA biplot showing relationships between FJ cartilage properties, IVD structure, and FJ synovial pathology. Arrows in the same direction = direct correlation, arrows in opposite directions = inverse correlation, arrows at 90 degrees = no correlation.

METHODS: *Cadaveric spine acquisition:* Five lumbar spines (2 male, 3 female, 27-70yo), were obtained from human cadavers. *IVD qMRI:* To assess disc degeneration, 3T MRI with sagittal T2 mapping were obtained for disc Pfirmann grading[6], and to quantify nucleus pulposus (NP) T2 relaxation times[7]. Spinal motions segments (n = 22) were dissected into discs and facet joints. *Facet cartilage creep indentation:* The articular surface was indented using a 2 mm spherical indenter (0.1 N creep, 15 minutes)[8]. *Facet qMRI and histopathology*: Following mechanical testing, T2 mapping of the facet articular cartilage was performed on a 4.7T preclinical MRI scanner. Evaluation of cartilage damage[9], and synovial inflammation and damage [10] was performed on paraffin embedded axial sections of intact facets. *Imaging mass cytometry (IMC)*: Axial sections underwent heat-mediated antigen retrieval and overnight incubation with a basic immune cell panel, a myeloid cell panel, and a tissue architecture panel of metal-conjugated antibodies, followed by imaging using a Hyperion Imaging System. *Statistical analysis:* Differences in quantitative outcomes stratified by OARSI score were assessed via a student's t-test ($p<0.05$). Principal component analysis (PCA) biplots were generated in Python.

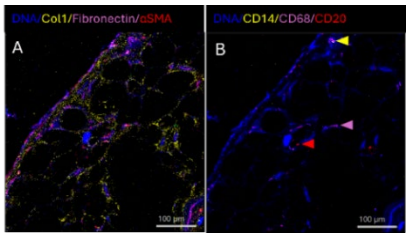

Fig 3: IMC of Facet Joint Synovium. A) tissue architectural markers in FJ synovium, **B)** Immune cell markers in FJ synovium.

RESULTS: Facet cartilage mechanical testing demonstrated that increased OARSI scores were accompanied by increased cartilage permeability and reduced tensile and compressive moduli. PCA biplots (**Fig 1**) demonstrated that more degenerative facet cartilage (higher OARSI scores and macroscopic grades) and higher synovial damage scores were associated with reduced IVD NP T2 values indicating more extensive disc degeneration. Synovial inflammation was not correlated with synovial damage but was inversely correlated with facet cartilage mechanical properties. PCA analysis revealed distinct phenotypes: healthy, hydrated IVDs with little facet pathology (cluster C); concomitant disc degeneration and facet synovium damage (cluster B); facet synovial inflammation with minimal disc and facet degeneration (cluster A), and severely degenerated discs and facets marked by high synovial inflammation, and compromised cartilage mechanics (cluster D). IMC demonstrated strong expression of collagen I, fibronectin, αSMA, and VEGF, as well as abundant immune and myeloid lineage cells within the facet synovium **(Fig 2**).

DISCUSSION: Our data revealed distinct phenotypes of spinal disease, with synovial damage and inflammation driving disparate phenotypes of degeneration, consistent with knee OA[10]. The presence of elevated synovial inflammation in samples with only modest structural damage suggests that synovial inflammatory signaling may contribute to subsequent tissue breakdown. These findings parallel knee OA where inflammatory cells can drive articular extracellular matrix degradation, pain and progression of disease[5]. The negative correlation between NP T2, synovial damage and cartilage degeneration provides evidence for facet–disc crosstalk, however, the biological mechanisms driving this relationship remain unclear and warrant further investigation. IMC further revealed ECM remodeling proteins (collagen I, fibronectin), myofibroblast activation (αSMA), angiogenic factors (VEGF), and immune cell infiltration, features consistent with synovial remodeling in knee OA[5]. Ongoing IMC analyses will quantify changes in tissue architecture and synovial cell populations as FOA progresses and will be compared to healthy facets to define molecular and cellular signatures of disease.

SIGNIFICANCE: Together, these results highlight the contribution of synovial inflammation and damage to FOA progression and adjacent disc degeneration, positioning the synovium as both a driver of pathological changes and a potential therapeutic target for low back pain.

REFERENCES: [1] Shahidi + J Orthop Res., 2017, [2] Jaumard + J Biomech Eng., 2011, [3] Gelhorne + Nat Rev Rheumatol., 2013, [4] Du + J Pain Res., 2022, [5] Scanzello + Bone., 2012, [6] Pfirrmann + Spine (Phila Pa 1976)., 2001, [7] Martin + J Orthop Res., 2015 [8] Gupta + J Orthop Res., 2023 [9] Pritzker + Osteoarthritis Cartilage., 2006 [10] Philpott + Osteoarthritis Cartilage., 2024.

MRI PREDICTORS OF OSTEOCHONDRAL INJURY IN ADOLESCENTS WITH PATELLAR DISLOCATION: ROLE OF TROCHLEAR DYSPLASIA AND RECURRENT INSTABILITY

Authors: Faizan Khalid BS, Jason D. Brenner BS, Steven M. Henick MD, Leila Mehraban Alvandi PhD, Eric D. Fornari MD, Benjamin J. Levy MD, Mauricio Drummond Junior MD

Affiliations: Montefiore Health System, Albert Einstein College of Medicine

Background: Osteochondral injury (OCI) is a known sequela of patellar dislocation (PD), particularly in adolescent patients.[1] Prior studies have identified patella alta and trochlear dysplasia (TD) as potential risk factors for OCI.[2,3] However, the contribution of anatomic and clinical risk factors to OCI development in this population remains unclear. This study aimed to address this gap by identifying clinical and imaging predictors of PD.

Hypothesis/Purpose: The authors hypothesized that patients with PD and OCI would have more prior patellar dislocations, and a higher prevalence of TD and patella alta compared to patients with PD without OCI.

Methods: A retrospective review was conducted of patients with MRI-confirmed PD at a single institution. Patients were stratified into two cohorts based on the presence or absence of OCI. Variables collected included age, gender, number of prior patellar dislocations, four axial measurements of cartilaginous sulcus angle (cSA – most proximal, cSA2 –near proximal, cSA3 – near distal, cSA4 – most distal), Caton Deschamps (CD), tibial tubercle–trochlear groove (TT-TG) distance, and patellar tilt (PT). Lesion location and cartilage thickness were also recorded for patients with OCI. Independent t-tests were used to compare continuous variables, and Chi squared tests were used for categorical variables. Statistical significance was defined as $p<0.05$.

Results: A total of 170 participants were included; 71 (57.7% female) had a history of OCI (mean age 14.54 ± 2.53 years), and 99 (60.6% female) had no history of OCI (mean age 15.13 ± 2.20 years). There was no difference in age (p=0.12) or sex distribution (p=0.83) between the cohorts. Patients with OCI were associated with elevated sulcus angles at multiple axial levels: cSA2 (p=0.023), cSA3 (p=0.015), and cSA4 (p=0.001). However, there was no difference in cSA1 (p=0.090), CD (p=0.321), TT-TG (p=0.188), or PT (p=0.426) between cohorts. Patients with OCI (2.69±3.20) had a greater number (p=0.035) of PDs compared to those without OCI (1.89±1.55). Of the 71 patients with OCI, 17 had injuries to the distal femur, 52 from the patella, and 2 from both the patella and femur; 21 of the OCIs were full thickness.

Conclusion:
OCI in patients with PD were significantly associated with a greater number of prior PDs and TD, measured by the cSA. Most lesions were located on the patella, and approximately one-third were full-thickness. These findings support MRI surveillance in patients with frequent dislocations to assess for clinically significant OCI.[4]

References

1. Khan SA, Baghdadi S, Carey JL, Moores TS, Sheth NP, Ganley T. Osteochondral fractures after patellar dislocation: current concepts. *JAAOS Glob Res Rev.* 2021;5(12):e21.00155. doi:10.5435/JAAOSGlobal-D-21-00155

2. Dejour DH, Mazy D, Pineda T, Cance N, Dan MJ, Giovannetti de Sanctis E. Patellar instability: current approach. *EFORT Open Rev.* 2025;10(6):378-387. doi:10.1530/EOR-2025-0051

3. Maine S, Ngo-Nguyen C, Barzan M, Stockton C, Modenese L, Lloyd D. Bisect offset ratio and cartilaginous sulcus angle are good combined predictors of recurrent patellar dislocation in children and adolescents. *J ISAKOS.* 2021;6(2). doi:10.1136/jisakos-2020-000461

4. von Engelhardt LV, Raddatz M, Bouillon B, Degenhardt K, Ziskoven C. How reliable is MRI in diagnosing cartilaginous lesions in patients with first and recurrent lateral patellar dislocations? *BMC Musculoskelet Disord.* 2010;11:149. doi:10.1186/1471-2474-11-149

Response of articular cartilage to bipedal loading

Christopher J. O'Connor-Coates[1], David E. Komatsu[2], Christopher J. Percival[1]

[1]Stony Brook University Department of Anthropology, Stony Brook, NY, [2]Stony Brook University Department of Orthopaedics and Rehabilitation, Stony Brook, NY

INTRODUCTION: Following chondral modeling theory (CMT), the fact that humans display thicker femoral articular cartilage than quadrupedal primate relatives may be the direct result of growth responses triggered by higher loading magnitudes experienced during bipedalism. Increased growth in articular cartilage may be an effective way to enhance cartilage health in response to regular activity and has been demonstrated to occur in exercised animal models, and CMT predicts that increased cartilage growth will result in increased articular cartilage thickness and increased chondrocyte cell densities. However, studies exploring the relationship between cartilage growth and mechanical loading have found conflicting results, with some indicating an increase in thickness and cellular density, and others finding an increase in thickness but not in cellular density, and still others finding no response. Therefore, to evaluate if articular cartilage thickness and cellular density can be increased by plastic developmental responses to higher loads from an introduction to bipedalism, we compared the tissue morphology of rats that exercised bipedally to quadrupedally exercised, bipedal standing, and control groups.

METHODS: We collected sagittal sections from the right lateral femoral condyles of 20 female Lewis rats, divided into four groups (5 rats per group): walking bipeds (WB), exercised quadrupeds (Q), standing bipeds (SB), and controls (C). The study began when the rats were approximately 6 weeks old and continued for 8 weeks. WB and Q rats exercised on a custom treadmill for 1 hour per day, 5 days per week, at a speed of 0.13 m/s. SB rats were placed on the treadmill under the same conditions, but the treadmill remained stationary. C rats stayed in their cages throughout the experiment and did not undergo any exercise regimen. The sections were stained using Hematoxylin and Eosin and analyzed for cartilage thickness in 3 regions of the condyle, and for chondrocyte density in 5 regions of the condyle. Cartilage thicknesses were measured for 4 specimens (2 WB, 2 C) as the linear distances between the osteochondral junction and the superficial-most surface of the articular cartilage at the anterior, middle, and posterior aspects of the femoral condyle. Cell densities were measured using a custom Fiji macro to automatically count the cell nuclei in each region of interest (ROI). These densities were averaged for each specimen and groups were compared using a Wilcoxen rank-sum test in R.

RESULTS: Thickness measurements were higher in WB compared to C across all regions measured: anterior (16.99µm ± 1.51 vs. 15.42µm ± 3.50), middle (17.58µm ± 1.84 vs. 12.84µm ± 1.34), and posterior (19.04µm ± 2.16 vs. 12.81µm ± 0.813). Our results reveal that between the walking bipeds and the controls, there is an average increase of ~1.5µm in the anterior aspect of the condyle, ~4.7µm in the middle aspect of the condyle, and ~6.2µm in the posterior aspect of the condyle. Average cell densities (mean ± SD) were WB: ~0.0028/μm^2 ± 0.0004, C: ~0.0027/μm^2 ± 0.0006, SB: ~0.0030/μm^2 ± 0.0005, and Q: ~0.0030/μm^2 ± 0.0002, with no significant intergroup differences identified.

CONCLUSION: Although the sample size for cartilage thickness is currently not large enough for statistical analysis, our results suggest that developmental plasticity may contribute to producing thicker articular cartilage in the human knee. However, we did not find a difference in cellular density between our groups. Further work is planned to validate this result.

Funding Source: This work was supported by start-up funds from Stony Brook University to CJP.

The Multi-Level Axial Patellofemoral Score (MAPS-TD) to Stratify Trochlea Dysplasia Severity

Jason Brenner, BS[1], Steven M. Henick, MD[2], Leila Alvandi, PhD[1,2], Edina Gjonbalaj[2], Jacob Schulz, MD[1,2], Eric Fornari, MD[1,2], Yungtai Lo, PhD[1,2] Benjamin J Levy, MD[1,2], Mauricio Drummond, MD[1,2]

[1]Albert Einstein College of Medicine, The Bronx, NY
[2]Department of Orthopaedic Surgery, Montefiore Einstein, The Bronx, NY

Background: Trochlear dysplasia (TD) is an important risk factor for patellar dislocation (PD). While several MRI measurements have been described to assess TD, stratifying its severity is less understood. Most techniques for assessing TD utilize radiographs, three-dimensional CT, or one axial MRI level, such as the Dejour classification adapted to MRI. However, there is no consensus on optimal axial level. Therefore, evaluating multiple axial levels of the trochlear groove (TG) may allow for complete assessment. The objective of the present study was to introduce a method that allows for stratification of TD severity using sulcus angle (SA) measurements at four axial levels. We hypothesize that patients with Recurrent patellar dislocations (RPDs) will have a higher prevalence of more severe grades of TD and a lower prevalence of no TD compared with controls.

Methods: Pediatric patients were retrospectively categorized into two cohorts: RPDs and controls (patients with no history of patellar dislocation; PD). Cartilaginous SA measurements were completed at four consecutive MRI axial levels (SA1=most proximal, SA2=near-proximal, SA3=near-distal, and SA4=most distal). Cutoff values were identified using Youden's index. Patients were classified based on the number of elevated SA values: all four elevated values indicated Grade 4 TD; three elevated values indicated Grade 3 TD; two elevated values indicated Grade 2 TD; one elevated value indicated Grade 1 TD; and all normal values indicated Grade 0 TD. Proportions were calculated, and Fisher's exact tests were used to compare TD severity between RPDs and controls.

Results: 106 RPDs and 98 controls were included. Diagnostic cutoff values were: SA1 160°, SA2 154°, SA3 153°, and SA4 148°. The RPDs were more likely to have Grade 4 TD (58% versus 4%, p<0.001) and Grade 3 TD (13% versus 4%, p=0.03) compared with controls. Conversely, RPDs had less Grade 0 TD (8% versus 68%, p<0.001). There was no difference in the proportions with Grade 2 TD (13% versus 9%, p=0.39) or Grade 1 TD (8% versus 14%, p=0.27) between cohorts.

Conclusion: The Multi-level Axial Patellofemoral Score for Trochlear Dysplasia (MAPS) is a novel classification system which stratifies TD severity and has demonstrated accuracy and reliability in distinguishing RPDs from controls. Its primary clinical utility lies in differentiating more extensive TD (especially Grade 4) from mild TD (Grades 1 and 2). MAPS-TD may help guide surgical decision-making, possibly even in identifying candidates for surgical procedures to address TD (i.e. trochleoplasty) among those with Grade 4 TD.

	RPDs (n=106)	Controls (n=98)	Odds Ratio	p-value
Grade 4	61(58%)	4(4%)	**31.86(10.90 – 93.07)**	**<0.001**
Grade 3	14(13%)	4(4%)	**3.58(1.13 – 11.27)**	**0.03**
Grade 2	14(13%)	9(9%)	1.50(0.62 – 3.65)	0.39
Grade 1	9(8%)	14(14%)	0.56(0.23 – 1.35)	0.27
Grade 0	8(8%)	67(68%)	**0.038(0.016 – 0.087)**	**<0.001**

Table: The Multi-Level Axial Patellofemoral Score for Trochlear Dysplasia (MAPS): proportion of RPDs versus controls with Grade 4, Grade 3, Grade 2, Grade 1, and Grade 0 TD. RPD, recurrent patellar dislocator; TD, trochlear dysplasia.

References:

Dejour DH, de Sanctis EG, Müller JH, et al. Adapting the Dejour classification of trochlear dysplasia from qualitative radiograph- and CT-based assessments to quantitative MRI-based measurements. Knee Surg Sports Traumatol Arthrosc. Nov 18 2024;doi:10.1002/ksa.12539

Levy BJ, Tanaka MJ, Fulkerson JP. Current Concepts Regarding Patellofemoral Trochlear Dysplasia. Am J Sports Med. May 2021;49(6):1642-1650. doi:10.1177/0363546520958423

Comparison of transport properties between human and tissue-engineered vertebral endplates

Brianna S. Orozco[1,2], Alexandra J. Baranyai[1], Matthew Fainor[1,2], Mohamed Habib[3], Aaron J. Fields[3], Sarah E. Gullbrand[1,2]
[1]University of Pennsylvania, Philadelphia, PA, [2]Corporal Michael J. Crescenz VA Medical Center, Philadelphia, PA,
[3]Department of Orthopaedic Surgery, University of California, San Francisco, CA, USA

INTRODUCTION: The vertebral endplates are the primary routes through which nutrients and metabolites enter and exit the intervertebral disc.[1] Changes in cartilaginous endplate (CEP) composition, including CEP fibrosis and calcification, can impair nutrient and metabolite transport[2,3] and associate with more severe disc degeneration.[4,5] As an alternative to spinal fusion surgery for the treatment of end-stage disc degeneration, our group developed a composite tissue-engineered total disc replacement (eDAPS), which includes a porous poly(caprolactone) (PCL) scaffold as an endplate analog that provides interface between the native vertebral bone and engineered disc. Our prior work has been focused on biomaterial modifications to this scaffold to promote integration *in vivo*; however, the transport properties of these engineered endplates in comparison to human endplates remains unknown.[6] Recapitulating the transport properties of healthy endplates will be essential to the long-term *in vivo* success of the eDAPS. We hypothesized that transport across engineered endplates would decrease with extracellular matrix deposition within the scaffold to reach equivalence with transport across healthy endplates.

METHODS: *Engineered endplate fabrication:* PCL endplate scaffolds (10 mm diameter x 1.5 mm in height) were fabricated according to a salt-leaching protocol and coated with hydroxyapatite (HA).[6,7] HA-coated PCL scaffolds (n=6) were then seeded with goat mesenchymal cells and cultured in chemically defined media with TGF-β3 for 5 and 10 weeks. *Human endplate acquisition:* Eight lumbar spines (L12-L5S1, 5 male, 3 female, 25-70yo) were obtained from human cadavers, and subjected to MRI scans to determine disc health. From spinal motion segments (n=35), two cylindrical cores (10 mm diameter x 2.50 mm, n=66) were obtained that included the cartilage endplate and adjacent trabecular bone. *Passive diffusion experiments*: Human endplates (n=32), acellular HA PCL scaffold (n=6), and 5-week cell-seeded HA PCL scaffolds (n=4) were used for passive diffusion experiments, where the upstream chamber contained either 3.33 mg/mL of glucose (MW=180.16), or 1.1 mg/mL of sodium fluorescein (MW=367.27). Triplicates of the downstream chamber were collected every hour for 6 hours. Fluorescence and absorbance were read via a microplate reader to calculate downstream chamber solute concentration. Total diffusion was quantified by calculating the area under the curve (AUC). *Convection experiments*: A custom loading apparatus (**Figure 1A**) was used apply cyclic pressure (0.28–0.55 MPa, 0.5 Hz) to native and engineered CEPs. Outcomes included the net fluorescein transport and hydraulic permeability.[2]

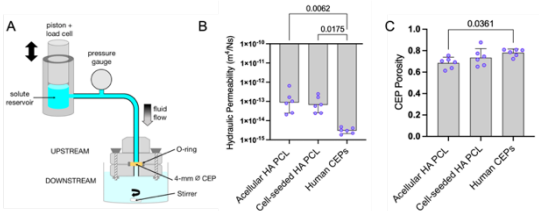

Figure 1. (A) Schematic of custom loading apparatus. (B) Hydraulic Permeability and (C) CEP Porosity for each experimental group.

RESULTS: Passive diffusion experiments demonstrated that transport through tissue-engineered CEPs was variable but trended lower compared to native human CEPs. Cell-seeded HA PCL had significantly less glucose passive diffusion compared to endplates from degenerative discs, but not statistically different from endplates adjacent to healthy discs (**Figure 2B**). Sodium fluorescein passive diffusion was not statistically different across groups, but demonstrated that sodium fluorescein diffusion is variable within the 5-week cell-seeded HA PCL and that passive diffusion across cell-seeded HA PCL endplates trended higher than for acellular HA PCL (**Figure 2C**). Acellular HA PCL and 10-week cell-seeded HA PCL had significantly higher hydraulic permeability compared to native human CEPs (**Figure 1B**). For CEP porosity, acellular HA PCL had significantly lower porosity compared to native human CEPs (**Figure 1C**).

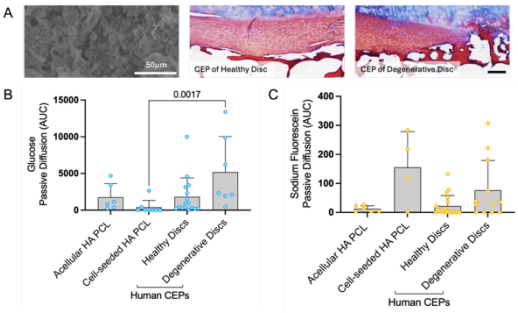

Figure 2. (A) SEM image of HA PCL scaffold and CEP histology images (Mallory Heidenhain). (B) Glucose and (C) Sodium Fluorescein passive diffusion for experimental groups. Endplate scale = 555 μm.

DISCUSSION: Passive diffusion experiments demonstrated trending reductions in glucose diffusion and increases in sodium fluorescein diffusion following chondrogenic pre-culture of MSC seeded endplates, likely due to the deposition of proteoglycan and collagen matrix. Endplates adjacent to degenerative discs also exhibited trending increases in diffusion compared to endplates adjacent to healthy discs. Diffusion across engineered endplates was more similar to diffusion across endplates adjacent to healthy discs versus degenerative discs. The low hydraulic permeability of healthy human CEPs is consistent with the dense, negatively charged extracellular matrix, which resists fluid flow. Engineered CEPs had less resistance to fluid flow compared to native human CEPs, which may lead to greater convective transport. This may improve nutrient transport into tissue-engineered total disc replacements, but may come at the expense of increased creep deformation under physiologic loading. CEP porosity is an important factor that influences hydraulic permeability and solute transport [2]. Despite engineered CEPs having higher permeability, they have low porosity, indicating other factors, such as matrix maturity and cross-linking/fiber anisotropy, may affect permeability.

SIGNIFICANCE: Overall, the results from this study can inform design improvements to the endplate interface of composite, tissue engineered disc replacements to enhance their long-term in vivo performance.

REFERENCES: [1] Maroudas+ *J. Anat.*, 1975 [2] Sampson+ *J. of Biomechanics*, 2018 [3] Benneker+ *Spine*, 1976 [4] Antoniou+ Spine 1996 [5] Bonnheim+ Eur Spine J 2022 [6] Fainor+ *Cells Tissues Organs*, 2023 [7] Kim+ *Acta Biomater, 2020*

Lumbar Intervertebral Disc Injury Induces Pain-Like Behaviors And Disability In A Mouse Discogenic Pain Model

Neharika Bhadouria[1*], Yunsoo Lee[1], Kaljang Sherpa[1], Michelle Villagran[1], Amanda Kopelman[1], Xueming Hu[1], Xinqi Guo[1], Trevonn Gyles[1], Andrew C. Hecht[1], Hongzhen Hu[1], James C. Iatridis[1]

[1]Department of Orthopedics, Icahn School of Medicine at Mount Sinai, New York, NY

INTRODUCTION: Back pain is a leading cause of global disability and is strongly associated with intervertebral disc (IVD) degeneration (IVDD). Chronic back pain causes reduced mobility, sagittal imbalance, and anxiety-like behaviors, with no disease modifying treatments available. Mouse models of discogenic pain are needed because genetic modification can identify pain and degeneration mechanisms, because pain-like behavioral assays exist, and because it is a small vertebrate animal model **[1,2]**. However, the small size of mice has resulted in most mouse models of IVDD using mouse coccygeal IVDs which have similar anatomy and a simplified surgical approach, yet coccygeal IVDs differ in their proximity to neural structures and biomechanical loading compared to lumbar IVDs. Few lumbar mouse IVDD models exist and there is a need for repeatable, surgically induced mouse lumbar IVDD models and this study focuses on deep phenotyping of pain-like behaviors. The aims are to develop an annulus fibrosus puncture-injury induced IVDD model in lumbar spine in female and male mice and to characterize multiple pain-like behaviors (hindpaw mechanical von Frey, axial grip strength, open-field response, and gait abnormality).

METHODS: C57BL/6J mice (n=3-4/group) received Sham, Mild (single puncture), or Severe (three punctures) lumbar IVD injury (L4-S1)(Fig.1A, B). Radiographs and behavioral assays (von Frey, grip strength, gait, open field) were evaluated up to 8 weeks **[3,4,5]**. Data was analyzed using repeated measures two-way and one-way ANOVA.

RESULT: All animals survived the procedures. Data are from female mice, as the male cohort was underpowered and females were chosen given evidence of greater discogenic pain **[6]**. Mild and severe IVD injuries reduced von Frey thresholds by 92% ($p = 0.02$) and 87% ($p = 0.05$, pre-surgery vs. week 8), indicating hypersensitivity (Fig. 2A). Severe injury also decreased grip strength by 28% ($p = 0.03$; Fig. 2B), increased stance/swing ratio by 89% ($p < 0.001$; Fig. 2C), and reduced open-field distance by 30% ($p = 0.1$; Fig. 2D). Compared with sham, severe injury lowered von Frey thresholds by 77% and grip strength by 32% (both $p < 0.001$; Fig. 2A, B). X-rays at week 8 showed trends of reduced disc height, altered wedge angle/shape (Fig. 2E, F), and decreased lumbar lordosis. Magnified L4–L5 views confirmed these changes, with osteophytes observed at some injury sites (red arrow, Fig. 2F).

DISCUSSION: This study established and characterized a surgically induced mouse model of lumbar discogenic pain. Both mild and severe IVD injuries produced behavioral and structural changes, with more pronounced effects in severe cases. Building on prior IVDD models **[1,2,7]**, deep phenotyping revealed pain-like behaviors paralleling human IVDD, including hypersensitivity, anxiety-like responses, reduced strength, altered gait, and sagittal curvature changes **[6]**. Importantly, severe injury with osteophyte formation and sagittal imbalance recapitulates spinal conditions associated with chronic pain in humans **[8]**. Ongoing work is increasing sample size to assess sex differences, compare injury severity, and perform microCT and histological analyses.

SIGNIFICANCE: Comprehensive characterization of structural, functional, pain-like, and anxiety-like changes following lumbar IVD injury establishes a clinically relevant discogenic pain mouse model that mirrors spine osteoarthritis and its associated pain, providing a platform for genetic manipulation, mechanistic studies, and therapeutic screening to advance translation to human back pain.

REFERENCES:[1]Tang SN+ Front Pain Res.,2022.[2]Tang SN+ Biomaterials.,2024.[3]Deuis JR+ Front Mol Neurosci.,2017.[4]Lai A+JOR., 2015.[5]Gyles TM+ Neuropsychopharmacology., 2024. [6] Rowland B+ Pain Medicine., 2025. [7] Millecamps M+ Pain., 2018. [8]Goode AP+ Curr Rheumatol Rep., 2013.

ACKNOWLEDGEMENTS: We gratefully acknowledge Dr. Devina Purmessur, Khady Dio & Yuzhang Liu, for training on the surgically induced mouse IVDD model. Supported by NIH/NIAMS grants R01AR078857 and R01AR080096.

Figure 1

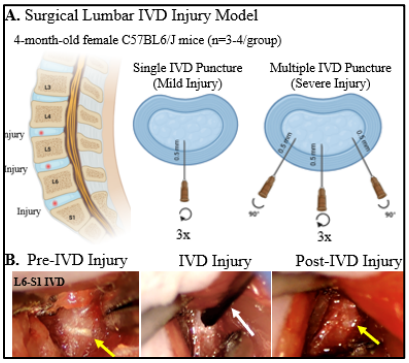

Figure 2

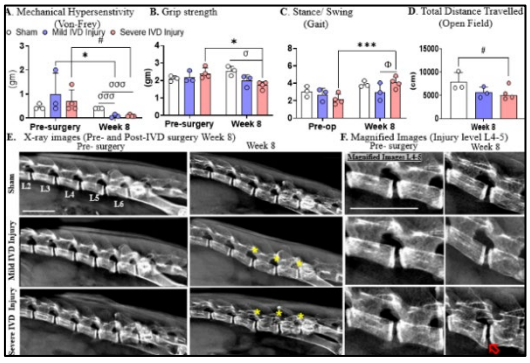

Figure 1. Mouse Lumbar Discogenic Pain Model. A. Lumbar IVD injury (L4–S1): mild injury=single puncture with 3×0.5 mm rotations; severe injury = multiple punctures with rotation and twisting. **B.** In vivo IVD images before, during (white arrow- needle + stopper), and after injury (yellow arrows indicate IVD). **Figure 2. Mild and severe IVD injuries in mouse lumbar spine elicit pain-like behaviors, decreased grip strength, gait abnormalities, anxiety-like behavior, and osteophyte formation. A–D.** Behavioral outcomes pre- and 8 weeks post-injury: (A) Mechanical Hypersenstivity using Von-Frey, (B) Grip strength, (C) Gait Stance/Swing, (D) Open-Field Total Distance Travelled by mouse. **E.** Spine X-rays pre- and post-surgery week 8 (sham, mild injury, severe injury). **F.** Magnified L4–L5 IVD X-ray; red arrow= osteophyte.*, $p < 0.05$; ***, $p < 0.001$ (Pre vs. Week 8); σ, $p < 0.05$ (Sham vs. Mild Injury vs. Severe Injury); #, $0.05 < p \leq 0.1$ (Pre vs. Week 8); Φ, $0.05 < p \leq 0.1$ (Sham vs. Mild Injury vs. Severe Injury)

Internal Fixation of Pediatric Knee Osteochondral Defects: Outcomes at 6-Year Mean Follow-Up

Edmund Corcoran[1], Mohamed Said[2], Edina Gjonbalaj[2], Leila Mehraban Alvandi[2], Mauricio Drummond[2], Eric Fornari[2]

[1]Albert Einstein College of Medicine, Bronx, New York
[2]Division of Pediatric Orthopedic Surgery, Montefiore-Einstein, Bronx, New York

Introduction: Osteochondral defects (OCDe) of the knee in pediatric patients can significantly affect long-term joint function. While numerous surgical modalities are available for treatment of these injuries, long-term pediatric outcomes after internal fixation of native fragments have not yet been reported.

Methods: This IRB-approved retrospective study included 24 patients (25 knees) who underwent internal fixation of full-thickness OCDe between January 2012 and December 2023 at an academic tertiary care center. Demographic and clinical data, including lesion location, size, and method of fixation, were collected via chart review. Updated patient-reported outcomes (PROs; Tegner-Lysholm, Pedi-IKDC, KOOS) and brief functional and satisfaction surveys were obtained via telephone interviews. Mann-Whitney U tests were used to compare PROs between fixation methods.

Results: A total of 24 patients (25 knees; mean age 15.39±2.08; mean BMI 25.87±5.93; 66.7% male; 33.3% Hispanic, 37.5% Black, 16.7% White; 50.0% public insurance) were included. Mean follow-up was 6.17 years (range 2.37-11.48 years) post-operation. Mean lesion area was 4.12±2.23 cm^2. Methods of fixation included metal screws (n=16), bioabsorbable screws only (n=6), a combination of bioabsorbable screws and chondral darts (n=2), and suture fixation (n=1). Of the 16 knees with metallic screws, 10 (62.5%) had complete hardware removal, 2 (12.5%) had partial removal because a portion of the hardware could not be safely retrieved, and 4 (25%) had retained hardware. One patient underwent a second surgery on the same knee to treat patellar instability in addition to complete hardware removal. No other patients underwent secondary surgery, and no post-operative complications were observed. 20/24 (83%) patients reported being satisfied with their surgery, and 22/24 (92%) reported they were able to return to their pre-injury level of sports activity. PRO scores demonstrated strong functional recovery and durable positive outcomes with no significant differences observed between metallic and bioabsorbable implants.

Conclusion: Internal fixation of native fragments in pediatric OCDe yielded high satisfaction, excellent return-to-sport rates, and strong PRO scores at a mean 6-year follow-up. Metal screws frequently required hardware removal, while bioabsorbable/suture fixation avoided reoperation with equivocal patient outcomes. Fixation appears to be a reliable and safe strategy for managing OCDe in young patients.

Significance: While debridement and marrow stimulation have long been considered the gold standard for osteochondral defects, internal fixation achieves high patient satisfaction and strong patient-reported and functional outcomes at mid- to long-term follow-up.

Patient-Reported Outcomes by Fixation Type

PRO Score	Median (IQR), Full Cohort	Median (IQR), Metal	Median (IQR), Bio	p-value
Tegner	80.0 (74.5–86.0)	84.0 (77.0–88.0)	77.0 (70.0–80.0)	0.210
IKDC	77.6 (70.4–87.1)	78.2 (75.9–88.5)	72.4 (66.7–86.2)	0.152
KOOS-Pain	81.2 (71.1–88.3)	84.4 (76.6–89.1)	78.1 (65.6–87.5)	0.472
KOOS-Symptom	82.1 (69.6–89.3)	85.7 (75.0–91.1)	71.4 (64.3–82.1)	0.072
KOOS-ADL	86.4 (81.8–96.6)	88.6 (81.8–97.7)	84.1 (81.8–93.2)	0.786
KOOS-Sport	78.6 (66.1–89.3)	82.1 (69.6–92.9)	67.9 (57.1–82.1)	0.188
KOOS-QOL	79.2 (62.5–84.4)	79.2 (62.5–85.4)	83.3 (66.7–83.3)	0.696

Table 1: PRO scores for the full cohort and stratified by fixation type. Values are reported as median with interquartile range (IQR). Mann-Whitney U testing revealed no significant differences between metallic and bioabsorbable techniques.

So Many Surgeries: Can we minimize the number of surgeries performed for deformity correction in Severe Early-Onset Blount Disease?

Ofir Horovitz, Zachariah Samuel, Mohamed Said, Leila Alvandi, Edina Gjonbalaj, Melinda Sharkey

Montefiore Einstein Department of Orthopaedic Surgery, Bronx, NY

Introduction: A subset of patients with early-onset Blount disease undergo multiple surgeries during childhood to fully correct their lower extremity deformity. Early recognition of patients at highest risk for repeated interventions may allow for the development of surgical strategies that minimize the overall number of procedures. This study aimed to identify preoperative clinical and radiographic factors that differentiate patients who require multiple corrective surgeries from those who achieve definitive correction with a single operation.

Methods: An IRB-approved retrospective analysis was conducted on patients surgically treated with early-onset Blount Disease between 2008 and 2024 at an academic, tertiary care center. Patients were categorized into two groups: those who underwent a single corrective procedure and those who required two or more, excluding hardware removal. An age-matched analysis was conducted to ensure comparable age at most recent follow-up. Demographic data and preoperative radiographic parameters, including Langenskiöld stage, Drennan angle, mechanical lateral distal femoral angle (mLDFA), and mechanical axis deviation (MAD), were compared between groups using chi-square and Fisher's exact tests.

Results: 24 limbs were included (12 single surgery, 12 multiple surgeries). The groups were similar in age at diagnosis (mean 6.2 vs. 5.9 years, p=0.74) and age at most recent follow-up (mean 13.0 vs. 13.9 years, p=0.56). Patients who required multiple surgeries were significantly more likely to present with advanced Langenskiöld stages IV or V (72.7% vs. 18.2%; p=0.042), greater preoperative Drennan angles (28.8° vs. 16.7°; p=0.019), and MAD in zone 3 (100% vs. 33.3%, p=0.008).

Conclusion: Children with early-onset Blount disease who presented with advanced Langenskiöld stage (IV or V), high pre-operative Drennan angle (mean 28.8°) and MAD zone 3 were significantly more likely to require multiple corrective surgeries.

Significance: Patients with severe early-onset Blount disease may benefit from more aggressive initial surgical management to reduce the likelihood of recurrent deformity and repeat procedures. These findings provide surgeons and families with realistic expectations regarding the surgical course required to achieve definitive correction in severe disease.

Table 1: Early-Onset Blount Disease Patient Characteristics Stratified by Number of Corrective Surgeries (excluding hardware removal).

	1 Surgery	2 or More Surgeries	P Value
n	12	12	
Age at Diagnosis (mean (SD))	6.21 (2.60)	5.85 (2.75)	0.743
Age at Most Recent Follow Up (mean (SD))	12.97 (4.17)	13.88 (5.41)	0.647
Female (%)	6 (50.0)	6 (50.0)	1
Race/Ethnicity (%)			0.587
Black or African American	6 (60.0)	4 (40.0)	
Spanish/Hispanic/Latino	2 (20.0)	4 (40.0)	
Unknown	2 (20.0)	2 (20.0)	
BMI Percentile (mean (SD))	97.25 (3.87)	97.20 (3.11)	0.972
Bilateral (%)	9 (75.0)	11 (91.7)	0.584
Initial Type of Treatment (%)			0.822
GG	9 (75.0)	8 (66.7)	
Osteotomy	1 (8.3)	2 (16.7)	
External Fixator	2 (16.7)	2 (16.7)	
Pre-Operative Langenskiöld Stage (%)			**0.042**
1	6 (54.5)	0 (0.0)	
2	2 (18.2)	2 (18.2)	
3	1 (9.1)	1 (9.1)	
4	1 (9.1)	6 (54.5)	
5	1 (9.1)	2 (18.2)	
Pre-Operative Drennan Angle (mean (SD))	16.72 (6.59)	28.84 (15.15)	**0.019**
Pre-Operative mLDFA (mean (SD))	92.49 (3.91)	90.72 (8.58)	0.598
Pre-Operative MAD (%)			**0.008**
1	1 (11.1)	0 (0.0)	
2	5 (55.6)	0 (0.0)	
3	3 (33.3)	10 (100.0)	

Spinal Alignment Device Enables Detection of Sagittal Curvature Changes in a Mouse Disc Degeneration Model

Michelle S. Villagran[1*], Neharika Bhadouria[1], Amanda Kopelman[1], Kaljang Sherpa[1], Philip Nasser[1], Yunsoo Lee[1], Woojin M. Han[1], James C. Iatridis[1]

[1]Department of Orthopedics, Icahn School of Medicine at Mount Sinai, New York, NY

Introduction: Sagittal spinal alignment is critical for spinal function, and disruption contributes to pain and disability in intervertebral disc degeneration (IVDD) and paraspinal muscle dysfunction [1]. Small-animal models allow mechanistic studies, but few assess sagittal alignment, disc height, or paraspinal muscle changes after IVD injury. Prior work links paraspinal muscle injury to sagittal deformity [2] and IVD injury to muscle pathology [3], but sagittal curvature and wedge angles remain unquantified. Whether quadrupeds exhibit alignment changes comparable to humans is unclear, and small size complicates measurement. We aimed to (1) develop a standardized device for mouse sagittal curvature imaging and (2) evaluate the effects of lumbar IVD puncture injury on alignment parameters.

Methods: IACUC-approved. Two devices for in vivo Faxitron X-rays were tested: Prototype 1 (cylinder with cube supports, Fig. 1D) and Prototype 2 (grooved alignment surface with limb support, Fig. 1E). Reproducibility was assessed in naïve C57BL/6J mice (n=20; 10M, 10F) imaged with no device, Prototype 1, or Prototype 2. Injury effects were evaluated in female mice (n=3–4/group; Sham, Mild, Severe) undergoing lumbar IVD puncture. Lateral X-rays were acquired at 8 weeks post-injury with Prototype 2 or no device. Lumbar Cobb, kyphotic Cobb, IVD angle, and IVD height were measured with a MATLAB script using standardized landmarks [4–6]. ANOVA with Tukey's post hoc tests compared conditions.

Results: In naïve mice, lumbar Cobb angle varied by device ($p=0.02$), with Prototype 2 reducing variance compared with Prototype 1 or no device. Prototype 2 improved reproducibility of Cobb angle and IVD height across lumbar levels (Fig. 2A–D). In injured female mice, Prototype 2 detected trends toward decreased lumbar Cobb angle with injury severity ($p=0.05$), reduced kyphotic Cobb angle, and decreased IVD height, consistent with degeneration (Fig. 3A–D).

Discussion: Prototype 2, which stabilizes limbs, improved reproducibility of sagittal measurements over Prototype 1 or no device. Injury across three lumbar IVDs showed trends toward reduced Cobb angle and IVD height, paralleling expected changes in IVDD. Variability at L5/L6–L6/S1 may reflect anatomical differences or vertebral defects. Ongoing work is expanding cohorts and incorporating histology of multifidus remodeling.

Significance: We developed a reproducible device for in vivo sagittal alignment imaging in mice. This method enables longitudinal studies of spinal alignment and muscle remodeling, supporting translational comparisons between rodent and human IVDD.

References: [1] Lafage+ Spine, 2008. [2] Noonan + Sci Rep, 2023. [3] Davies + NASSJ, 2021. [4] Bailey+ J Anat, 2016. [5] Pfirrman+ J Orthop Res, 2006. [6] Hu+ GSJ, 2021.

Acknowledgements: Supported by NIH R01AR080096 and R01AR078857.

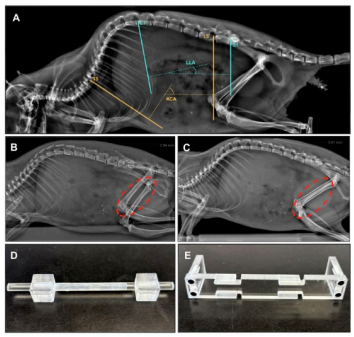

Figure 1. Alignment devices and sagittal curvature parameters in mice: (A) sagittal spinal angles (lumbar Cobb and kyphotic Cobb), (B) lateral X-ray with cylindrical device (Prototype 1), (C) cylindrical device, (D) lateral X-ray with limb holder device (Prototype 2), and (E) limb holder device.

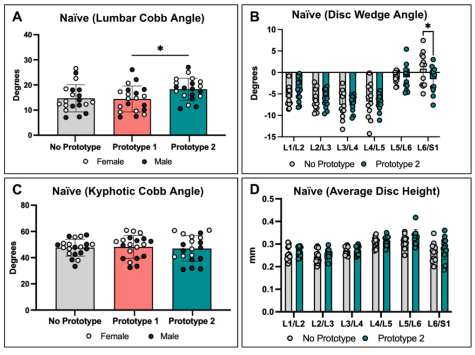

Figure 2. Prototype 2 reduced variability in sagittal spinal angles in naïve C57BL/6J mice (n=20): (A) lumbar cobb angle, (B) disc wedge angle, (C) kyphotic Cobb angle, and (D) average disc height, across no prototype, Prototype 1, and Prototype 2.

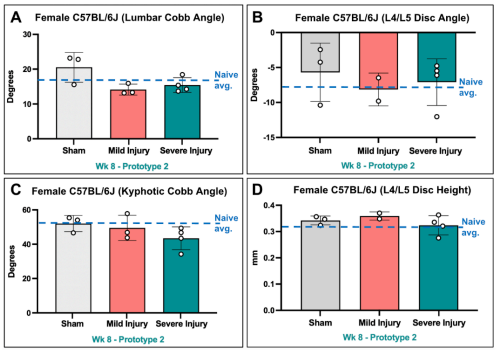

Figure 3. Sagittal spinal deformity at 8 weeks post-injury in C57BL/6J mice: (A) lumbar cobb angle, (B) disc wedge angle, (C) kyphotic Cobb angle, and (D) disc height, with Prototype 2.

Adaptation of the BioDent for Spherical Microindentation to Determine Elastic Modulus in Small Rodent Bones

Authors: Mixame Jerome, Jelena Basta-Pljakic, Mitchell Schaffler*
Affiliations: The City College of New York

Background and Objective: Mechanical and material properties of bone are essential for understanding both normal skeletal function and the progression of bone-related diseases. Microindentation has become a widely used method for evaluating tissue mechanical properties of bone, as it samples the contributions of microarchitecture and composition. Microindentation using a standard Vickers (four-sided diamond) tip introduces both elastic and plastic deformation into the material. In contrast, spherical indentation can be operated entirely in the elastic range, providing for a non-damaging test that has significant advantages over sharp indentation techniques. In the current study, we tested whether a BioDent, Reference Point Indentation (RPI) device, could be reconfigured and repurposed for use as a spherical microindentation system for testing small rodent bones.

Methods: The BioDent system was invented with the idea that bone toughness could be indexed from the indentation depth of a sharp indenter point relative to a reference point at the bone surface. However, this approach was determined to not be as useful as originally hypothesized and its use has fallen into disfavor. At core, the BioDent is a small, controlled loading device containing an actuator, load cell and LVDT. To operate as a true microindenter, we had to: 1) Reconfigure the system software for use under load-control, 2) Remove the reference probe assembly and replace with a custom designed spherical indenter (radius 425µm) and 3) Create and validate new testing procedures for the remade BioDent, which was done using a PMMA calibration standard. After validation, mid-diaphyseal cylinders (5 mm height) were harvested from tibiae of two 16-week-old female SD rats and used to test sensitivity and specificity of the new testing system on cortical bone. Microindentation was performed on PBS-hydrated samples that were then dried (placed in an incubator for 24 hours at 37°C) and tested again; drying is known to increase bone elastic modulus by ~15%. The loading range was from 0.1N to 1N. Elastic modulus was determined using a modification of the Oliver-Pharr method.

Results: Elastic moduli that we measured for the PMMA test block, 2.79 ± 0.16 GPa, were effectively identical to the reference value from the manufacturer (2.8 GPa). Moduli for hydrated bone samples were highly consistent between the different rat tibiae (11.85 ± 2.15 GPa and 11.91 ± 2.87 GPa, respectively). These values fall within the expected range for mature rat cortical bone and point to high reproducibility between tests. Moduli of the same samples after drying increased to 14.45 ± 3.39 GPa and 13.33 ± 2.91 GPa, consistent with the known stiffening effect of water loss on bone.

Figure 1. *Elastic Modulus of PMMA (left). Elastic Modulus of rat cortical bone (right)*

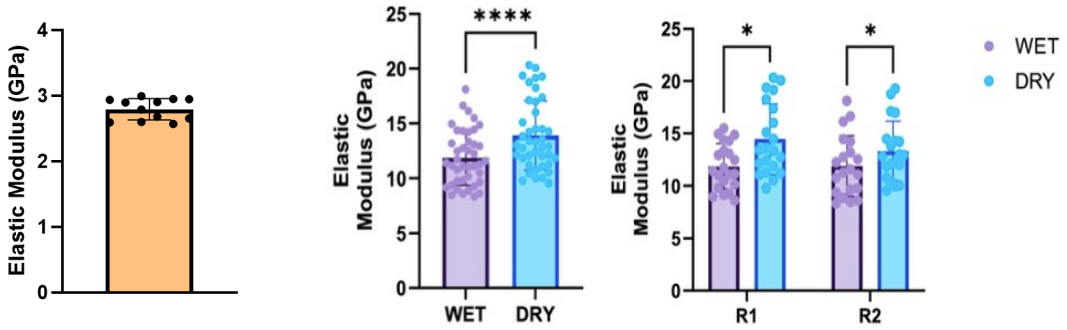

Conclusion and Discussion: The BioDent was successfully adapted into a spherical microindentation tool and demonstrated a high degree of precision and repeatability in rodent bone tests. Further studies are ongoing for different indenter designs that would be useful for small bones. The low forces used to assure that testing was in the elastic range for samples were at the low end of sensitivity for the BioDent. Nevertheless, this modified system shows promise for reliable measurements of bone mechanical and material properties and lends itself as a highly suitable device for *in vivo* testing in small animals. Moreover, the main advantage of using spherical indentation lies in its operation under Hertzian contact in a non-destructive manner which opens its potential for future viscoelastic and dynamic studies.

Perturbation of the mechanical microenvironment disrupts muscle stem cell self-renewal *in vivo*

Josh A. Grey[1], Kelley Tu,[2] GaYoung Park[1], Britney Chin-Young[1], Charlene Cai[1,3], Damien Laudier[1], Woojin M. Han[1]
1. Department of Orthopaedics, Icahn School of Medicine at Mount Sinai, New York, NY, USA; 2. Department of Biology, Brown University, Providence RI, USA; 3. Department of Biology, The College of New Jersey, Ewing, New Jersey, USA.

Introduction: Muscle stem cells (MuSCs) repopulate their niche through self-renewal and quiescence reacquisition to maintain skeletal muscle's regenerative capacity following injury. MuSCs are required for skeletal muscle regeneration, and their impairment is associated with permanent loss of function in conditions such as sarcopenia and cachexia[1,2]. Treatment options for replenishing MuSCs are limited and ineffective, partly due to an incomplete understanding of the niche factors driving cell fate decisions during self-renewal and quiescence reacquisition following activation. We hypothesize that mechanical cues from the MuSC microenvironment play a critical role in regulating stem cell fate during regeneration.

Brief Statement of Methods: We developed a novel injury model that combines barium chloride (BaCl2)-induced injury with a complete, simultaneous tenotomy of the distal tibialis anterior (TA) tendon, thereby removing residual tension and disrupting mechanical homeostasis. To further isolate the role for mechanics on self-renewal, we introduced a delayed tenotomy at 7 dpi when MuSC self-renewal is greatest[3]. 8-12-week old C57Bl6/J mice were randomized into 4 experimental groups for which the injury was performed on one hindlimb each: saline/sham, saline/tenotomy, $BaCl_2$/sham, and $BaCl_2$/tenotomy. The tissues were then allowed to regenerate for 5-,7-,14-, and 28-days post injury (dpi) before sacrifice. To examine the impact of tenotomy on muscle's regenerative capacity, we repeated $BaCl_2$ injections on 28- and 56-dpi in $BaCl_2$/sham, and $BaCl_2$/tenotomy groups and sacrificed at 84-dpi. Experimental and contralateral control TA tissues were then harvested, cryosectioned, and analyzed via histological and immunofluorescent staining.

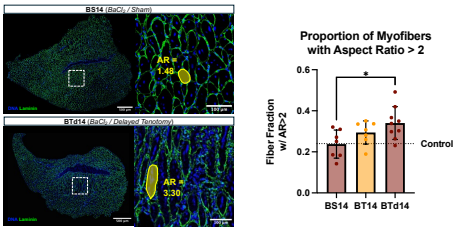

Fig 1. (left) Representative images with inset showing example AR metrics. (right) Proportion of total myofibers with AR >2. One-way ANOVA, Tukey post-hoc, n = 7-8, *p<0.05

Results: Myofiber cross sectional geometry is distorted in tenotomized conditions as indicated by an increased proportion of fibers with an aspect ratio (AR) >2 at 14-dpi. Delineation of central and peripheral regions in cross sections showed a localized distortion effect to the center of tissues (Fig. 1). At 14-dpi, delayed tenotomy results in a more pronounced MuSC loss than either $BaCl_2$ alone or simultaneous $BaCl_2$+tenotomy (Fig. 2). Notably, the loss of Pax7+ MuSC density is significantly lower at the central region of muscle cross sections in the delayed tenotomy condition indicating a stronger disruption of the mechanical microenvironment (Fig. 2). Intriguingly, though the Pax7+ cell density was significantly reduced in the 28-dpi $BaCl_2$/tenotomy group, the repeat injury experiment showed no gross differences in regeneration between $BaCl_2$/sham, and $BaCl_2$/tenotomy conditions (Fig. 3) This suggests that the role of the mechanical microenvironment may be more important at later regenerative stages and may be restored to rescue regenerative capacity in tissues with simultaneous injuries.

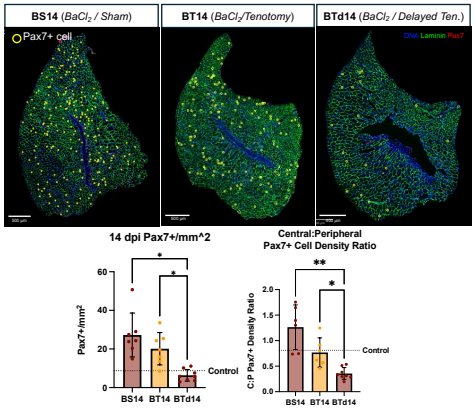

Fig 2. (top) Representative images of 14-dpi cross sections with the location of Pax7+ cells. (bottom left) Pax7+ cell density for 14-dpi cohorts. (bottom right) Pax7+ cell density ratio of central to peripheral regions. One-way ANOVA, Tukey post-hoc, n = 7-8, *p<0.05.

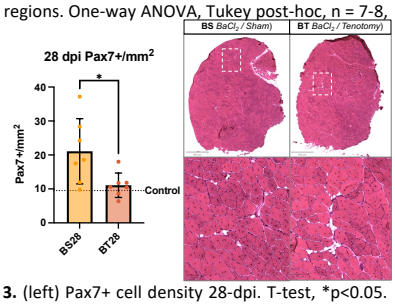

Fig 3. (left) Pax7+ cell density 28-dpi. T-test, *p<0.05. (right) Representative H&E images from repeat injury experiment with myofiber detail in each condition.

Conclusion: This work begins to elucidate the mechanical contribution to the regenerative microenvironment at the niche and whole tissue scale. The results suggest that mechanical cues may play a critical role in self-renewal and niche repopulation during regeneration. Our *in vivo* model establishes a novel method to probe the mechanical contribution to MuSC fate decisions within the physiological niche, effectively uncoupling these stimuli from the systemic biochemical and cellular microenvironment.

Significance: This study provides new *in vivo* evidence that mechanical cues can influence MuSC fate and raise new questions about how the biophysical niche governs stem cell-microenvironment interactions. These findings also suggest broader applications for rehabilitation in acute muscle injuries and can be used to inform platform design for *ex vivo* MuSC culture thereby facilitating their use in cell replacement therapies.

1. Di Girolamo, D. & Tajbakhsh, S. Pathological features of tissues and cell populations during cancer cachexia. *Cell Regen* **11**, 15 (2022).
2. Shefer, G., Rauner, G., Yablonka-Reuveni, Z. & Benayahu, D. Reduced Satellite Cell Numbers and Myogenic Capacity in Aging Can Be Alleviated by Endurance Exercise. *PLOS ONE* **5**, e13307 (2010).
3. Cutler, A. A. *et al.* The regenerating skeletal muscle niche drives satellite cell return to quiescence. *iScience* **25**, 104444 (2022).

Proteome composition and tissue structural dynamics during scar-free ligament regeneration in zebrafish

Authors : Katherine A. Spack[1], Julia Mo, Joanna Smeeton
Affiliations : Columbia University Irving Medical Center, Columbia University; New York, NY 10032, USA

INTRODUCTION: Following injury, humans ligaments demonstrate limited regenerative capacity. When ruptured, ligaments form fibrotic scar tissue with a disorganized extracellular matrix (ECM) that is biomechanically inferior to the uninjured tissue[1]. This limitation in ligament healing capacity is not shared by highly regenerative species like the zebrafish. Following total transection of the interopercular-mandibular (IOM) ligament in the jaw, zebrafish are capable of fully regenerating mechanically competent, scar free tissue[2]. Legumain, a cysteine protease that is known to regulate ECM components, is significantly upregulated in tissue macrophages during this regeneration process. Knockout of Legumain results in developmentally normal zebrafish that generate dysmorphic ligaments with poorly organized ECM following transection. The objective of this study was to define the matrix environment associated with normal regenerative processes in a zebrafish model and identify differentially expressed proteins associated with pro-regenerative, scar free tissue remodeling. To understand the landscape of the normative and fibrotic ligament we quantified the proteomic landscape proteins associated with normal and dysregulated ligament regeneration using label free mass spectrometry. We additionally captured the temporal dynamics of tissue organization using high resolution whole tissue imaging of the collagen network throughout healing.

METHODS: With IACUC approval (AABF1555), complete transection of the IOM ligament was performed on 5-12 month-post-fertilization adult zebrafish as described previously[3]. Joint tissue was collected from uninjured (UI) and three days post-ligament transection (3 dplt) *legumain* wildtype (*lgmn^{WT}*), and *legumain* mutant (*lgmn^{MUT}*) fish. Triplicate pools of tissue from 15 uninjured fish (*lgmn^{WT}* 20M, 25F. *lgmn^{MUT}* 30M, 15F) and from 10 3 dplt fish (*lgmn^{WT}* 14M, 16F. *lgmn^{MUT}* 15M, 15F) were shipped to MS Bioworks for label-free quantitative protein profiling of ligament samples. 500ng of purified protein extracted from each pooled sample was analyzed by LC/MS with a ThermoFisher Vanquish Neo UPLC system interfaced to a ThermoFisher Orbitrap Astral operated in data-independent mode. Peptides were loaded on a trapping column and eluted over a 150µm analytical column heated at 55C at 1.5µL/min with a 30-minute gradient. Full scan MS data (240,000 FWHM resolution) from m/z 380-980 was followed by 300 x 2m/z precursor isolation windows; products were acquired in the Astral at 40,000 FWHM resolution. DIA data were analyzed using DIA-NN (v1.9.2) with database search results filtered at 1% peptide and protein false discovery rates against the Uniprot Zebrafish library. Statistical analysis of captured proteins was conducted using R and Rstudio with the DEP, MatrisomeAnalyzeR, and GSEA packages. Additional *lgmn^{WT}* and *lgmn^{MUT}* fish (M13, F29) underwent IOM transection and were sacrificed at 0, 3, 7, 14, and 28 dplt. Samples were fixed for 24 H in paraformaledehyde, photobleached on a hydrogen peroxide solution, and permeabilized in a KOH solution. Samples were then dehydrated in MeOH to enable efficient anhydrous collagen staining with Fast Green FCF[4]. The tissue was cleared via the iDISCO+ protocol, and collagen architecture was imaged through the full ligament depth with a Leica SP8 confocal microscope.

R**ESULTS:** Proteomic analysis resulted in the detection of 10,023 unique proteins across all samples, including 402 core matrisome and matrisome-associated proteins. In uninjured and 3dplt groups, Legumain was present in all *lgmn^{WT}* samples and absent in all *lgmn^{MUT}*, confirming complete KO. Analyses of *lgmn^{MUT}* and *lgmn^{WT}* samples identify distinct proteomic profiles, with 549 proteins differentially expressed across two or more sample groups (*lgmn^{WT}* UI, *lgmn^{WT}* 3 dplt, *lgmn^{MUT}* UI, *lgmn^{MUT}* 3dplt). During normal healing processes, healing is driven by macromolecular and peptide biosynthetic processes as new matrix is deposited to bridge the injured ligament. Gene ontology analysis of biological processes comparing the *lgmn^{WT}* and *lgmn^{MUT}* samples at the early regenerative 3 dplt timepoint indicate that the greatest differential expression of proteins is found in protein families involved in heterooligomerization and proteolysis. No significant differences were found in fibrillar collagen or elastin content between *lgmn^{MUT}* and *lgmn^{WT}* samples in uninjured or 3 dplt samples. Full-tissue collagen imaging shows greater persistence of proximal ligament stub and in *lgmn^{MUT}* fish and an apparent reduction in crimped collagen fibers following transection.

DISCUSSION: Differences between *lgmn^{WT}*, and *lgmn^{MUT}* proteomic profiles indicate that while legumain is crucial for regenerating ligaments to organize the deposited ECM, it does not directly modulate the ECM composition through regulation of the quantity of major structural ECM components like fibrillar collagens during early ligament regeneration. These data indicate that Legumain is responsible for the differential activation of proteases in early regeneration that govern the crosslinking and clearance of matrix structural proteins. Dysregulation of proteases involved in clearance of damaged matrix and stabilizing deposited collagen via crosslinking results in a disorganized matrix that does not recapitulate uninjured tissue architecture.

R**EFERENCES: 1**. Leong, N. L. *et a. J Orthop Res.* 2020. **2**. Anderson, T. *et al. npj Regen Med* 2023. **3.** Smeeton, J. *et al. Front Cell Dev Biol* 2022. **4.** Timin, G. & Milinkovitch, M. C. *iScience* 2023.

ACKNOWLEDGEMENTS: Funding was provided by Ines Mandl Connective Tissue Fellowship (K.S), National Institute of Health 5F31DE033220-02 (J.M.), and Columbia Stem Cell Initiative Seed Fund Award (J.S.). LC/MS was performed by MSBioworks.

Generation of fibrocartilage cells for rotator cuff repair guided by identification of sequential signaling activation during human fetal enthesis development

Saswati Kar[1], Angel Moonilall[1], Alina Feng[1], Linda Liang[1], Fei Fang[1]

[1]*Leni and Peter W. May Department of Orthopedics, Icahn School of Medicine at Mount Sinai, New York*

Introduction: Rotator cuff injuries are prevalent disorders and the tendon-bone interface (enthesis) at this joint is particularly prone to tearing[1]. Current treatments fail to regenerate the fibrocartilaginous enthesis[2]. Our previous studies in mice showed that transplanting postnatal fibrocartilage progenitors significantly enhanced rotator cuff repair in injured adults[3-4]. Our current work has demonstrated that the human fetal enthesis shares similar cell types and molecular signatures with its mouse counterparts during development. Our work and other reports of stem cell applications in regenerative medicine highlight the potential of cell-based therapies for enthesis repair. Therefore, this study aims to produce a new source of fibrocartilage cells of human-origin for enthesis healing, by (1) evaluating key signaling pathways underlying human fetal enthesis cells specification, and (2) leveraging these molecular cues to direct differentiation of human pluripotent stem cell lines (hPSCs) into the desired cells.

Methods: Human fetal tissues were sourced from elective terminations provided by the Developmental Origins of Health and Disease Biorepository at the Icahn School of Medicine at Mount Sinai. Fetal supraspinatus tendon-bone junction tissues from samples 13 and 17-weeks post conception were sectioned for spatial scRNA-seq. The transcriptomic data was processed, and specific cell types were annotated. Further, the expression levels of signaling factors that were highlighted in prior studies to be essential in early development[5–6] was spatially analyzed. hPSCs were differentiated into the critical sclerotome stage using established protocols[7]. Following sclerotome, fibrochondrogenic differentiation was performed using stepwise activation of signals identified by previous fetal tissue development analysis. The differentiated cells were evaluated by scRNA-seq, qPCR and flow cytometric quantifications. An established chondrogenic differentiation protocol was adopted as a negative comparison[7]. A 3-dimensional tissue formation protocol was adapted from the literature to assess the capacity of the cells to form *de novo* fibrocartilage-like tissue[8].

Results: Fetal enthesis cell types were annotated by spatial scRNA-seq analysis, including two distinct populations of fibrochondrocytes separated spatially and transcriptionally *(Fig 1A-B)*. Gene expression levels of factors related with TGFβ, BMP and Hh pathways were aggregated and shown as a heat-plot to highlight their expression patterns across the cell types at the two time points. TGFβ, BMP and Hh signaling were more enriched in the fibrochondrocytes, specially from 13 weeks *(Fig 1C)*. To evaluate similarity of the differentiated cells to human fetal enthesis cells as the reference, scRNA-seq integration analysis was conducted. Differentiated cells generated by both the fibrochondrogenic and chondrogenic differentiation approaches had overlapping cell types with fetal enthesis cells (*Fig 2A*). A higher proportion of fibrochondrocytes-II were identified in the fibrochondrogenic differentiation condition (*Fig2B-C*). Further, relative expression of a gene-set of known fibrochondrocyte markers was scored for each cell to further compare gene activities among fetal cells and the differentiated cells from the two conditions. Fibrochondrogenic differentiation had more cells with higher scores (brighter) for marker gene-set expression than the chondrogenic condition (*Fig 2C*). qPCR analysis showed fibrochondrogenic differentiated cells had significantly higher expressions of fibrocartilage marker genes (i.e., *GLI1, PDGFRA, SCX, COL1A1, SOX9, COL2A1*) than chondrogenic cells, while their levels were comparable to the fetal cells (*Fig 3*). The differentiated fibrochondrogenic cells could also form 3-dimensional tissue constructs with high collagen I deposition (*Fig 4*).

Discussion & Significance: We have successfully developed a fibrocartilage cell differentiation protocol from hPSCs by decoding molecular cues governing human fetal fibrocartilage formation, which has never been reported before. The differentiated fibrocartilage cells have similar transcriptional profiles, protein expression, and tissue forming ability as the human fetal fibrocartilage cells from the enthesis. Additionally, our differentiated cells show more prominent fibrocartilaginous features, displayed by higher COL-I expression, compared to the cells differentiated using a widely used chondrocyte differentiation protocol. Future studies will evaluate the efficacy of employing these cells for treating a mouse rotator cuff enthesis injury model. Our findings will develop an expandable source of fibrocartilage cells closely related to the natural fetal enthesis cells for translational applications.

References: [1] Zelzer+ Birth Defects Res. C Embryo Today (2014); [2] Galatz+, J Bone Joint Surg Am (2004); [3] Schwartz+ Development (2017); [4] Fang+ Cell Stem Cell (2022); [5] Blitz+ Development (2013); [6] Fang+ Matrix Biol (2021); [7] Wu+ Nat Commun (2021); [8] Gehwolf+ Methods Mol Biol (2019).

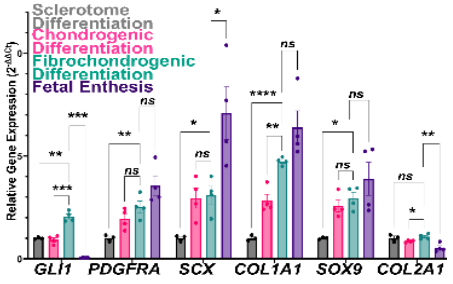

Fig 3: Relative expression of fibrocartilage marker genes in differentiated cells and human fetal enthesis cells normalized over sclerotome. *Not significant (ns), p<0.05 (*), p<0.01 (**), p<0.001 (***),*

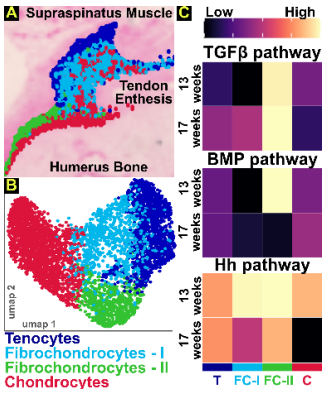

Fig 1: **(A)** Specific cell populations identified at human fetal enthesis by spatial transcriptomics, with **(B)** distinct transcriptomic clusters in the UMAP. **(C)** Relative aggregate expression levels of TGFβ, BMP & Hh pathway genes in the enthesis cell types at 13 & 17-weeks post conception.

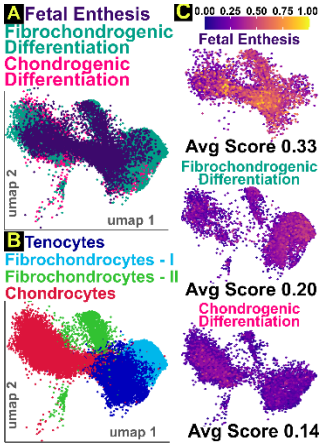

Fig 2: **(A)** scRNA-seq integration of fetal enthesis & differentiated cells showing high transcriptomic overlap. **(B)** Enthesis-specific cell types identified in the integrated UMAP. **(C)** Gene-set based single-cell expression scores for fibrochondrocyte markers in fetal enthesis and differentiated samples. Brighter colors indicate more enriched expression. *Avg Score*-average score from all cells in a sample.

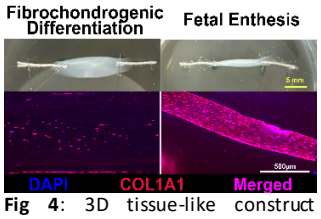

Fig 4: 3D tissue-like construct formation (*top*), with directional cell assembly and Collagen I expression (*bottom*).

Hypoxic Culture Enhances Biomechanical Properties of Engineered Scaffold-Free Tendon Fibers and Upregulates Collagen I, Collagen III, and Lysyl Oxidase

Michael T.K. Bramson[1], **Alessia G. Randazzo[1,2]**, David T. Corr[1,2]

[1]*Biomedical Engineering, Rensselaer Polytechnic Institute, Troy, NY, USA*

[2]*Center for Modeling, Simulation, and Imaging in Medicine (CeMSIM), Rensselaer Polytechnic Institute, Troy, NY, USA*

INTRODUCTION: To better understand tendon development, our lab has established a scaffold-free tendon fiber engineering platform to apply controlled biophysical stimuli *as fibers develop* and evaluate their functional consequences (**Fig. 1**) [1,2]. Given the key role of hypoxia in mammalian development [3], we seek to explore the effects of hypoxic culture on tendon fiber development and functional maturation in our *in vitro* system. Our preliminary work showed that hypoxic culture (5% O_2) improved biomechanical function of engineered tendon fibers, increasing fiber peak stress and moduli compared to normoxic controls, with additional improvements observed with time [4]. In this study, we continue the biomechanical characterization and evaluate the effect of hypoxic culture (5% O_2) on gene expression of engineered tendon fibers over 7 days of development.

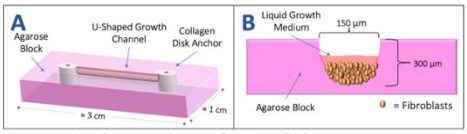

Figure 1: Schematics of (A) 2% agarose growth channel coated with human fibronectin and bounded by collagen disk anchors, and (B) cross-section of cell-seeded channel (modified from [2]). Not drawn to scale.

We hypothesize that hypoxia will enhance biomechanical properties, namely max force, peak stress, Young's modulus, and toughness, compared to normoxic fibers. We also anticipate that hypoxic culture will upregulate expression of *Col1a1*, *Col3a1*, the predominant components of developing tendon ECM, and *lysyl oxidase* (*LOX*), a marker of collagen crosslinking, shown to contribute to biomechanical maturation of developing tendon [5]. Evaluating the impact of hypoxic culture on gene expression and biomechanical properties of developing tendon fibers can provide insight into the biological mechanism(s) that drive the previously observed functional improvements.

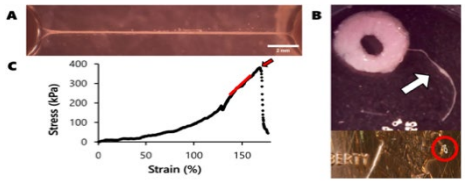

Figure 2: (A) Representative engineered tendon fiber. (B) Fiber (white arrow) attached to collagen anchor, and T-clip (red circle) used to grip fiber for biomechanical characterization. (C) Fiber stress vs. strain curve illustrating Young's modulus (slope of red line), and point of failure (failure strain, peak stress) indicated by red arrow. Toughness is determined as area under curve, from onset of load to point of failure.

METHODS: Fibers were engineered using our established method [2]. Single-fiber growth channels were molded into agarose gels, with collagen disks (4-mm diameter) functioning as anchors for the fiber (**Fig. 1**). Human fibronectin (0.375 mg/mL) was wicked through the channel to promote cell adhesion, and human dermal fibroblasts (HDFs) were seeded into the growth channels at 30 M cells/mL. Seeded channels were cultured in normoxic (21% O_2) or hypoxic (5% O_2) conditions. Cells self-assembled within 18 hours to form continuous fibers (**Fig. 2A**), that were maintained in culture and harvested at 1, 3, or 7 days for biomechanical testing or gene expression analyses via RT-qPCR.

For PCR, samples were homogenized, RNA was extracted and treated, reverse transcribed, and cDNA samples were diluted. Relative gene expression, compared to 1-day normoxic fibers, was calculated using the $2^{-\Delta\Delta CT}$ method, with two replicates per sample. For biomechanical evaluation, fibers were pulled to failure using a custom tensile bioreactor with mN-force resolution [2]. Resulting force-displacement data were normalized by specimen geometry to obtain stress-strain curves, then analyzed to assess fiber strength (peak stress), stiffness (elastic modulus), toughness, as well as toe-in and yield strain (not shown) (**Fig. 2C**). All statistical analyses were conducted using Minitab®.

RESULTS: Biomechanical data show a significant increase in max force, peak stress, Young's modulus, and toughness with hypoxic culture, compared to normoxic (**Fig. 3**). Hypoxic culture significantly upregulated expression of *Col1a1*, *Col3a1*, and *LOX* compared to 1-day normoxic fibers (**Fig. 4**). Expression of these genes did not change significantly with time.

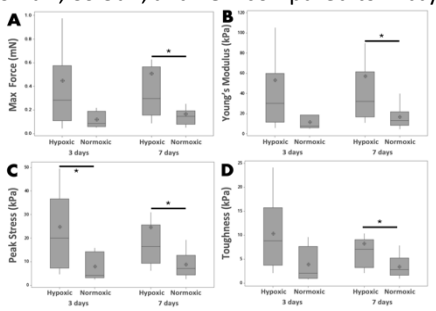

Figure 3: Hypoxic culture significantly increased (A) max force, (B) Young's modulus, (C) peak stress, and (D) toughness compared to normoxic controls.

DISCUSSION: Hypoxia enhanced biomechanical properties of our fibers, with a significantly greater max force, peak stress, elastic modulus, and toughness for fibers grown in hypoxic conditions. These functional enhancements are consistent with increased matrix production and collagen crosslinking, as supported by observed upregulation of *Col1a1*, *Col3a1*, and *LOX* expression with hypoxia, compared to normoxic controls. Hypoxic culture also significantly upregulated *LOX* across all timepoints. *LOX* trended downward with time in culture, which could potentially indicate a decreasing need for this protein as the fiber develops.

Our future work seeks to investigate the resulting collagen structure and composition to complement our genetic and biomechanical observations, thus connecting gene expression, tissue composition, and fiber function. Further, we will explore other macroenvironmental stimuli, such as macromolecular crowding, and their potential synergies with hypoxia to promote tendon development. The work herein provides novel insight into biological underpinnings for use of hypoxic culture to enhance engineered tendon maturation, with potential applications in larger-scale tendon engineering approaches.

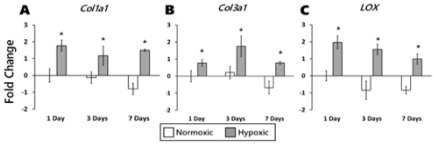

Figure 4: Hypoxic culture significantly upregulated expression of (A) Col1a1, (B) Col3a1, and (C) LOX, with no significant changes observed with time.

ACKNOWLEDGEMENTS: We thank Dr. Connie Chamberlain (UW-Madison) and Dr. Elizabeth Blaber (RPI) for assistance in RT-qPCR experimental design and interpretation of results.

REFERENCES: [1] Schiele, N. et al., Tissue Eng. Pt. A, 2013. [2] Mubyana, K. et al., Tissue Eng. Pt. A, 2018. [3] Dunwoodie, S.L., Dev. Cell, 2009. [4] Bramson, M.T.K, Thesis, 2023. [5] Marturano, J., Acta Biomat., 2014.

The Orthopaedic Impact of Chronic Kidney Disease and Associated Mineral and Bone Disorder – A Comparative Analysis of Clinical Profiles and Laboratory Markers

Authors: Rami Abuqubo, BS; Steven Maxwell Henick, MD; Mohamed Said, MS; Edina Gjonbalaj, BS; Leila Mehraban Alvandi, PhD; Melinda Sharkey, MD

Affiliations: Montefiore-Einstein Department of Pediatric Orthopaedic Surgery

Objective: Children with chronic kidney disease (CKD) frequently develop mineral and bone disorder (MBD), resulting in bone deformities, fractures, and substantial long-standing functional disability. This study examines how CKD-MBD affects orthopedic presentations for surgical and non-surgical management within a pediatric and adolescent population.

Methods: A retrospective review was conducted of 66 pediatric patients with CKD who presented to Montefiore's pediatric orthopaedic surgery division. Patients were categorized into CKD-MBD (n=30) and CKD without MBD (n=36) groups. Data collected included patient demographics, orthopedic and nephrology diagnoses, treatment history, laboratory values (hemoglobin, hematocrit, potassium, blood urea nitrogen [BUN], creatinine, and intact parathyroid hormone [iPTH]) within 3 months prior to and 1 year after the initial orthopedic consultation, non-operative and perioperative complications, and transplant status. Statistical significance was set at $p<0.05$.

Results: Surgical intervention was confined to the CKD-MBD group, affecting 35% of patients (11/31; $p<0.001$), with 1 ± 1 surgeries per patient ($p=0.003$) and more orthopaedic clinic visits (6 ± 7, $p = 0.008$). Mean age at initial renal consultation was higher in the CKD-MBD group (8 ± 6 years) than in the CKD non-MBD group (6 ± 5 years; $p = 0.077$). A history of ESRD and HD was also higher in the CKD-MBD group, with 35% (11/31) having active ESRD and 29.0% (9/31) on dialysis at initial orthopaedic presentation. Advanced CKD was more common in the CKD-MBD group, with 35.5% (11/31) having a prior kidney transplant for ESRD and 32.3% (10/31) with active stage 5 CKD, whereas the CKD non-MBD group predominantly presented with early to moderate stages (CKD 1-3). Across the follow-up period, mean CKD stage remained higher in the CKD-MBD group (stages 4–5) than the CKD non-MBD group (stage 2, $p<0.001$). Rates of kidney transplantation (67.7% vs. 5.7%), renal osteodystrophy (71.0% vs. 5.7%), and vitamin D deficiency (93.5% vs. 57.1%) were also higher in the CKD-MBD group ($p < 0.001$). Within 3 months pre-consultation, labs showed elevated iPTH in CKD-MBD 87.5% vs 50.0% ($p=0.031$), with persistent abnormalities at 1 year for Hb ($p=0.022$), Hct ($p=0.011$), and BUN ($p<0.001$).

Conclusion: Children with CKD-MBD exhibit persistent laboratory abnormalities, compromised bone quality, and a greater disease burden compared to those without MBD. Despite non-surgical measures, underlying skeletal fragility remains inadequately addressed.

Significance: These findings identify CKD-MBD as a high-risk subset of pediatric CKD and support a tailored multidisciplinary approach integrating orthopaedics, nephrology, and endocrinology to optimize bone health minimize musculoskeletal complications.

Demographic, Orthopaedic, and Renal Profiles of Pediatric CKD Patients by MBD Status			
	CKD non-MBD (n=35)	CKD-MBD (n=31)	p-value
Age at 1st Orthopaedic Appointment, mean ± SD (range)	9 ± 5 (1-18)	9 ± 6 (1-18)	0.709
Number of Orthopaedic Appointments, mean ± SD (range)	3 ± 3 (1-18)	6 ± 7 (1-32)	**0.008**
Primary Orthopaedic Diagnosis, n (%)			0.484
Other Pain, Instability, or Gait Abnormality	4 (11.4)	5 (16.1)	0.579
Fracture/Trauma	9 (25.7)	3 (9.7)	0.092
Infection/Infection-Related	1 (2.9)	1 (3.2)	0.931
Spine Conditions	10 (28.6)	6 (19.4)	0.383
Hip Conditions	3 (8.6)	6 (19.4)	0.203
Lower Extremity (LE) Deformity	6 (17.1)	9 (29.0)	0.250
Upper Extremity (UE) Conditions	1 (2.9)	0 (0.0)	0.343
Tumor/Pathology	1 (2.9)	1 (3.2)	0.931
Orthopaedic Surgical Intervention, n (%)	0 (0.0)	11 (35.5)	**<0.001**
Surgeries per Patient, mean ± SD (range)	0	1 ± 1 (0-6)	**0.003**
Intra-op Complications, n (%)	0 (0.0)	1 (9.1)	
Post-op Complications, n (%)	0 (0.0)	4 (36.4)	
Age at Renal Consultation, mean ± SD (range)	6 ± 5 (0-16)	8 ± 6 (1-17)	0.077
CKD Stage Distribution (≤3 Months of Orthopaedic Consult), n (%)			**<0.001**
Former ESRD/Transplant Patient	1 (2.9)	11 (35.5)	
Stage 1	13 (37.1)	0 (0.0)	
Stage 2	15 (42.9)	4 (12.9)	
Stage 3	16 (45.7)	5 (16.1)	
Stage 4	0	1 (3.2)	
Stage 5	0	10 (32.3)	
CKD Stages (relative to 1st Orthopaedic Consult), mean ± SD (range)			
≤3 Months of Consult	2 ± 1 (1-6)	5 ± 1 (2-6)	**<0.001**
1 Year Post-Consult	2 ± 1 (1-3)	5 ± 2 (2-6)	**<0.001**
2 Years Post-Consult	2 ± 1 (1-6)	4 ± 2 (2-6)	**<0.001**
End-Stage Renal Disease (ESRD)			
History of ESRD, n (%)	1 (2.9)	21 (67.7)	**<0.001**
ESRD at 1st Orthopaedic Appointment, n (%)	0 (0.0)	11 (35.5)	**<0.001**
Hemodialysis (HD)			
History of HD, n (%)	1 (3.0)	18 (58.1)	**<0.001**
HD at 1st Orthopaedic Appointment, n (%)	0 (0.0)	9 (29.0)	**<0.001**
History of Transplant, n (%)	2 (5.7)	21 (67.7)	**<0.001**
Renal Osteodystrophy, n (%)	2 (5.7)	22 (71.0)	**<0.001**
Vitamin D Deficiency, n (%)	20 (57.1)	29 (93.5)	**<0.001**

Hallmarks of Fibrocartilage Cells from Human Fetal Enthesis

Linda Liang, Angel Moonilall, Fei Fang

Leni and Peter W. May Department of Orthopaedics, Icahn School of Medicine at Mount Sinai, New York, NY

Introduction: The enthesis, a fibrocartilaginous tissue that forms the transitional interface between tendon and bone, is essential for joint function but highly susceptible to injury[1]. Current treatments remain suboptimal, often failing to restore native mechanical function. Additionally, the limited understanding of enthesis cell composition and developmental mechanisms poses a major barrier to effective reparative treatments. Therefore, the objective of this study is to characterize the phenotypes and function of fibrocartilage cells from human fetal enthesis.

Method: Fetal supraspinatus tendon enthesis tissues (13–20 weeks gestational age) were obtained from the Developmental Origins of Health and Disease Biorepository at the Icahn School of Medicine at Mount Sinai (ISMMS) and dissected in accordance with the human subject's protocol, New York State laws, and ISMMS regulations. Tissues were cut into ~1 mm^3 pieces and enzymatically digested for cell isolation. Isolated cells were either fixed with 1% paraformaldehyde (PFA) for analysis or cultured in complete MEM-α media. To confirm the proliferation ability of fetal cells, a doubling time assay[4] was performed on the fibrocartilaginous cells as well as tendon tenocytes and cartilage chondrocytes to evaluate the divergence. The freshly digested and fixed cells were used for flow cytometry to preserve their native state, and they were stained with fluorescent antibodies against SOX9, Scleraxis (SCX)[2], and some surface markers, CD200, CD51, and CD73, which have been reported to express in mesenchymal cells of musculoskeletal tissues[3]. The combination of both transcriptional and surface markers to enable future cell sorting applications. Stained samples were analyzed using a BD Symphony A5 flow cytometer with FACSDiva software (BD Biosciences) and further processed with FlowJo for in-depth analysis.

Results: Preliminary histology data showed that the enthesis expressed of both SOX9 and SCX, but with lower expression of SOX9 than chondrocytes and SCX than tenocytes (Fig. 1A). Based on this information, we gated cells with medium-level expression of SCX and SOX9 as fibrochondrocytes. Fetal enthesis cells exhibited a doubling time of 50 (±4.7) hours, significantly longer than to 37 (±4.8) and 39 (±3.5) hours for tendon and cartilage cells, separately (Fig. 1B). Fetal cells have significantly shorter proliferation time compared to mature tenocytes and tendon-derived stem cells (TDSCs), with reported doubling time of 354 (±140) and 508 (±49) hours[4], separately. Interestingly, almost 70% CD51-positive cells were SCX positive (SCX^+) and $SOX9^+$ cells. In contrast, only 15.3% $CD200^+$ and 20.6% $CD73^+$ cells were $SOX9^+$ and SCX^+ cells, indicating that CD51 is more specific for fibrocartilage cells than other surface markers. (Fig. 2). PDGFRα, identified previously as enthesis stem cell markers in our mouse work, was also expressed in $SOX9^+/SCX^+$ fibrocartilage cells, demonstrating consistency between mouse and human enthesis cell features. (Fig. 3).

Discussion: Highly proliferative capacity of fetal enthesis cells compared to adult counterparts explains their better regenerative potential. FACS analysis identified CD51 as a strong surface marker candidate for fibrocartilage cells, which can further help distinguish fibrocartilage cells from tenocytes and chondrocytes. Our study showed a distinct $PDGFR\alpha^+$ with $SOX9^+/SCX^+$ fibrocartilage cells, suggesting the presence of enthesis stem cells at the human fetal stage. Future studies are needed to comprehensively map composition, molecular profiles, and the function of fibrocartilage cells from enthesis development to maturity.

Significance: This study will provide a better understanding and characterization of fetal fibrocartilage progenitor cells to fill in the gap of what the fibrocartilage cells are.

References: [1] S. Thomopoulos et al. *Tissue engineering. Part A* vol. 17,7-8 (2011) [2] Y. Sugimoto et al. *Development (Cambridge, England)* vol. 140,11 (2013) [3] G. Shi et al. *Human Cell* 36, 2259–2269 (2023) [4]K. Lee et al. *BMC musculoskeletal disorders* vol. 19, 116. (2018)

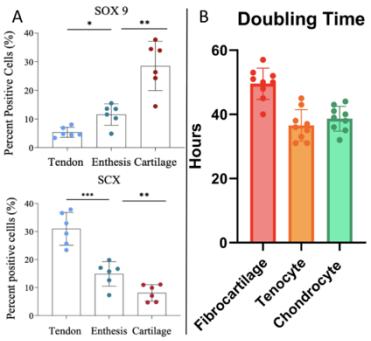

Figure 1: Fibrocartilage cells are distinct from tenocytes and chondrocytes. (A) Histological staining shows that the enthesis region exhibits intermediate levels of SOX9 and SCX expression. (B) Doubling times differ between fibrocartilage, tenocyte, and chondrocyte populations, highlighting distinct growth characteristics.

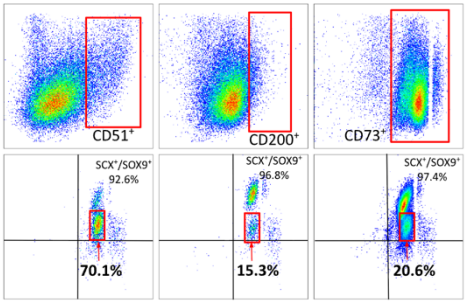

Figure 2: CD51 is identified as the most robust surface marker candidate for the fibrocartilage population. The top row shows all live cells expressing each surface marker (highlighted in red), while the bottom row indicates the proportion of $SCX^+/SOX9^+$ cells within the corresponding surface marker–positive populations, with the putative fibrocartilaginous enthesis cells highlighted in red.

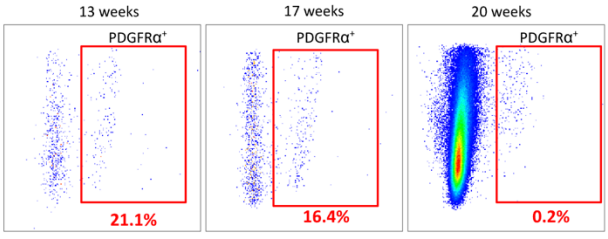

Figure 3: PDGFRα is notably detected in $SOX9^+/SCX^+$ populations. The proportion of $PDGFR\alpha^+$ cells within the $SOX9^+/SCX^+$ population.

Predictability of Polyethylene Insert Size Using an Imageless Robotic System in Total Knee Arthroplasty: A Single-Surgeon Experience

Carlos Salazar, Matthew Goldner, Sun Jin Kim, John Pope, Carlos M Alvarado, Zachary Berliner

Introduction: Two types of robotic systems are used in total knee arthroplasty - imageless and image-based. In preparing reference planes, imageless systems rely solely on user input of anatomic landmarks while image-based systems reference preoperative cross-sectional imaging. Resection levels are then planned based on ligamentous laxity, accounting for implant and polyethylene insert size. We seek to evaluate how often the intended polyethylene size was replicated with the use of a common imageless robotic system.

Method: A prospectively collected, single surgeon database of primary, total knee arthroplasty cases performed with the ROSA Knee System (Zimmer–Biomet, Warsaw, Indiana) was queried. All cases were performed from 2021-2023 at a tertiary academic center, by an experienced, fellowship trained arthroplasty surgeon, including the surgeon's learning curve with this system. Conversion and revision procedures were excluded. Minimum follow-up was 1 year. All cases were completed using a kinematic alignment strategy, aiming for a balanced 22 mm gap in extension and flexion which corresponds to a 10 mm planned polyethylene insert size with 1 mm of varus/valgus laxity. Basic demographic data and polyethylene insert sizes were recorded, as well as the incidence of re-resections.

Results: A total of 400 patients (86 males, 314 females) met inclusion criteria (Table 1). A 10 mm insert was used in 293 (73%) of cases. An 11 mm insert was used in 60 cases (15%). Inserts >11 mm (range 12–14 mm) were used in 47 cases (12%) (Table 2). Re-resections were performed in 32 cases (8%).

Discussion: In this single surgeon series of 400 total knee arthroplasties performed with an imageless robotic knee system, polyethylene insert size of 10-11mm was achieved in 88% of cases. Re-resections were performed in 8% of cases. This may help surgeons understand predictability in balancing with a common imageless robotic knee system. Future research can report postoperative outcomes and compare these measures between imageless and image-based systems.

Rethinking Pain Control in Adolescent Idiopathic Scoliosis Surgery: The Role of the Erector Spinae Plane Block

Authors: Eliana R. Weinstein, BS[1]; Leila Mehraban Alvandi, PhD[2]; Edina Gjonbalaj, BS[2]; Yesmeen Elgabori[1]; William Jackson[3], MD; Jinu Kim, MD[3]; Jaime A. Gomez, MD[4]; Jacob Schulz, MD[2]

Affiliations: [1]Albert Einstein College of Medicine, Bronx, NY; [2]Montefiore Einstein Department of Orthopaedic Surgery, Bronx, NY; [3]Montefiore Einstein Department of Anesthesiology, Bronx, NY; [4]Nicklaus Children's Orthopedics, Miami, FL

Introduction: Posterior spinal fusion (PSF) for adolescent idiopathic scoliosis (AIS) is associated with severe postoperative pain and frequently requires high opioid use. Analgesic strategies in this population remain highly variable, reflecting the lack of consensus on an optimal perioperative approach. The erector spinae plane block (ESPB) is an ultrasound-guided regional technique that may improve analgesia and reduce opioid consumption in this setting [1,2].

Purpose: To evaluate the effect of ESPB as an adjunct to multimodal analgesia on perioperative outcomes in AIS surgery.

Methods: We performed a retrospective review of adolescent patients with idiopathic scoliosis who underwent PSF at a single urban tertiary center between January 2023 and July 2024. Patients were stratified based on whether or not they received an ESPB. Primary outcomes included perioperative opioid consumption and postoperative pain scores (0–10). Patient-reported outcomes were assessed using the Scoliosis Research Society-22r (SRS-22r) questionnaire, comparing preoperative values with scores at 6 weeks postoperatively. Statistical analyses included chi-square and Fisher's exact tests for categorical variables, and non-parametric tests for continuous variables.

Results: Fifty-six AIS patients were included (22 ESPB, 34 no-ESPB). The mean age at surgery was 14.79 ± 2.61 years, and the mean preoperative Cobb angle was 56.83 ± 6.87°. Intraoperative opioid use was similar between the ESPB (0.71 ± 0.28 mg/kg) and no-ESPB groups (0.72 ± 0.18 mg/kg; p=0.260). Inpatient morphine consumption also did not differ (ESPB: 0.07 ± 0.08 mg/kg vs. no-ESPB: 0.09 ± 0.11 mg/kg; p=0.590). However, oxycodone use during hospitalization was significantly lower in the ESPB group (0.42 ± 0.37 mg/kg) compared with the no-ESPB group (0.69 ± 0.45 mg/kg; p=0.023). Postoperative pain scores were consistently lower in the ESPB group, with significant benefit at 12 hours (p<0.05). At 6 weeks, ESPB patients demonstrated greater improvements in SRS-22r pain (1.16 vs. 0.67; p=0.295), satisfaction (1 vs. 0.5; p=0.613), and self-image (0.36 vs. -0.37; p=0.463) domains, with no group differences in function or mental health.

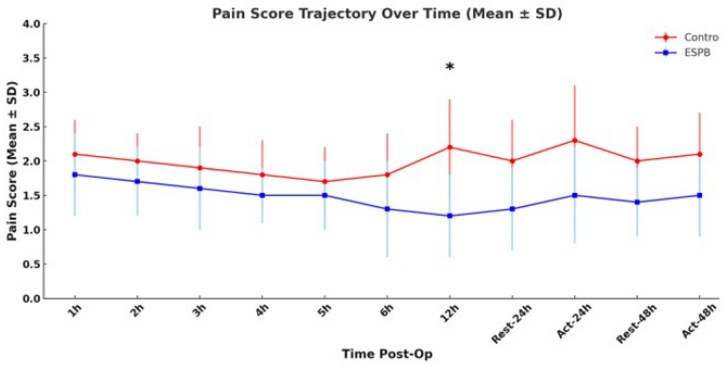

Figure 1. Post-Operative Pain Score Trajectory in the 48-Hours After Surgery

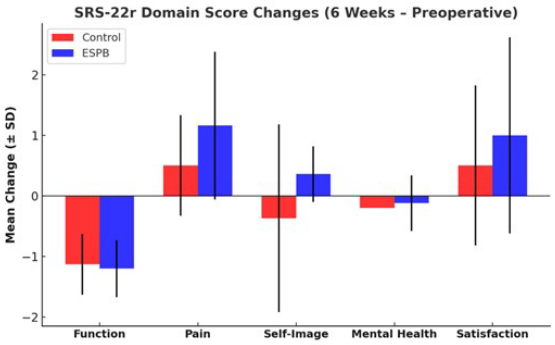

Figure 2. SRS-22r domain score changes from preoperative baseline to 6 weeks postoperatively in control (red) and ESPB (blue) groups.

Conclusion: Use of the ESPB in PSF for AIS was associated with significantly lower oxycodone use during hospitalization, lower early postoperative pain scores, and greater improvements in patient-reported pain, satisfaction, and self-image at 6 weeks.

Significance: These findings underscore ESPB as a safe and effective adjunct to multimodal analgesia in scoliosis surgery and support its integration into enhanced recovery pathways. Larger, prospective multicenter studies are warranted to validate these results and inform clinical guidelines.

References

1. Al-Naseem AO, Alshahomi Y, Almehandi A, et al. Safety and efficacy of erector spinae plane block for perioperative analgesia in posterior spinal fusion surgery for pediatric idiopathic scoliosis: a meta-analysis. Spine Deform. Jul 15 2025.

2. Domagalska M, Ciftsi B, Janusz P, et al. Effectiveness of the Bilateral and Bilevel Erector Spinae Plane Block (ESPB) in Pediatric Idiopathic Scoliosis Surgery: A Randomized, Double-Blinded, Controlled Trial. J Pediatr Orthop. Aug 01 2024;44(7):e634-e640.

Dynamic cell plasticity drives synovial joint regeneration in adult zebrafish

Maria Blumenkrantz[1-6], Felicia Woron[2-6], Maryam Kamel[2-6], Leonardo Campos[4-8], Nadeen Chahine[4-8], Joanna Smeeton[2-6,9]

[1]Integrated Program in Cellular, Molecular, and Biomedical Science, [2]Department of Rehabilitation and Regenerative Medicine, [3]Columbia Stem Cell Initiative, [4]Vagelos College of Physicians & Surgeons, [5]Columbia University Medical Center, [6]Columbia University, [7]Department of Orthopedic Surgery, [8]Department of Biomedical Engineering, [9]Department of Genetics & Development

Objective: Synovial joints are complex organs consisting of lubricated articular cartilage, specialized synovial cavities, and ligaments stabilizing the articulating bones. In humans and mammalian models, mature joint tissues such as articular cartilage have a limited ability to regenerate in their native forms. Currently, we have a poor understanding of both the gene regulatory networks driving articular cartilage cell fate specification, as well as the cellular mechanisms through which joint progenitor cells regenerate and integrate into functional tissues after injury. Although mammalian models are informative in uncovering cells and pathways contributing to articular cartilage development, they repair joint injury with fibrous tissue, not native cell types. The highly regenerative zebrafish, however, can regenerate individual musculoskeletal tissues including bone, tendons, and ligaments as adults. As they also have lubricated synovial joints, zebrafish may be a useful model for dissecting the pathways that enable regeneration of native articular cartilage. Here, we developed a new whole-joint regeneration model to test the capacity of adult zebrafish to perform coordinated regeneration of a synovial joint. We hypothesized that following full resection of the synovial joint, adult zebrafish would exhibit dynamic cell plasticity that resulted in the regeneration of all synovial joint tissue types into a new 3D structure.

Methods: Our lab has devised an adult zebrafish joint regeneration model involving complete resection of the synovial jaw joint, including the synovium, articular cartilage, and joint-supporting ligaments. To assess the re-establishment of mature joint tissue types and functionality of the joint, we used fluorescence *in situ* hybridization, 3D confocal imaging of tissue-cleared fluorescent transgenic zebrafish lines, and immunofluorescence staining using antibodies for muscle and nerves. To characterize the early injury response, we used histological analysis and stereoscopic live imaging of fluorescent transgenic zebrafish. To probe gene expression changes after joint removal, we completed single-cell RNA sequencing at 7 unique time points throughout joint regeneration and performed pseudotime trajectory analysis using Monocle3. Lastly, we used a single-clone lineage trace to delineate the potency of regenerating skeletal cells.

Results: Following whole-joint resection, we find de novo regeneration of articular cartilage, ligament, and synovium into a functional joint by 56 dpjr (days-post-joint resection). The initial injury response involves epithelia enclosing the wound site within 1 hour post-surgery (n=3), with mesenchymal invasion into the wound initiating by 3 dpjr (n=4). By 7 dpjr, epithelial and mesenchymal tissue fully bridge the resected area (n=6), with lineage commitment initiating by 14 dpjr (n=8). Confocal 3D imaging of the tissue-cleared regenerate revealed that *thbs4a_p1:eGFP*+ cells with rounded, articular chondrocyte-like morphology are present by 56 dpjr (n=7). Single-cell transcriptomic analysis of regenerating joint tissues revealed the presence of several fibroblast populations unique to early regeneration (1-7 dpjr). The transcriptional signature of these fibroblasts includes both known genetic drivers of joint development, such as *sox9a*, as well as regeneration-specific genes. Fluorescence *in situ* hybridization for *prg4b*, which encodes lubricin, the lubricating glycoprotein found in synovial fluid, showed that *prg4b* is strongly expressed in cells lining the regenerated joint cavity (n=3 per timepoint). Recovery of muscle and nerve by 56 dpjr was shown via immunofluorescence staining for MF20 and Acetylated Tubulin, respectively (n=4). Imaging inducible *sox10:CreERT2* in combination with *ubi:Zebrabow* transgenic fish revealed that 56 dpjr samples contained predicted clone pairs of distinct mature joint cell lineages, implicating a multipotent population in the adult skeleton as a cell source for regenerating tissues. Thus, our findings establish a new model for de novo regeneration of a functional synovial joint with lubricating articular cartilage.

Conclusions: Our data show that after whole-joint resection in adult zebrafish, the injured site consistently undergoes a wound healing response, mesenchymal bridging, lineage differentiation, and reintegration of all mature synovial joint cell types into a new 3D structure that includes articular cartilage. The dynamic plasticity and differentiation of tissue-resident fibroblasts into distinct types of mature joint cell lineages is a particular strength of our model, enabling the study of not only the regrowth of one tissue type, but the crosstalk involved in regenerating a whole joint organ containing multiple cell types.

Significance: We have developed a reductionist model for dissecting cellular and genetic mechanisms driving endogenous regeneration of synovial joint tissues into an integrated 3D organ. Uncovering factors required for endogenous articular cartilage regeneration will aid future translational studies in improving *in vitro* articular chondrocyte differentiation protocols, advancing tissue-engineering approaches to cartilage repair, and increasing the efficacy of therapies for human degenerative joint diseases. Our model is well-suited for studying the regeneration of joint cell fate and can be used to complement poorly-healing mammalian models towards the translational goal of uncovering targets to enhance the regenerative capacity of the human joint.

Diabetes Mellitus is a Risk Factor for Extended Length of Stay and Non-Home Discharge Following Non-Elective Hip Arthroplasty: A National Inpatient Sample Study

Olivia Stala, BS[1]; Maxwell Ruffner, BS[1]; Priyanka Tiwari, BS[1]; Jay B. Ayar, DrPH, MPH, BDS[1,2]; Anna R. Cooper, MD MPH[3]
[1] *School of Medicine, New York Medical College, Valhalla, NY*
[2] *Department of Public Health, School of Health Sciences and Practice, New York Medical College, Valhalla, NY*
[3] *Department of Orthopaedic Surgery, Montefiore Einstein, Bronx, NY*

Abstract

Purpose: Diabetes mellitus (DM) is a prevalent comorbidity and a known risk factor for adverse outcomes after joint arthroplasty. While its impact on elective procedures is well documented, the effect of DM severity on outcomes following non-elective total hip arthroplasty (THA) and hemiarthroplasty (HA) remains underexplored. Given the increasing burden of DM in the aging population, this study aimed to evaluate how the presence and severity of DM influences extended length of hospital stay (ELOS) and non-home discharge (NHD) following non-elective hip arthroplasty.

Methods: We conducted a retrospective cohort study using data from the National Inpatient Sample (NIS) between October 1, 2015, and December 31, 2019. The NIS is the largest all-payor inpatient database in the U.S., designed to represent a 20% stratified sample of all hospital discharges. Adult patients undergoing non-elective THA or HA were identified using ICD-10 procedural codes. Exclusion criteria included age under 18, elective admission, pathologic fractures, and missing BMI data. DM status was categorized into non-diabetic, uncomplicated DM, and complicated DM using the Elixhauser Comorbidity Software Refined for ICD-10-CM, with complicated DM defined by the presence of end-organ complications such as nephropathy, neuropathy, or retinopathy. The primary outcomes were ELOS (>5 days) and NHD (any discharge destination other than home or home with health services). Descriptive statistics and bivariate analyses were performed using ANOVA and chi-square tests. Multivariable logistic regression models were constructed to assess the association between DM severity and outcomes, adjusting for patient demographics, BMI class, primary payor, and hospital characteristics.

Results: Among 24,484 patients, 25.4% had DM (10.8% uncomplicated, 14.6% complicated), 46.0% experienced ELOS, and 1.8% had NHD disposition. After adjustment, complicated DM was significantly associated with higher odds of ELOS (aOR 1.54, 95% CI 1.43–1.66) and NHD (aOR 1.96, 95% CI 1.78–2.15). Uncomplicated DM was not associated with ELOS (aOR 0.92, 95% CI 0.85–1.01) but had a modest association with NHD (aOR 1.14, 95% CI 1.03–1.26). Female sex was associated with decreased odds of ELOS (aOR 0.74, 95% CI 0.70–0.78) but increased odds of NHD (aOR 1.12, 95% CI 1.05–1.20). Compared to normal BMI, all obesity classes and underweight status were associated with lower odds of both ELOS and NHD.

Conclusions: DM severity independently predicts extended hospitalization and NHD following non-elective hip arthroplasty. Complicated DM, in particular, is associated with significantly worse outcomes. Interestingly, underweight and obese patients had better outcomes than those of normal weight, possibly reflecting an "obesity paradox" or sample bias. These findings support the incorporation of DM severity and BMI class into preoperative risk assessment and discharge planning for this high-risk patient group.

Characterization of ethanol post-treatment on collagen type I scaffolds for pathological tendon modelling

Arnold, KM[1]; Nykypanchuk, D[2]; Schmidt, TA[1]; Deymier, AC[1]
[1]*Biomedical Engineering, School of Dental Medicine, UConn Health, Farmington, CT*
[2]*Center for Functional Nanomaterials, Brookhaven National Laboratory, Upton, NY*

Ethanol dehydration is a common step in both scaffold manufacturing and tissue processing, yet the influence of ethanol on collagen is not well understood. This study examined the effects of dehydration, via ethanol treatment and air drying, on collagen structure, behavior, mechanics, and rehydration capacity. Multiple material characterization methods were used including Fourier Transform Infrared Spectroscopy (FTIR), Raman spectroscopy, Scanning Electron Microscopy (SEM), Thermogravimetric Analysis (TGA), Small/Medium Angle Xray Scattering (SAXS/MAXS), volumetric swelling analysis, and tensile testing. Ethanol dehydration removed bulk water from scaffolds, making them stronger and stiffer, but also showed loss of molecular water. This molecular water appears to act as a collagen stabilizer, resulting in less thermally stable scaffolds. The loss of molecular water is also evident in the molecular d-spacing, which is increased by 0.2 nanometers, the difference in size between a water and ethanol molecule. Secondary structure of scaffolds was also altered by ethanol, resulting in significantly enhanced rehydration capacity. Bulk water, both before and after rehydration, largely determined mechanical properties, which did not correlate with other structural measures such as FTIR. While rehydration largely returned collagen spacing to pre-ethanol treated state, structural alterations seen in FTIR cannot be recovered. These results have implications for not only collagen scaffolds, but in many tissue engineering and processing applications.

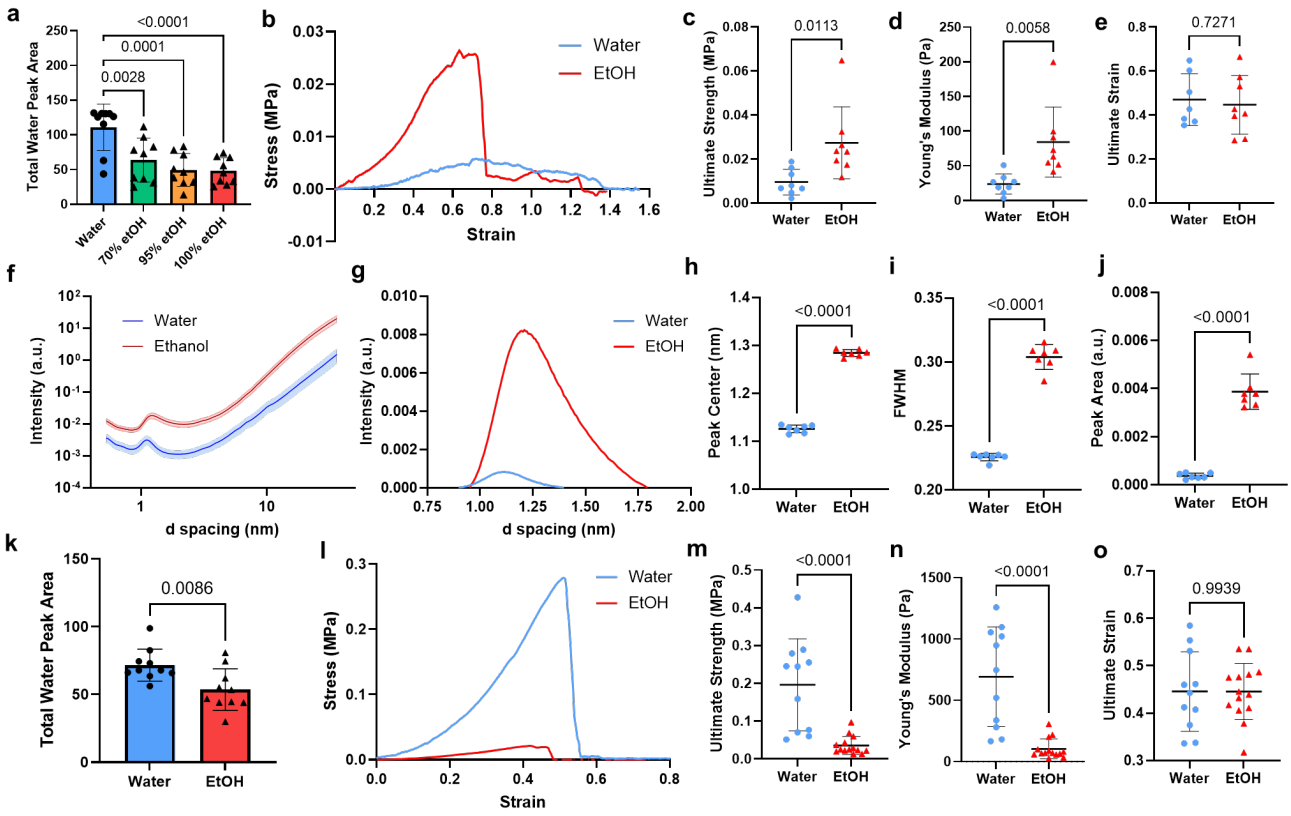

Figure 1: Effect of ethanol on collagen scaffolds. *(a) Ethanol reduces molecular water (b) Stress-strain curve of tensile test (c) Ultimate strength (d) Young's Modulus (e) Ultimate strain of ethanol treated scaffolds (f) MAXS spectra showing molecular spacing peak (g) MAXS representative peak fit of 1nm peak (h) Peak center (i) Full width half max (j) Peak area of 1nm MAXS peak (k) Post-rehydration molecular water (l) Stress-strain curve of tensile test post-rehydration (m) Ultimate strength (n) Young's modulus (o) Ultimate strain of ethanol treated post-rehydration collagen scaffolds.*

Comparing Three *In Vitro* Mineralization Techniques to Model Calcific Tendinopathy Pathogenesis

Angell, C[1]; Arnold, KM[2]; Deymier, AC[2].

[1]*School of Dental Medicine, UConn Health, Farmington CT*
[2]*Biomedical Engineering, School of Dental Medicine, UConn Health, Farmington CT*

Introduction: Calcific Tendinopathy (CT) is a disease involving aberrant mineral deposits in tendons, causing pain and loss of function primarily affecting military personnel and athletes. By creating a model that accurately simulates the molecular pathogenesis of calcific tendinopathy, this study aims to lay the groundwork for future therapeutic discoveries.
Methods: Tendons are almost completely comprised of type I collagen, so ring-shaped collagen I scaffolds made of lyophilized bovine collagen were made in custom molds. Apatite was deposited into the scaffolds via three different methods: Direct Addition (DA), Simulated Body Fluid (SBF), and Polymer-Induced Liquid Precursor (PILP). For DA scaffolds, 10mg/ml of preformed carbonated apatite was mixed into acid soluble collagen before polymerization[1]. For the SBF group, premade collagen scaffold rings were added to 10X SBF for 1 hr. PILP uses a similar ionic solution but with the addition of poly-L-aspartic acid to enable penetration of the amorphous calcium phase into the collagen scaffold over the course of 10 days. The scaffolds' structure and function were assessed via Raman spectroscopy, tensile testing, and Von Kossa staining and histological analysis.
Results: Histology and Raman spectroscopy revealed that all methods resulted in the deposition of apatite, while SBF also resulted in the deposition of brushite. The mineral was distributed throughout the scaffold in DA and exclusively on the surface of the scaffolds with SBF. PILP resulted in only minimal deposition. DA significantly strengthened and stiffened the scaffolds, while SBF dramatically weakened them while increasing their ultimate strain. PILP had no mechanical effect.
Discussion: Different collagen mineralization techniques result in significantly different mineral deposition and scaffold function. PILP was unable to significantly mineralize the scaffolds in the provided timeframe. SBF deposited a variety of crystal types on and within the scaffold surface. These likely act as nucleators for microdamage resulting in decreased strength and stiffness. DA is the only method that resulted in well distributed apatite that shares load with the collagen strengthening the composite. Given the mechanical results and the consistency of mineral deposits, direct addition is the most appropriate method for modelling of calcific tendinopathy.

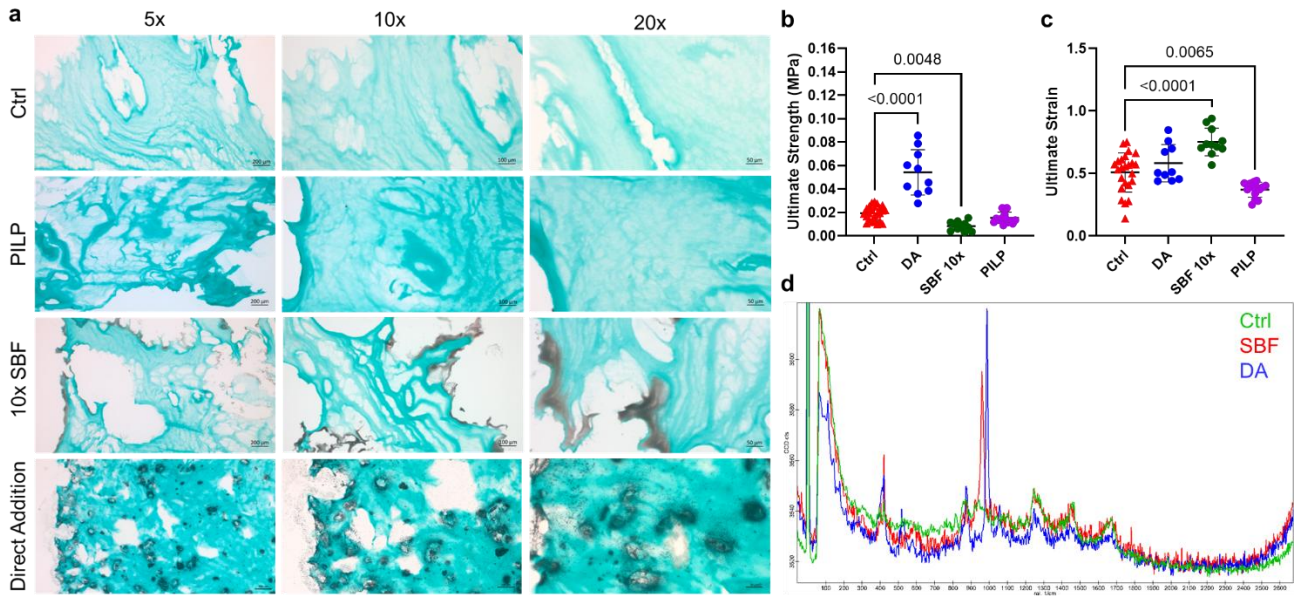

Figure 1: Methods for mineralization of collagen scaffolds. *(a) Von Kossa silver nitrate staining showing deposition of mineral (black/brown) into collagen scaffolds (blue) (b) Ultimate strength of mineralized scaffolds (c) Ultimate strain (d) Raman spectra for each technique (PILP analysis is currently in progress).*

1. Deymier AC, Nair AK, Depalle B, et al. Protein-free formation of bone-like apatite: New insights into the key role of carbonation. *Biomaterials*. 2017;127:75-88. doi:10.1016/j.biomaterials.2017.02.029

Frailty Scores 11-item Modified Frailty Index (11-mFI) and Charlson Comorbidity Index (CCI) Predict Delayed Fracture Fixation in Patients with Intertrochanteric Fractures: An Analysis of the National Inpatient Sample

Jenny Yang, BS[1], Maxwell Ruffner, BS[1], Mary Katharyn Fatehi, BS[1], Victor Koltenyuk, BA[1], Jay Ayar, DrPH, MPH, BDS[2], Elizabeth Drugge, PhD, MPH[2], Anna R. Cooper, MD MPH[1,3]

Affiliations : [1]School of Medicine, New York Medical College, Valhalla, NY;

[2]Department of Public Health, School of Health Sciences and Practice, New York Medical College, Valhalla, NY;

[3]Department of Orthopaedic Surgery, Montefiore Medical Center, 3400 Bainbridge Avenue, 6th Floor, Bronx, NY 10467, USA

Abstract Body

Objectives: Delayed fixation and frailty are established risk factors for patients undergoing fixation for intertrochanteric hip fractures. These variables, however, have been considered independently.[1] This study examines frailty as a risk factor for delayed fixation in patients with intertrochanteric hip fractures.

Methods: A retrospective analysis was performed using fourth quarter 2015 through 2019 data from the Healthcare Cost and Utilization Project (HCUP) National Inpatient Sample (NIS). Adult patients at least 60 years of age with ICD-10-CM code intertrochanteric fracture and ICD-10-PCS codes for insertion of intramedullary internal fixation device were included. Patient characteristics included age, sex, race, income quartile, payor, obesity, medical comorbidity, use of long-term anticoagulation therapy, and receipt of echocardiogram during admission. Institutional characteristics included hospital region, teaching and rural status (rural; urban, nonteaching; urban, teaching), and bed size. Frailty scores were calculated using the 11-mFI and the CCI as discrete variables. Delayed fixation was defined as surgery delayed more than 48 hours after admission.

Bivariate logistic regression was performed to identify significant predictors of delayed surgery with p-value threshold relaxed to $p < 0.2$. Using these initial predictors, one model incorporating 11-mFI and another model incorporating CCI were built using forward stepwise regression. Demographics, hospital characteristics, echocardiogram requirement, and blood thinner status were forced into the final models controlling for other significant predictors. Multivariable logistic regression was used to assess associations between frailty scores and delayed fixation at two-tailed significance level of 0.05.

Results: A total of 16,338 patients with intertrochanteric hip fractures and subsequent fixation were identified. Demographic variables did not differ between groups (Table 1). Of the 866 (5.3%) patients that experienced a delay in fixation, 25 (2.9%) patients required an echocardiogram and 250 (29.0%) patients were on long-term anticoagulant therapy.

The probability of delayed fixation increased 41% for each increase in 11-mFI score (aOR: 1.41, 95% CI: 1.33-1.51) and 13% for each increase in CCI score (aOR: 1.13, 95% CI: 1.10-1.18). In both frailty models (Table 2), independent predictors of delayed fixation also included long-term anticoagulant therapy, receipt of an echocardiogram, and Black, Asian/Pacific Islander as compared to White patients. Protective factors in both models included admission in a medium bed size hospital as compared to large bed size and Midwest or West regions as compared to the Northeast.

Conclusion: The 11-mFI and CCI were independent predictors of delayed fixation for adult patients with intertrochanteric hip fractures. Demographic and regional variance in healthcare outcomes continue to persist. Frailty indices can be useful tools in risk assessment, counseling, and multidisciplinary coordination of care.

Significance: Frailty indices can be useful tools in risk assessment, counseling, and multidisciplinary coordination of care.

References:

1. Klestil T, Röder C, Stotter C, et al. Impact of timing of surgery in elderly hip fracture patients: a systematic review and meta-analysis. *Sci Rep. 2018*;8(1):13933. doi:10.1038/s41598-018-32098-7

Carpal Tunnel Syndrome and Other Predictors of Amyloidosis

Kathryn E. Grabowski[1], Stephen C. Vlay[2], Peter Gorevic[3], Marie A. Badalamente[4], David E. Komatsu[4], Lawrence C. Hurst[4]

Affiliations: [1]Renaissance School of Medicine, Stony Brook University; [2]Department of Cardiology, Stony Brook University; [3]Division of Rheumatology, Allergy and Immunology, Stony Brook University; [4]Department of Orthopaedics and Rehabilitation, Stony Brook University

INTRODUCTION: Amyloidosis is a protein misfolding disease caused by extracellular deposits of amyloid fibrils. As the amyloid protein aggregates, it becomes insoluble and causes organ dysfunction. [1] There are two main types of amyloidosis: amyloid transthyretin (ATTR) and immunoglobulin light chain (AL). Both ATTR and AL amyloidosis can impact cardiac tissue, resulting in fatal disease. [1] Studies have shown that patients with carpal tunnel syndrome (CTS), particularly older adults, may have amyloid deposits in their flexor tenosynovium, but have not yet demonstrated any overt signs of amyloidosis. [1] In an effort to understand risk factors for amyloidosis, a study identified several "red-flag" symptoms and patient characteristics, and placed them in two tiers, based on their predictive value. [2] However, this study did not rank these "red flags" by their individual predictive value. In this study, we used the TriNetX database to assess the relative predictability of each "red flag" so that the risk of a carpal tunnel syndrome patient having undiagnosed amyloidosis could be more accurately assessed before recommending a tenosynovial biopsy at the time of carpal tunnel release.

METHODS: This was a retrospective cohort study of patients with CTS, amyloidosis, and 30 other "red flag" diagnoses. TriNetX contains de-identified data, and therefore, this study was exempt from our Institutional Review Board. The study included electronic medical record data from patients included in the TriNetX Research Network as of September 3rd, 2025. All cohorts were composed of patients with the given diagnoses between January 1, 2010, and December 31, 2019. The CTS cohort included patients with a diagnosis code of CTS, but no prior diagnosis of amyloidosis. The amyloidosis cohort included patients with neuropathic heredofamilial amyloidosis, organ-limited amyloidosis, light chain amyloidosis, or wild-type transthyretin-related amyloidosis. For the cohorts that examined pre-existing risk factors before the CTS diagnosis in patients aged ≥50, all cohorts included patients with CTS but excluded patients who had any prior diagnosis of amyloidosis. The following pre-existing risk factors were examined: African American race, heart failure, trigger finger, diabetes mellitus type 2, atrial fibrillation, aortic stenosis, cardiomyopathy or chest pain, endoscopic CTS surgical release, open CTS surgical release, peripheral neuropathy, lumbar spinal stenosis, total knee arthroplasty, total hip arthroplasty, rotator cuff tear, family history of heart disease, sleep apnea, non-central causes of dizziness, essential hypertension, bilateral CTS, shortness of breath, localized edema, low back pain, diabetes mellitus type 1, digestive issues or abnormal weight loss, floaters, enlarged tongue, diabetic neuropathy, Dupuytren's contracture, distal biceps tendon rupture, and presence of a cardiac pacemaker. Using the compare cohorts feature on TriNetX, each comparison was analyzed after 1:1 propensity score matching for age at index event. The index event was defined as the diagnosis of CTS. For each comparison, the risk of developing amyloidosis in the CTS cohort without the additional risk factor was subtracted from the risk in the CTS cohort with the additional risk factor to yield the risk difference. The risk difference was then scaled to reflect a population of 100,000.

RESULTS: The overall population included in TriNetX consists of 144,092,751 patients across 103 healthcare organizations (HCOs). The prevalence of these conditions in the overall TriNetX population is as follows: 800,662 subjects (0.556%) for CTS and 23,350 subjects (0.016%) for amyloidosis. For the males aged ≥50, 18 of the 30 pre-existing risk factors significantly increased the risk of developing amyloidosis within six years following a CTS diagnosis. For the females aged ≥50, 19 of the 30 pre-existing risk factors significantly increased the risk of developing amyloidosis within six years following a CTS diagnosis. However, the range of the absolute risk difference was lower than that seen in males, with the highest risk factor also found to be heart failure, though with a lower number of 261 per 100,000 compared to 702 per 100,000.

DISCUSSION: For both males and females with CTS, there are several pre-existing conditions associated with an increased risk of developing amyloidosis within six years of the initial CTS diagnosis. These additional risk factors may identify high-risk patients that should be recommended for a tenosynovial biopsy at the time of their CTS surgical release. These results build upon prior studies by ranking comorbidities and drawing from patient populations that are significantly larger, with most cohorts consisting of ≥5,000 subjects, giving this study an unsurpassed level of power. Hand surgeons can use these ranked pre-existing conditions as a diagnostic tool to screen and identify their CTS patients that should be recommended to have a tenosynovial biopsy. The hand surgeon can now better understand how each individual risk factor increases the risk of their CTS patient developing amyloidosis.

SIGNIFICANCE: If asymptomatic amyloid patients with carpal tunnel syndrome can be identified early, then new drugs can potentially slow the deposition of amyloid in major organs. Therefore, taking a sample of a patient's tenosynovium during carpal tunnel surgery who are at risk with these red flags for amyloidosis is important and potentially lifesaving.

REFERENCES: 1. Brown CR, Bergin JD, Deal DN. Amyloidosis and Considerations for the Hand Surgeon - PubMed. *The Journal of hand surgery*. 2024 Mar;49(3)doi:10.1016/j.jhsa.2023.10.013

2. Donnelly JP, Hanna M, Sperry BW, Seitz WH. Carpal Tunnel Syndrome: A Potential Early, Red-Flag Sign of Amyloidosis - PubMed. *The Journal of hand surgery*. 2019 Oct;44(10)doi:10.1016/j.jhsa.2019.06.016

Outcomes after Treatment of Scaphoid Nonunion with Open Reduction Internal Fixation and Corticocancellous vs Cancellous Only Nonvascularized Autograft

Lynn Ann Forrester MD (1), Rafa Rahman MD (2), Raylin Xu MD (2), Michelle Carlson MD (2), Daniel Osei MD (2), Samir Trehan MD (2)

Affiliations : (1) Montefiore Einstein, Department of Orthopedic Surgery, (2) Hospital for Special Surgery, Department of Orthopedic Surgery

Purpose

Optimal treatment of symptomatic scaphoid nonunion remains uncertain. There is compelling data that vascularized bone grafting produces reliable healing of scaphoid nonunions, but it is not without morbidity to the patient, and often requires resources not available to all surgeons. The purpose of this study was to more rigorously characterize outcomes following treatment of scaphoid nonunions with an alternative bone graft option: nonvascularized bone graft.

Methods

We retrospectively identified all patients treated at our institution for symptomatic scaphoid nonunion from 2014 to 2024. Inclusion criteria included patients with a diagnosis of scaphoid nonunion, who had 12 weeks or greater elapse from date of injury (DOI) to time of surgery (DOS), and were treated with operative management. Radiographic healing was defined as 50% or greater bridging bone on CT.

Discussion

149 patients met inclusion and exclusion criteria. Median age at time of surgery was 22 years and the majority of patients included in the study were male (86%). Distribution of nonunion sites included the scaphoid waist (79%), proximal pole (19%), and distal pole (2%). The majority of patients in the study (93%) were treated with open reduction internal fixation (ORIF) with a longitudinal screw or screws, and 104 patients were also treated with nonvascularized autograft bone (cancellous only (CC) or corticocancellous (CO)). The median length of time between DOI and DOS was 277 days, and there was a significantly longer period between DOI and DOS for patients treated with CC compared to CO (median 365 vs 235 days, p=0.004).

96 of these 104 nonunions (92%) healed, with a median time to healing of 81 days. Three patients were lost to follow up. Five patients did not have documented radiographic healing, but all were clinically asymptomatic and had resumed full activities at the time of last follow up. There was no significant difference in likelihood of healing at 12 weeks postop or at time of final follow up for patients treated with CC vs CO graft ($p>0.05$), or in time to healing for patients treated with CC vs CO (median 81 vs 79 days, p=0.99).

Conclusion/Summary

These findings have significant implications for the management and counseling of patients with scaphoid nonunions because over 90% of patients healed when treated with nonvascularized bone graft, a rate higher than previously reported in the literature, suggesting that modern surgical techniques may lead to improved outcomes.

Figure 1: Postoperative Healing by Graft Type

A Shorter Interval Between Preoperative Radiation and Surgery Does Not Increase Wound Complications in Soft-Tissue Sarcoma: A Single Institutional Experience

Authors: Abhijith Annasamudram, Ranxin Zhang, Jichuan Wang, Sung-Suk Chae, Hasibagan Borjihan, Harrison Ho, Yungtai Lo, Rui Yang, Bang H. Hoang, Anna Cooper, David S. Geller

Affiliations: Montefiore Medical Center

Introduction:
Soft-tissue sarcomas (STS) are rare malignant tumors of mesenchymal origin. Limb-salvage surgery combined with radiotherapy (RT) has become the standard of care, improving local control without compromising oncologic outcomes. Preoperative RT (preRT) offers advantages including reduced dose and smaller treatment volumes but carries a higher risk of wound complications. The optimal interval between RT completion and surgery remains controversial.

Methods:
This single-institution, retrospective study evaluated extremity STS patients treated from 2014–2024. Inclusion criteria: high-grade, ≥5 cm, extremity STS treated with preRT and surgery. Data on demographics, comorbidities, ASA score, histology, RT-to-surgery interval, chemotherapy, flap reconstruction, and wound complications were analyzed. Patients were dichotomized at the median RT-surgery interval (33 days). Logistic regression was performed to identify independent predictors of wound infection.

Results:
Fifty patients met inclusion criteria. Twenty (40%) developed deep wound infections; 30 (60%) had no wound complications. RT-to-surgery interval was not associated with infection (median 31.5 vs 33 days; $p = 0.62$; <33 vs ≥33 days, $p = 0.56$). Independent predictors of infection included chemotherapy (OR 4.8, 95% CI 1.1–20.2, $p = 0.03$), male sex (OR 5.2, 95% CI 1.0–26.0, $p = 0.04$), and flap reconstruction (OR 4.8, 95% CI 1.2–18.6, $p = 0.02$).

Conclusion:
Shorter RT-to-surgery intervals (<33 days) were not associated with higher wound complication rates in extremity STS. Chemotherapy, sex, and flap use were stronger predictors of postoperative infection. These findings support flexible surgical scheduling after preRT and highlight the importance of multidisciplinary planning to mitigate wound morbidity.

Keywords: Soft-tissue sarcoma, preoperative radiation, wound complications, RT-to-surgery interval

Frail Cancer Patients with Extremity Fractures Treated Surgically are More Likely to have Extended Length of Stay and Nonhome Discharge than Non-Frail counterparts as measured by the 11-item Modified Frailty Index: A National Inpatient Sample Database Analysis

Srinidhi Raghav[1], Madison Weckerly[1], Jay Ayar[2], Naitik Singh[1], Elizabeth D. Drugge[2], Anna R. Cooper[3]

[1]New York Medical College, School of Medicine; [2]New York Medical College, School of Public Health; [3]Montefiore Einstein, Department of Orthopaedic Surgery.

Background: Length of stay and nonhome discharge disposition are of interest to patients and families, physicians, hospital administrators, and insurance payors. Comorbidity indices have been reported to be predictive of adverse outcomes in surgical patients across specialties. This study of surgical patients with extremity pathologic fractures due to cancer examined frailty as categorized by the modified Frailty Index-11 (mFI-11) as a predictor of extended length of stay and nonhome discharge disposition.

Methods: We analyzed a sample of patients from the 2015 Q4 – 2021 National Inpatient Sample (NIS) who were identified as at least 18 years of age, had both pathologic fracture and cancer diagnosis by diagnostic codes, and surgical procedural codes for that acute care episode. Frailty was assessed using the mFI-11 and categorized as high-risk (≥0.27) or low-risk (<0.27). The primary outcomes were non-home discharge (NHD) and extended length of stay (ELOS, >6 days). Weighted multivariable logistic regression was performed to evaluate associations between frailty status and each outcome, adjusting for age, sex, race, income, primary payor, obesity, and hospital characteristics. All tests were two-sided and $p<0.05$ was considered statistically significant. Significant interactions were examined using predictive margins, with Bonferroni correction applied for pairwise comparisons.

Results: A total of 5,330 adult patients with a pathologic fracture, a cancer diagnosis, and a surgical procedural code were included. Of these, 71.6% had a lower extremity fracture, 24.2% had an upper extremity fracture, and 4.2% had both. The majority were female, 55.5%, and White, 73.4%. The most common primary payor was Medicare, accounting for 60.5% of cases. There was a balanced distribution of income quartiles and hospital regions within the U.S. Of the total study sample, 23.3% were classified as high-risk mFI-11. The overall prevalence of NHD was 2,966 (55.6%) and ELOS was 2,587 (48.5%).

In the weight-adjusted odds ratios (aOR) for predictors of NHD, the mFI-11 (high risk versus low risk) showed significant associations overall aOR 1.46 (95% CI, 1.27-1.68), stratified by upper extremity fractures aOR 1.71 (95% CI, 1.28-2.28) and lower extremity fractures aOR 1.43 (95% CI, 1.20-1.70). Additional independent risk factors included age, female sex, Black vs. White, Medicare vs. private payor, obesity, and Northeastern and Midwestern vs. Southern hospital. Many of these risk factors remained significant when stratified by upper and lower extremity location.

In the weight-adjusted odds ratios (aOR) for predictors of ELOS, the mFI-11 (high risk versus low risk) showed significant associations overall aOR 1.74 (95% CI, 1.52-1.99), stratified by upper extremity fractures aOR 1.96 (95% CI, 1.48-2.59) and lower extremity fractures aOR 1.68 (95% CI, 1.43-1.98). Comparisons of Black to White patients showed significant associations overall aOR 1.50 (95% CI, 1.25-1.79) which was maintained when limited to only lower extremity fractures aOR 1.62 (95% CI, 1.31-2.00). Additional independent risk factors of ELOS were female sex, obesity, rural vs. urban teaching hospital, large bed size hospital, and Northeastern vs. Southern region.

Discussion and Conclusion: High risk stratification by the 11-item Modified Frailty Index was significantly predictive of nonhome discharge disposition and extended length of stay in patients admitted for extremity pathologic fracture surgery. Differences between lower and upper extremity location was less impactful than other factors such as sociodemographic and regional practice differences. These findings underscore the utility of preoperative frailty screening in patient-centered care, multidisciplinary coordination, discharge planning and longitudinal care pathway development.

Distressed Communities Index and Postoperative Outcomes in Geriatric Hip Fracture Patients

Maggie Fagan, Jessica Chao, Brandon Wang, Mohammed Bashier, Megan Darrell, Dylan Horan, MD, Leila Alvandi, PhD, Wanda Horn, MD, Mani Kahn, MD

Albert Einstein College of Medicine and Montefiore Medical Center

Background

Hip fractures are a major cause of morbidity and mortality among older adults worldwide, with mortality rates as high as 36% within one year. Socioeconomic status (SES) has been implicated in surgical outcomes, but its impact remains difficult to measure. The Distressed Communities Index (DCI), a composite metric based on zip code–level socioeconomic data, has recently been applied to surgical outcomes. This study evaluated the association between DCI and postoperative outcomes in geriatric hip fracture patients at a large tertiary academic center in the Bronx, NY.

Methods

We conducted a retrospective cohort study of patients ≥65 years who underwent operative fixation for femoral neck or intertrochanteric fractures between January 2019 and September 2022. Patients were categorized into quintiles based on DCI scores, ranging from prosperous (least distressed) to distressed (most distressed). Primary outcomes included in-hospital, 30-day, and one-year mortality. Secondary outcomes included time to surgery, length of stay, time to ambulation, postoperative complications, and follow-up within three weeks. Statistical analyses were performed with chi-squared/Fisher's exact tests and Mann-Whitney U tests, with Benjamini-Hochberg correction applied for multiple comparisons.

Results

A total of 482 patients were included, of whom 124 (25.7%) resided in high-distress zip codes and 358 (74.3%) in low-distress zip codes. Comparison between the most distressed DCI quintile and the remaining quintiles revealed no significant differences in mortality, time to surgery, length of stay, time to ambulation, postoperative complications, or follow-up adherence. The only difference noted was racial distribution, with a higher proportion of white patients residing in the least distressed quintiles.

Conclusion

In this single-institution cohort, DCI was not associated with differences in postoperative mortality or complication rates after hip fracture surgery. These findings contrast with prior multi-institutional studies that demonstrated worse outcomes among patients from more distressed communities. The high baseline level of socioeconomic distress among the Bronx population may have limited variability in DCI scores and reduced the ability to detect outcome disparities. Additionally, institutional resources such as dedicated geriatric co-management, social support services, and community-based programs may mitigate the effects of socioeconomic disadvantage. Future multicenter studies spanning populations with broader socioeconomic diversity are needed to clarify the relationship between DCI and hip fracture outcomes.

Hyperosmotic Pressure Mimics Mechanical Confinement and Regulate Muscle Stem Cell Fate

GaYoung Park[1], Woojin M. Han[1]
[1] *Department of Orthopaedics, Icahn School of Medicine at Mount Sinai*

Introduction

Muscle stem cells (MuSCs) play a central role in skeletal muscle regeneration, undergoing dynamic transitions in dimensional confinement throughout the repair process [1]. Upon injury, quiescent MuSCs rapidly activate, proliferate, and differentiate to rebuild damaged tissue. At later stages, when regeneration approaches completion, differentiation subsides and MuSCs return to a quiescent state. Although numerous studies have investigated the regulatory factors shaping MuSC fate, such as niche interactions and molecular signaling pathways, the mechanisms remain incompletely understood. Notably, MuSCs reside between muscle fibers, where they are subjected to substantial biomechanical cues during regeneration (Figure 1). Previous findings have identified compression as a determinant of MuSC fate [2], and more recently, our own work demonstrated that confinement similarly influences MuSC behavior [1]. Building on this knowledge, the present study investigates whether elevated osmotic pressure alone can mimic mechanical confinement in vitro and how such conditions impact MuSC stemness, activation, and differentiation.

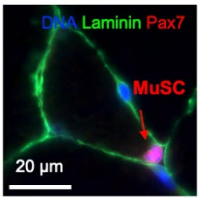

Figure 1. *Immunofluorescence of uninjured muscle.*

Brief Statement of Methods

To investigate whether osmotic pressure can influence MuSC fate, we established an in vitro system in which culture media containing varying concentration of XX Da polyethylene glycol (PEG) was applied in place of a top hydrogel layer. The culture substrate was fabricated from tunable PEG-norbornene (PEG-NB) hydrogels to approximate the stiffness of muscle tissue (12 kPa), and MuSCs were isolated from Pax7EGFP reporter mice and seeded onto the hydrogel surface. After overnight attachment (16–20 h), cells were cultured for five days under four conditions: standard growth medium (GM), GM supplemented with 1% PEG, GM with 2% PEG, or GM with 4% PEG. MuSC fate was evaluated using multiple complementary assays. Pax7EGFP expression was monitored by fluorescence imaging, and GFP intensity was quantified to assess stemness (Figure 2 a,b). Myogenin immunostaining was performed to identify differentiating cells, while DNA staining was used to measure nuclear size and morphology (Figure 2 c,d). This system enabled a systematic comparison of MuSC responses across osmotic environments and provided a controlled framework to test whether osmotic pressure can serve as a surrogate for mechanical confinement in vitro.

Result

The proliferation of MuSCs was markedly reduced in the 4% PEG group compared to other conditions, particularly the isotonic control, while Pax7EGFP intensity remained strongly elevated (Figure 2 a,b). Increasing PEG concentration, and thus increasing osmotic pressure, was associated with decreased proliferation and enhanced maintenance of stemness. Consistent with these findings, Myogenin staining revealed that differentiation was significantly lower in hyperosmotic groups compared to the control growth medium, indicating that hypertonic pressure delays MuSC differentiation. Finally, analysis of nuclear morphology demonstrated a pronounced reduction in nuclear size under higher-pressure conditions, with the smallest nuclei observed in the 4% PEG group (Figure 2 c,d).

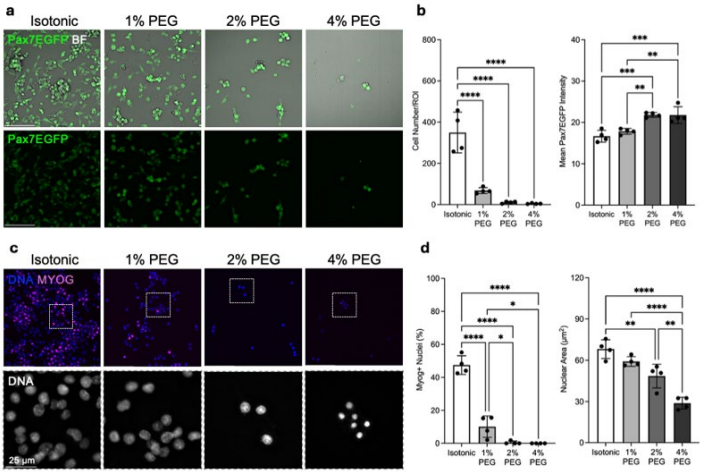

Figure 2. *(a) Pax7EGFP MuSCs cultured in isotonic or PEG-supplemented media. (b) Quantification of cell number and Pax7 intensity. (c) Myogenin (MYOG) and DNA images. (d) Quantification of Myogenin (MYOG) and DNA *p < 0.05, **p < 0.01, ***p < 0.001, ****p < 0.0001.*

Conclusions

Our findings demonstrate that a hyperosmotic in vitro system functions as a mechanical brake on MuSC activation, proliferation, and differentiation, thereby promoting the maintenance of stemness. Modulation of osmotic pressure provides a simple yet effective means to mimic aspects of 3D confinement with highly reproducible outcomes. Moreover, this platform offers flexibility for incorporating diverse ligands, making it a versatile tool for experimental design. As an initial proof-of-concept, this study highlights the potential of controlling osmotic pressure to facilitate future investigations into the mechanobiology of muscle stem cell regeneration.

Reference

[1] Park G.Y., Grey J.A., Mourkioti F., Han W.M. (2025). 3D mechanical confinement directs muscle stem cell fate and function. bioRxiv. https://doi.org/10.1101/2024.10.03.616478
[2] Tao J., Choudhury M.I., Maity D., Kim T., Sun S.X., Fan C.M. (2023). Mechanical compression creates a quiescent muscle stem cell niche. Communications Biology, 6, 104411. https://doi.org/10.1038/s42003-023-04411-2

Title: Improved Healing of Pathologic Long-bone Fractures: Contemporary Outcomes in the Era of Modern Cancer Therapy

Authors : Dylan Horan MD, Deena Najjar BS, Jenna Le MD, Beverly Thornhill MD, Jonathan Sterman MD, Youngtai Lo PhD, Sung-Suk Chae PhD, Ranxin Zhang MD, Jichuan Wang MD, Fnu Hasibagan PhD, Harrison Ho PHD, Abhijith Annasamudram MD, Anna Cooper MD, MPH, Bang Hoang MD, Rui Yang MD, David Geller MD

Departments: Department of Orthopeadic surgery and Oncology, Department of Radiology, Department of Pediatrics

Affiliations : Montefiore Medical center; Albert Einstein College of Medicine, University of Texas at Houston

Background

Metastatic bone disease (MBD) causes significant morbidity, pain, and inferior quality of life. [i],[ii],[iii],[iv] Treatment focuses on improving skeletal stability, with the aim to provide a durable orthopedic solution for a patient's remaining life. Historically, union rates for pathologic fractures were considered according to histology type, with some cancers reliably healing while others exhibited dismal healing rates. These historical rates, which have not been updated in over 40 years, have continued to inform surgeons, influencing the type of surgery recommended and the inherent risks incurred.[v] Given advances in tumor profiling and classification, as well as in adjuvant therapies, a more contemporary review of bone healing is warranted and may improve expectations, decision making, and management recommendations.

Methods:

An IRB approved retrospective review spanning from 2014 to 2024 was conducted at an NCI-designated comprehensive cancer center. Inclusion criteria included patients ≥18 years of age with MBD that either underwent prophylactic fixation (PF) or internal fixation (IF) for MBD. Patients with primary bone malignancies, spinal metastases, and/or treated with endoprosthesis were excluded. The primary outcome was histology specific-bone healing rate, determined by radiographs reviewed by two fellowship-trained musculoskeletal radiologist. Any differences were managed by input from a third musculoskeletal radiologist. Additional data such as overall survival, treatment, and fixation type were assessed as well.

Results:

A review from 2014-2024 has revealed a total of 175 patients who underwent fixation for either an impending or pathologic fracture. Of these patients, 76 were impending fractures and 129 were pathologic fractures. Results demonstrate a marked improvement in healing rates as multiple myeloma, breast cancer, and lung cancer were 96%, 86%, and 92% as compared to historical values of 67%, 37%, and 0% respectively. Additionally, our study demonstrates an improved survival of all subtypes. Lung cancer showed the largest improvement with 39% survival at 6 months compared to previous studies, in which patients did not live beyond 6 months.

Conclusion:

Our review suggests bony union rates have substantially improved from historic values. Additionally, it appears there is near universal healing in multiple myeloma and meaningful potential for bony healing in the setting of other histologies that historically demonstrated poor healing rates. More accurate prognostication, in the setting of molecular profiling, targeted treatments, and immunotherapy, will allow surgeons to make more informed and accurate recommendations. Having accurate and contemporary expectations is of immense importance in guiding patients, making surgical recommendations, and managing complex patients living with metastatic cancer.

[i] Jiang W, Rixiati Y, Zhao B, Li Y, Tang C, Liu J. Incidence, prevalence, and outcomes of systemic malignancy with bone metastases. *Journal of Orthopaedic Surgery*. 2020;28(2).

[ii][ii] Cosphiadi I, Atmakusumah TD, Siregar NC, Muthalib A, Harahap A, Mansyur M. Bone Metastasis in Advanced Breast Cancer: Analysis of Gene Expression Microarray. Clin Breast Cancer. 2018 Oct;18(5):e1117-e1122. doi: 10.1016/j.clbc.2018.03.001. Epub 2018 Mar 8. PMID: 29609951.

[iii] Logothetis C, Morris MJ, Den R, Coleman RE. Current perspectives on bone metastases in castrate-resistant prostate cancer. Cancer Metastasis Rev. 2018 Mar;37(1):189-196. doi: 10.1007/s10555-017-9719-4. PMID: 29380085; PMCID: PMC5801387.

[iv] Bienz M, Saad F. Management of bone metastases in prostate cancer: a review. Curr Opin Support Palliat Care. 2015 Sep;9(3):261-7. doi: 10.1097/SPC.0000000000000157. PMID: 26262831.

[v] GAINOR, BARRY J. M.D.; BUCHERT, PETER M.D.. Fracture Healing in Metastatic Bone Disease. Clinical Orthopaedics and Related Research 178():p 297-302, September 1983.

Investigating the role of AP-1 during zebrafish ligament regeneration

Authors : Safiyah Ali[1,2,3], Troy Anderson[1,2,3], **Joanna Smeeton**[1,2,3,4]
Columbia University Irving Medical Center[1], Department of Genetics & Development[2], Columbia Stem Cell Initiative[3], Department of Rehabilitation and Regenerative Medicine[4]

Ligament injury induces a healing response that is characterized by the formation of a fibrotic scar. This scar tissue is often weaker and lacks the biochemical and biomechanical properties of the native structure (1). To date, there are no effective treatment strategies that can promote a regenerative response to repair ligaments following injury. To enhance ligament healing, it is important to understand the cellular mechanisms that promote scar-free ligament regeneration. Our lab has developed a novel injury model to study scar-free ligament regeneration by utilizing the highly regenerative zebrafish as a model organism. We demonstrate that zebrafish have the capacity to regenerate their craniofacial interopercular mandibular (IOM) ligament following transection without forming a fibrotic scar (2). Ligament regeneration in zebrafish is driven by a series of fate changes where pre-existing ligamentocytes in the left-over ligament stubs lose their ligament cell fate characteristics and undergo dedifferentiation (2). Dedifferentiated ligamentocytes give rise to a regenerative mesenchymal cell population that bridges the injury gap followed by redifferentiation and reestablishing ligament cell fate (2). The transcriptional drivers that promote ligamentocyte dedifferentiation and their ability to adopt a pro-regenerative cell fate are unknown. To define transcriptional drivers, we performed single nuclei assay for transposase accessible chromatin sequencing (snATAC-seq) to identify regions that gain accessibility in regenerative mesenchymal cells after ligament injury and transcription factor binding motifs enriched in these regions. Regions with increased accessibility in regenerative mesenchymal cells have enriched transcription factor binding motifs corresponding to AP-1, Fos::Jun motifs. AP-1 transcription factors consist primarily of Fos and Jun proteins and are immediate-early genes transcribed in response to cellular stress and growth factors. Preliminary experiments demonstrate that the phosphorylation of Jun increases following ligament injury. This suggests Jun is transcriptionally active and likely forming complexes with Fos proteins. In the absence of AP-1 activity, ligamentocytes fail to undergo dedifferentiation suggesting that AP-1 activity is required for ligamentocyte dedifferentiation. Together, this preliminary data showcases an important role of AP-1 during the early stages of ligament regeneration. Future work will help us determine whether AP-1 transcription factor activity is required for scar-free ligament regeneration in zebrafish.

(1) Leong, N. L. *et al.* Tendon and Ligament Healing and Current Approaches to Tendon and Ligament Regeneration. *J. Orthop. Res.* **38**, 7–12 (2020).

(2) Anderson, T. *et al.* Ligament injury in adult zebrafish triggers ECM remodeling and cell dedifferentiation for scar-free regeneration. *Npj Regen. Med.* **8**, 51 (2023).

From Variant to Function: Using Machine Learning to Uncover the Regulatory Syntax Governing Osteoblast Differentiation in Osteoporosis

Chynna Smith[1], Reanna Doña[1], Marliette Rodriguez[1,], John Greally[1,2], Srilakshmi Raj[1]

[1] Department of Genetics, Albert Einstein College of Medicine, Bronx, NY
[2] Department of Pediatrics, Albert Einstein College of Medicine, Bronx, NY

Osteoporosis is a complex bone disease with a strong genetic component, yet the function of the vast majority of non-coding variants identified by genome-wide association studies (GWASs) in this condition remain unknown. To address this gap, we present a powerful framework that integrates population-level genetic data with experimental functional genomics to prioritize functional non-coding variants for experimental validation. We trained a deep learning model, ChromBPNet, on chromatin accessibility data from an ATAC-seq time-course experiment of mesenchymal stem cells (MSCs) undergoing osteogenic differentiation to osteoblasts (bone forming cells). The differentiation of MSCs to osteoblasts as opposed to adipocytes is necessary for the maintenance of healthy bone, and this process is regulated by transcription factor (TF) activity at differentiation-specific loci. We first used our trained model to predict chromatin accessibility from DNA sequence, allowing us to identify key TF binding motifs necessary for early cell fate decisions. We successfully identified TF binding motifs for key osteogenic regulators such as AP-1 and TEAD family TFs.

To identify disease-relevant genetic variation which could impact TF activity at our identified key binding motifs, we integrated our model's regulatory insights with a credible-set of fine-mapped variants reaching genome-wide significance for bone mineral density (BMD) — the primary diagnostic indicator for osteoporosis. By scoring the impact of these variants on our functional data, we identified and prioritized rs570639864, as a candidate functional non-coding variant (FNCV). This single nucleotide polymorphism (SNP) is located within an intron of WNT7B, a gene highly influential in early osteogenic differentiation acting through Wnt/ß-catenin regulated inhibition of adipogenesis. Our model predicts that the risk allele for this variant disrupts a core AP-1 (FOSL:JUNB) binding site, and greatly alters local chromatin accessibility relative to the reference allele. This risk variant occurs at a frequency of 0.2% globally, but at 0.4% in Tuscans and Puerto Ricans and 2.2% in Ashkenazi Jewish individuals, illustrating how it may contribute differently to distinct populations. This study provides a powerful computational framework for translating GWAS associations into functional insights, allowing researchers to test disease-specific hypotheses and identify high-confidence candidates for functional validation studies, which we applied here to understanding osteoporosis in different world populations.

Tendon Type and Health Influence the 3D Organization of Collagen Fibrils Visualized with Machine Learning Assisted Segmentation and Reconstruction of SBF-SEM Images

Kelsey Y. Gsell[1], Lily M. Lin[1], Jamie M. Benson[1], Chandran Sabanayagam[2], Jeffrey Caplan[2,3], Dawn M. Elliott[1]
[1]Department of Biomedical Engineering, [2]Delaware Biotechnology Institute, [3]Department of Plant and Soil Sciences, University of Delaware, Newark, DE

INTRODUCTION: Collagen fibrils are the primary structural unit of connective tissues like tendon. At the nanoscale, the ability of collagen to bear load depends directly on fibril structure [1]. Accordingly, there are structural differences between tendons with distinct functions [2] and structural changes due to damage and injury alter mechanical function [3,4]. Assessing fibril structure within a tissue remains challenging. Electron microscopy provides sufficient resolution but is traditionally limited to a single plane, and fibril segmentation remains a time-consuming and difficult step. While 2D imaging allows for fibril diameter, shape, and density to be measured [5], 3D fibril geometry and organization are required to fully characterize tendon structure and infer its contribution to mechanics. Using serial block face scanning electron microscopy (SBF-SEM), sequential cross-sections can be imaged through a sample volume. We previously demonstrated that tendon fibrils throughout a 3D image stack can be automatically segmented using a U-Net machine learning algorithm [5]. The aim of the current study was to reconstruct and quantify fibril structure in 3D, and to assess potential differences between tendon type and tendon health.

METHODS: SBF-SEM images of 3 rat tendons: tail, plantaris (shown in Fig 1A.), and a plantaris following 8 weeks of chronic mechanical overload in a synergist ablation model, were taken from our previous study [5]. U-Net segmented fibrils were reconstructed in 3D using Amira (ThermoFisher) cylinder tracing shown in Fig 1B. While Amira provides useful visualizations, such as for tortuosity and orientation (seen in Fig C&D respectively), calculations are not always relevant or customizable. Therefore, centroid coordinates (x, y, z) of each fibril were extracted and analyzed in MATLAB to calculate and compare fibril length, tortuosity, and alignment across the 3 tendon samples. Pathlength along the fibril was normalized to the bulk average. Tortuosity, a measure of waviness/twist, was calculated by normalizing pathlengths to the straight-line distance (chord) between the first and last centroid (1 = perfect straight). The general orientation of fibrils was calculated as the relative chord angle created between individual fibrils and the bulk, while the local angular deviation of individual fibrils relative to the bulk was calculated as the average deviation angle (degree of off-axis twist).

RESULTS & DISCUSSION: Three-dimensional fibril structure varied by tendon type and health (Fig 2). Rat tail fibrils were relatively straight—as seen by a tortuosity values close to 1—and well-aligned: with small average deviation and relative chord angles. Compared to the rat tail tendon, the plantaris tendon had more fibrils with shorter relative lengths and had less aligned fibrils. Tortuosity, deviation angle and relative chord angle were all greater with lower peak frequencies and larger spread of values. This indicates a less uniform structure potentially due to reported differences between the fiber structure of these two tendons [6]. Overloaded plantaris fibrils were less organized than their healthy counterpart. Fibrils were shorter—less full-length fibrils and more short fibrils—and while tortuosity was similar to the healthy plantaris. Overloaded fibrils had larger and more varied average deviation and relative chord angles, indicative of disorganization which has been reported with similar animal models [3] and human tendinopathy [4]. Our methodology allows for the measurement of structural features that support and better characterize fibrils compared to 2D analysis. Comprehensive characterization of geometry and organization is necessary to infer mechanical function in healthy, adapted, or degenerated tissue. By utilizing machine learning to segment and reconstruct collagen fibrils from SDF-SEM images, we were able to trace 90% of fibrils in the stack with greatly increased throughput compared to manual methods (~1800 vs. 42 for rat tail fibrils, respectively). Further development of this tool could allow for investigation of different tendon regions, aging, other connective tissues, and the shape and influence of cells.

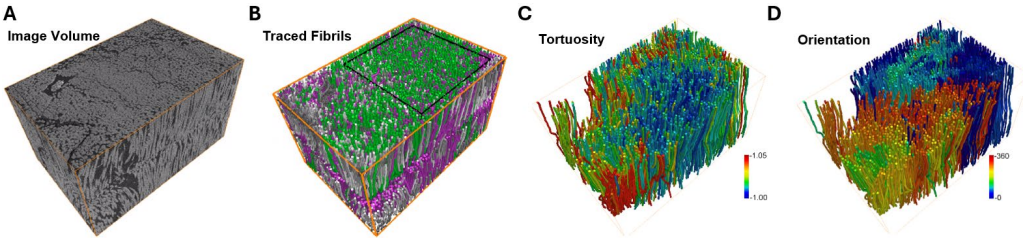

Fig 1: A) 3D SBF-SEM volume of plantaris tendon. **B)** Fibrils reconstructed in Amira with color representing % of sample spanned (gray<50%, purple>50% but less than full-length, green=full-length), **C)** tortuosity (red indicates higher tortuosity), and **D)** orientation (color shows the direction each fibril points in the imaging plane) for full-length fibrils.

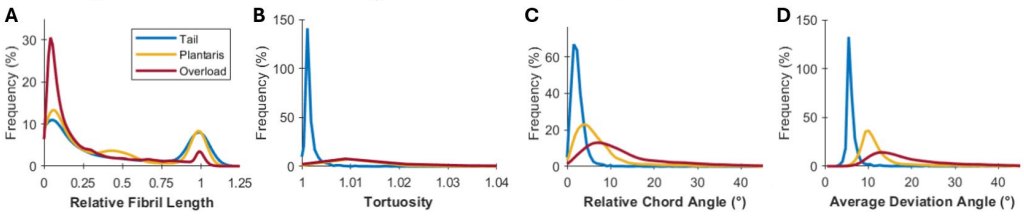

Fig 2: Frequency distributions for 3D structural fibril measures in 3 rat tendons: tail, healthy plantaris, and overloaded plantaris. **A)** Relative fibril length, B) tortuosity, **C)** relative chord angle, and **D)** average deviation angle.

REFERENCES:
[1] Provenzano & Vanderby, 2006, *Matrix Biol*, 25(2):71-84; [2] Hefferan et al., 2025, *J Orthop Res*, 43(5):994-1011; [3] Pingel et al., 2014, *J Anat*, 224(5):548-555; [4] Shepherd & Screen, 2013, *Int J Exp Pathol*, 94(4):260-270; [5] Bloom et al., 2025, *J Orthop Res*, 43(1):5-13; [6] Lee & Elliott, 2019, *J Anat*, 234:252-262